The characterization and application of plasma-based photonic crystals for high power terahertz devices

Whitney R. Thomas

A dissertation
submitted in partial fulfillment of the
requirements for the degree of

Doctor of Philosophy

University of Washington

2023

Reading Committee:

Uri Shumlak, Chair

Justin Little

Eric Meier

Program Authorized to Offer Degree:
Aeronautics & Astronautics

University of Washington

Abstract

The characterization and application of plasma-based
photonic crystals for high power terahertz devices

Whitney R. Thomas

Chair of the Supervisory Committee:
Professor Uri Shumlak
Aeronautics & Astronautics

Plasma photonic crystals (PPCs) have the potential to significantly expand the capabilities of current submillimeter wave technologies by providing high speed (microsecond time scale) control of energy transmission characteristics in the GHz through low THz range. Furthermore, plasma-based devices can be used in higher power applications than their solid-state counterparts without experiencing significant changes in function or incurring damage. PPC studies on the unique conditions present in high power applications are few. Furthermore, the construction of THz PPC experimental devices requires lattice sizes on the order of microns, plasma densities exceeding 10^{22} m^{-3}, and high power THz sources, all of which sit at the limit (or outside) of the capabilities of current technology. Analytical and numerical exploration of THz PPCs is therefore strongly motivated, allowing for advancements in understanding as hardware capabilities grow.

In support of the use of plasma-based photonic crystals for high power THz wave applications, three complementary lines of research amenable to theoretical or numerical treatment are developed that account for plasma's unique properties. Plasmas do not have discontinuous density profiles; therefore, assumptions used for dielectric PCs are not valid and a new analysis is necessary. In the first line of investigation the effect of smooth versus discon-

tinuous density profiles in PPCs on transmission characteristics is explored using a linear analytical model and group velocity band gap maps. Plasmas can deform in response to large electromagnetic fields. In the second line of investigation a two-dimensional plasma-vacuum photonic crystal is simulated using a high-fidelity plasma model, implemented in the discontinuous Galerkin finite element code WARPXM, and the plasma's response to high amplitude fields is observed. When the plasma in the PPC used for high power applications is partially ionized, changes in plasma density can occur due to energy absorption and ionization. In the final line of investigation, a reacting 5-moment multi-fluid model is implemented and applied to capture collisions and reactions for partially ionized THz plasmas.

TABLE OF CONTENTS

LIST OF FIGURES

LIST OF TABLES

ACKNOWLEDGMENTS

The information, data, or work presented herein was funded in part by the Air Force Office of Scientific Research under Award Nos. FA9550-14-1-0317 and FA9550-15-1-0271. This material is also based upon work supported by the National Science Foundation under Grant No. PHY-2108419. This work was facilitated through the use of advanced computational, storage, and networking infrastructure provided by the Hyak supercomputer system at the University of Washington.

DEDICATION

To my family and friends who have tolerated my general absence, and not infrequent freak-outs, over the duration of this degree.

Chapter 1

INTRODUCTION

High power communications and radar equipment have long been plagued by atmospheric breakdown. In fact, breakdown mitigation in high altitude aircraft was a major driver of the incipient fields of electrical discharges and low temperature plasmas[1, 2]. It was quickly recognized that the strong coupling of atmospheric plasmas to micro- and millimeter waves could be used intentionally. Plasma based power limiters were developed as early as the 1930s[3] and continue to be an active area of research[4, 5, 6, 7].

Recently, as communication bandwidths have become crowded and requirements for wireless data transfer speeds are pushing into the gigabits per second, terahertz (THz) radiation has gained attention[8, 9]. As a traditionally underutilized area of the spectrum, few devices exist for the creation, detection, or manipulation of sub-millimeter waves. Plasmas have a natural electrostatic oscillation frequency (or plasma frequency) from the MHz to high THz, depending on density, making them an attractive material for THz devices[10, 11].

Photonic crystals (PCs) are manufactured periodic structures of dielectric or conducting materials where the spacing and crystalline structure determine the frequency and direction that light can propagate (or not propagate). **Plasma photonic crystals** (PPCs) combine the designer dispersion characteristics of photonic crystals with the tunability and resistance to high power electromagnetic radiation of plasmas.

PPCs have four main characteristics that make them especially attractive in high power THz applications:

- *Strong tendency to self organize.* Collective response is a key property of plasma.

- *Resilience to high powers and temperatures.* Once ionized, gas properties do not change abruptly with additional heating (no phase change).

- *Fast (μs) control.* Plasmas can be ignited, extinguished, and modified on the time scales needed for data transmission up to THz frequencies.

- *Passive amplitude response.* Devices can be designed to have predictable amplitude dependent changes in transmission characteristics, in addition to frequency.

As the larger field of photonic crystals is relatively new, the study of PPCs is still in its infancy. Plasma photonic crystals and metamaterials were added only in 2017 to the Institute of Physics (IOP) *Plasma Roadmap: Low temperature plasmas science and technology*[12] and no articles appear with the term "plasma photonic crystal" in the title before the seminal paper by Hojo and Mase in 2004[13]. PPC studies on the unique conditions present in high power applications are few. Furthermore, the construction of THz PPC experimental devices requires lattice sizes on the order of microns, plasma densities exceeding 10^{22} m^{-3}, and high power THz sources, all of which sit at the limit of, or outside, the capabilities of current technology. Analytical and numerical exploration of the THz PPCs is therefore strongly motivated, allowing for advancements in understanding as hardware capabilities grow.

In order to better understand how the attributes particular to theoretical PPCs in high power THz applications impact transmission characteristics, three complementary lines of research are identified that both account for plasma's unique properties, and are amenable to theoretical and computational treatment. Specifically, this work addresses the presence

of density gradients in PPCs, non-ideal and nonlinear effects due to finite photonic crystal size and the presence of strong fields, and plasma formation due to high power THz waves.

1.1 Parametric study of PPCs with smooth and discontinuous density profiles

Due to plasma's diffuse nature, PPCs cannot support steep gradients in density. Despite this fact most theoretical work in PPCs is based on solid state photonic crystal methods, and assumes constant material properties with abrupt changes at material interfaces. In Chapters 3 and 4 a linear model is derived for one- and two-dimensional cold-plasma photonic crystal with an arbitrary density profile. The model is validated against a discontinuous Galerkin (DG) method numerical solution of the same device configuration. Band gap maps are then created from derived group velocity data to elucidate the operating regime of a theoretical PPC device. The band gap maps are compared for PPCs with both smooth and discontinuous density profiles. This study finds that band gap behavior is strongly correlated with density profile Fourier content, and that density profile shapes can be engineered to produce specific transmission characteristics.

1.2 Response of fully ionized plasma-vacuum photonic crystal to high power microwaves

To be useful in high power applications, plasma photonic crystals must respond predictably to EM waves of given frequency, polarization, and amplitude. Frequency and orientation dependent responses can be well characterized by traditional linear methods of dispersion relation calculation. Amplitude dependent responses generally require techniques that evolve material properties self-consistently with the electromagnetic fields.

In Chapter 5, a high fidelity two fluid (electron-ion) 5-moment plasma model[14] is solved with the discontinuous Galerkin (DG) finite element method on unstructured grids to analyze the response of a fully ionized two-dimensional plasma-vacuum photonic crystal to non-ideal and non-linear effects including: finite PPC size, finite temperature, density gradients, and

the presence of strong electric fields. Results are then compared to those of other software (ANSYS HFSS) and experiment.

1.3 Modeling plasma formation in a THz plasma photonic crystal passive power modulation device

While the preceding investigations in this thesis deal exclusively with fully ionized PPC, many of the proposed PPC devices involve partially ionized plasmas. At sufficiently high power, ionization of the surrounding gas is inevitable, leading to changes in absorption, refraction, and reflection of the THz waves. Furthermore, solid state photonic crystals can be functionalized with self-initiated plasmas in resonant defects to provide passive power modulation. Understanding the plasma's formation, as well its interaction with the EM fields, is necessary to the design of high power THz devices.

Self-consistent modeling of THz breakdown is challenging as it covers many orders of magnitude in speed (light speed to the neutral thermal speed) and ionization fraction (neutral gas to near full ionization). Models typically used in low temperature and process plasma simulations rely on reaction rate and transport coefficients calculated by third-party Boltzmann solvers. Self-consistent solution of the Boltzmann equation is often necessary in low temperature plasmas as the electron velocity distribution function (EVDF) departs from a Maxwellian, with significant impact on reactions and transport. The EVDF is a function of interaction cross sections, electric field strength, electric field oscillation frequency, gas temperature, ionization fraction, and temporal and spatial gradients. In order to simplify calculations, all but one variable is held constant, in both time and space. In contrast, in fully ionized plasmas at atmospheric densities and low temperatures, the Coulomb collision frequency becomes dominant, driving the EVDF towards a Maxwellian. The plasma can then be reliably modeled by fluid moment models with well established closures (isotropic pressure or Braginskii). Maxwellian EVDFs also allow for reaction rates to become functions of only electron temperature and relative velocity.

THz plasmas fall in a transitional regime between local thermal equilibrium (LTE) where Maxwellian electron distribution can be assumed, and non-LTE where reaction and transport rates must be calculated through self-consistent solution of the Boltzmann equation. Chapter 6 extends a reacting three-species (electron-ion-neutral atom) 5-moment model developed by Meier and Shumlak[15] for modeling THz plasma formation in the transitional LTE regime. A PPC passive power modulation device[16] is used as a benchmark, as it has been well explored experimentally and theoretically for the low- to mid-GHz range. The model is then validated against the electron Boltzmann equation solver Bolsig+[17].

Chapter 2

CONTEXT AND BACKGROUND

Plasma photonic crystals combine the designer dispersion characteristics of photonic crystals with the tunability and resistance to high power electromagnetic radiation of plasmas. Their study benefits from the techniques and concepts used in both fields. In this chapter the major ideas in photonic crystals, metamaterials, plasmonic photonic crystals are summarized (Sec. 2.1), and brief overview is given of the small subfield of plasma photonic crystals (Sec. 2.2). Finally, the analytical and numerical methods used to study the dispersion and transmission characteristics of EM waves in periodic media is introduced and their application to photonic crystals is discussed (Sec. 2.3).

2.1 Photonic crystals, metamaterials & plasmonic photonic crystals

For centuries the field of optics was dominated by geometry. The shape of a lens or mirror was the only controllable variable: dispersion was determined by nature.

With the discovery of semiconductors, and the ability to control electron dispersion within a doped crystal lattice, the electromagnetic analog was apparent to many[18, 19]. With the maturation of micro-manufacturing and materials science, designer optical dispersion became a reality. The fields of photonic crystals and optical metamaterials are the result.

2.1.1 Photonic crystals

> "A photonic crystal is the optical analogy to a crystal lattice, where atoms or molecules are periodically arranged and the periodic potential introduces gaps into the energy band structure of the crystal."
>
> *-V. Schmidt, Laser-based micro- and nano-fabrication of photonic structures, 2012*

Photonic crystals are manufactured periodic structures of dielectric materials where the spacing and crystalline structure determine the frequency and direction that light can propagate (or not propagate). One-, two-, and three- dimensional structures can exhibit the characteristics of a photonic crystal (see Fig. 2.1), with each new dimension adding possibility of new symmetries and propagation modes.

From a geometric perspective, photonic crystals work by action of constructive and destructive interference of successive reflections off changes in the index of refraction.

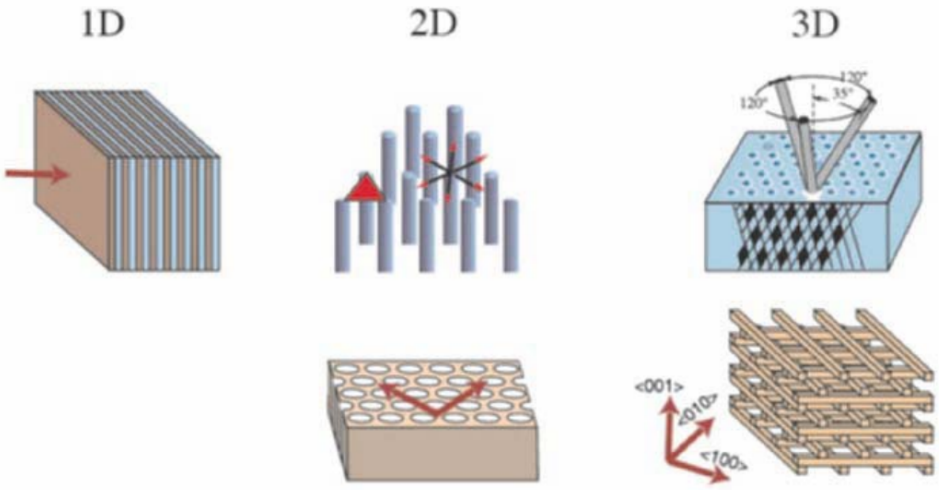

Figure 2.1: Examples of one-, two-, and three-dimensional photonic crystals[20].

The simplest case of a photonic crystal is the Bragg reflector. Forbidden frequencies, or **bandgaps**, are determined by layer thickness and contrast of the index of refraction between layers. For example, the mid-gap frequency ω_m and gap width $\Delta\omega$ for a quarter-wave stack is

$$\omega_m = \frac{n_1 + n_2}{4n_1n_2} \cdot \frac{2\pi c}{a}, \quad \text{and} \quad \frac{\Delta\omega}{\omega_m} \approx \frac{4}{\pi} \sin^{-1}\left(\frac{|n_1 - n_2|}{n_1 + n_2}\right), \tag{2.1}$$

where a is the periodicity, n_1 and n_2 are the refractive indices of each layer, and c is the speed of light. (Note: for a quarter-wave stack each layer thickness is exactly a quarter wave at the mid gap frequency, $4d_1 = 2\pi c/n_1\omega_m$, and $4d_2 = 2\pi c/n_2\omega_m$).

Symmetry, the reciprocal lattice, and Brillouin zones

Crystals are characterized by their symmetry. In the case of atomic lattices, primary definitions of symmetry are translational, and are described by **lattice vectors** $\boldsymbol{a}_i$ (see Fig. 2.3). One-dimensional crystals will have at least one lattice vector, two-dimensions will have at least two $\boldsymbol{a}_1$ and $\boldsymbol{a}_2$, etc. The **unit cell** in physical space can be infinitely repeated by any integer combination of the lattice vectors and remain the same

$$\boldsymbol{F}(\boldsymbol{r}) = \boldsymbol{F}\left(\boldsymbol{r} + \sum_{i=1,N} n_i \boldsymbol{a}_i\right), \tag{2.2}$$

where n_i are relative integers. As calculations are done in frequency space (both temporal ω and spatial k), it is more useful to define the lattice in its reciprocal space as well. The **reciprocal lattice vectors** $\boldsymbol{G}_i$ are defined such that

$$\boldsymbol{a}_i \cdot \boldsymbol{G}_j = 2\pi\delta_{ij}, \tag{2.3}$$

where δ_{ij} is the Kronecker delta symbol. For example, in a 1D lattice $\boldsymbol{G} = 2\pi/a\hat{z}$.

The unit cell in reciprocal space is the **Brillouin zone**, and constitutes the smallest unit of translational symmetry. The corresponding Brillouin zones for common physical lattices are shown in Fig. 2.3 in yellow.

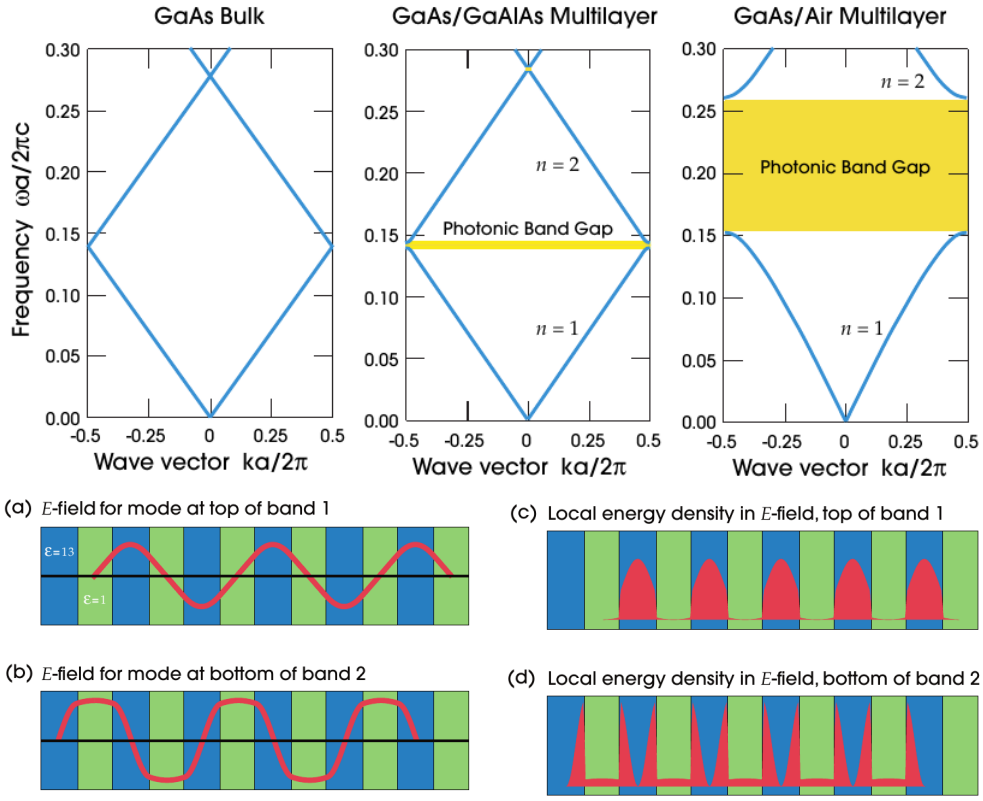

Figure 2.2: (Top) Photonic band structures of three Bragg reflectors, or 1D photonic crystals, for a bulk material (left), permittivity ratio of $\varepsilon_1/\varepsilon_2 = 12/13$ (center), and a 1/13 (right) respectively. (Bottom) Electric field amplitude and energy density for bands n =1 and 2 for the large contrast case[21].

Translational symmetry is not the only form of symmetry a lattice may have. As wave propagation properties will share their symmetry with the lattice (translational, rotational, or reflected), redundancy can be eliminated by identifying the **irreducible Brillouin zone**, outlined in red in Fig. 2.3. In the next section the irreducible Brillouin zone will be key in identifying where to sample k space in constructing a band diagram.

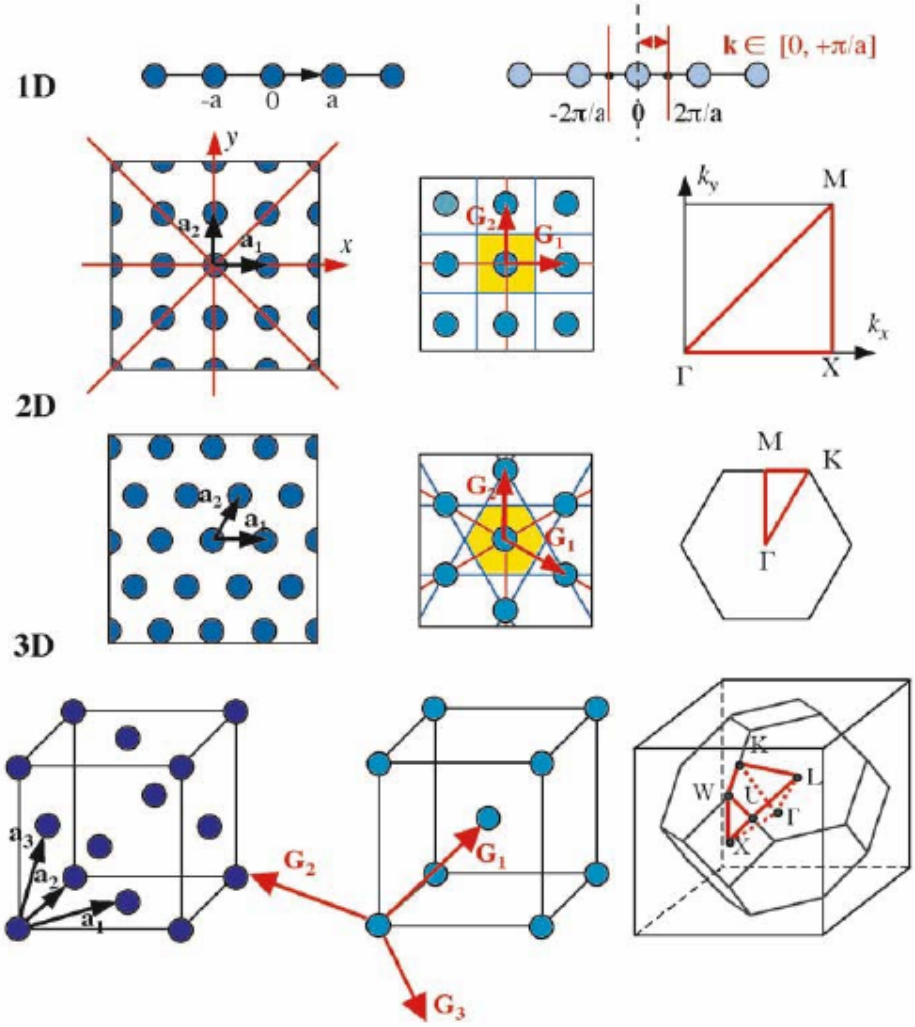

Figure 2.3: One-, two-, and three-dimensional crystals (left) with their corresponding reciprocal lattices (center) and irreducible Brillouin zones (right)[20].

Dispersion in photonic crystals: bands, bandgaps, and the band diagram

Photonic bands, like conduction and valence bands for electrons in a semiconductor, define the allowable modes. When plotted in $\omega - k$ space, important dispersion features like **phase**

velocity $v_p = \omega/k$, **group velocity** $v_g = d\omega/dk$, and bandgaps become readily apparent.

Band gaps are discontinuities in the photonic band structure, constituting a frequency range in a certain direction where propagation is not possible, and are a key feature of wave propagation in periodic structures. **Complete band gaps** occur when propagation is not possible at a range of frequencies in *any* direction, and only occur in certain types of three-dimensional lattice structures.

The dispersion of any wave (electron, photon, phonon, etc.) in a periodic structure will share symmetries with that structure. In the case of a one-dimensional crystal, like that derived for a layered plasma-dielectric by Hojo and Mase[13] shown at the right in Fig. 2.12, bandgaps form at k values that are integer multiples of the reciprocal lattice vector. In **band diagrams** k space is folded back on to itself at symmetry points so that all the bands are stacked.

In a two- or three- dimensional crystals, the bands become surfaces and volumes, respectively. Representing these higher dimensional surfaces is challenging. Three-demensional surface plots, and two-dimensional contour plot projections are options (see Fig. 2.4), but can only effectively show one or two bands at a time and gradients are hard to discern.

The least and greatest dispersion gradients, as well as band intersections and gaps, all occur along planes of symmetry that correspond to the reciprocal lattice vectors. Not coincidentally, these are the same surfaces that define the irreducible Brillouin zone. Therefore the standard format for band diagrams in two or three dimensions is to plot slices through k space at the boundaries of the irreducible Brillouin zone, the vertices of which have developed standard naming conventions (see Fig. 2.5).

2.1.2 Electromagnetic metamaterials

Metamaterials are any material with engineered properties that cannot by found in nature. **Electromagnetic metamaterials** generally refer to ordered arrays of electromagnetic os-

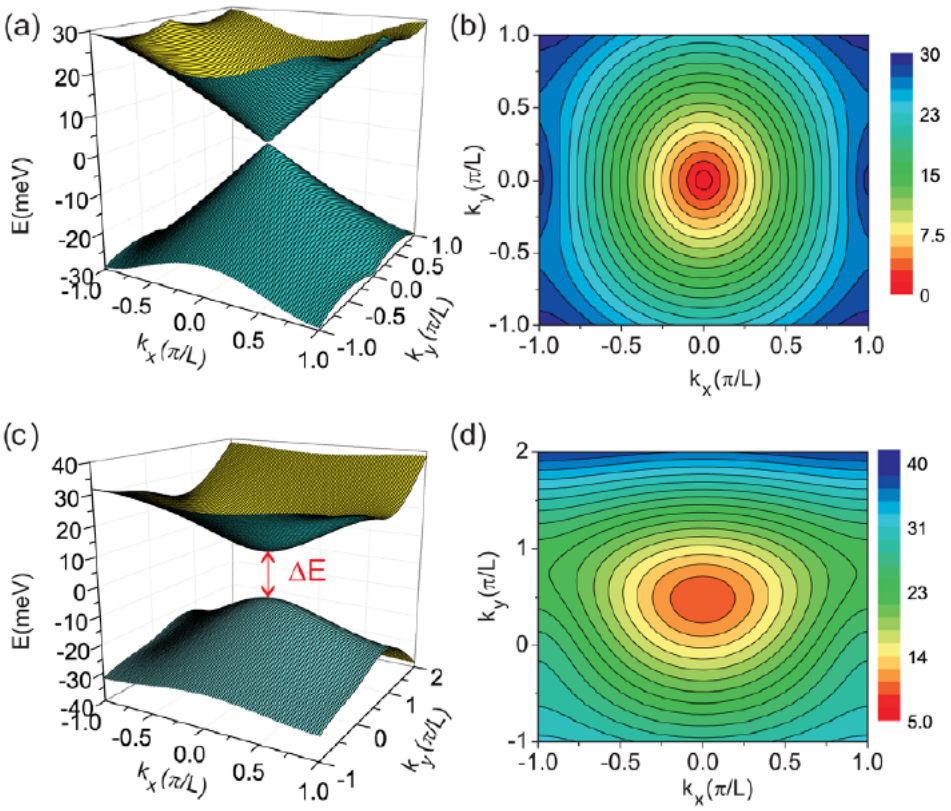

Figure 2.4: (a) and (c) are 3D plots of first conduction band and valence band of a graphene super lattice. (b) and (d) show the corresponding contour plots of the conduction band[22].

cillators arranged on a *sub-wavelength scale*. Both permittivity and permeability can be controlled, occasionally independently, and can lead to exotic effects like a negative refractive index (phase velocity opposite to Poynting flux). These "Left-handed materials" have been used to improve performance of antennas[23], create superlenses with focal lengths beyond the diffraction limit[24, 25], and achieve object cloaking[26] (see Fig. 2.6).

Plasmonic metamaterials take advantage of natural surface plasmon resonances on conductor-dielectric interfaces as the resonant component. They have proposed uses in cancer

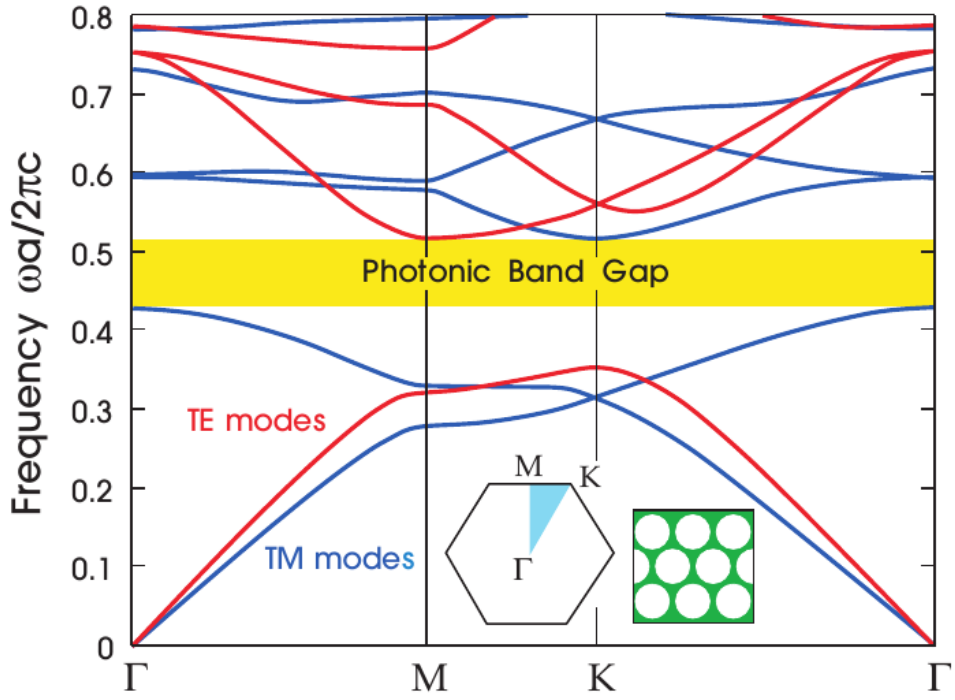

Figure 2.5: A band diagram for a 2D triangular lattice of air columns. The Brillouin zone is shown outlined in black, with the irreducible Brillouin zone shaded in blue, along with conventional labeling of vertices Γ, M and K. A complete photonic band gap is shown in yellow[21].

treatment[29], signal amplification[30], spectroscopy, and high efficiency photovoltaics[31]. Field energy is absorbed into localized plasma oscillations that form at the surface of the metal/dielectric interface. On closed surfaces (cylinder in 2D, sphere in 3D) surface plasmons are stationary, and accumulate energy, producing fields many times larger than the driving wave.

For cylindrical rods the surface plasmon resonant frequency falls between $\omega_{pe}/\sqrt{3}$ and $\omega_{pe}/\sqrt{2}$, and is a function of fill fraction and mode number (see Fig. 2.8). Each mode has a

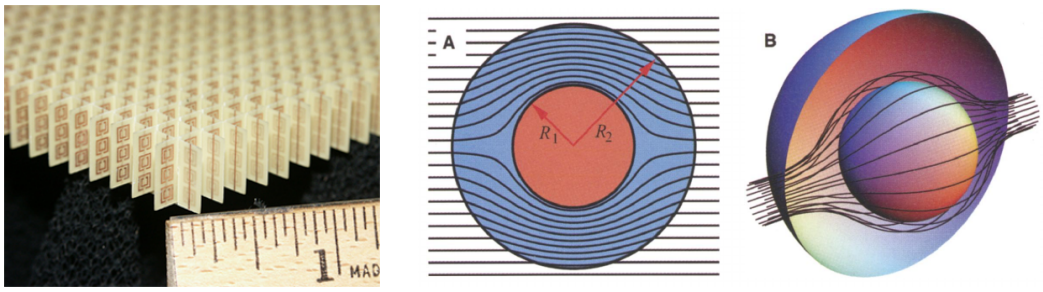

Figure 2.6: (Left) Split ring resonator array metamaterial[27]. (Right) Ray tracing of a 2D and 3D negative index cloaking material[28]

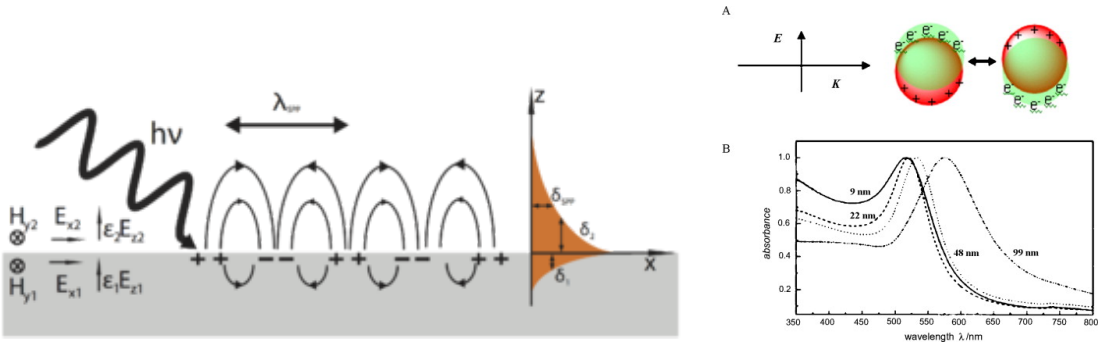

Figure 2.7: (Left) sketch of a surface plasmon, Wikipedia. (Right) surface plasmons on gold nanoparticles.[29]

magnetic field arrangement as shown at the right.

2.1.3 Plasmonic photonic crystals

Plasmonic photonic crystals combine the properties of photonic crystals and plasmonic metamaterials. Plasmon resonant frequency and oscillator spacing are chosen to coincide, creating anomalous dispersion characteristics.

In plasmonic photonic crystals, the frequency dependency of the permittivity becomes

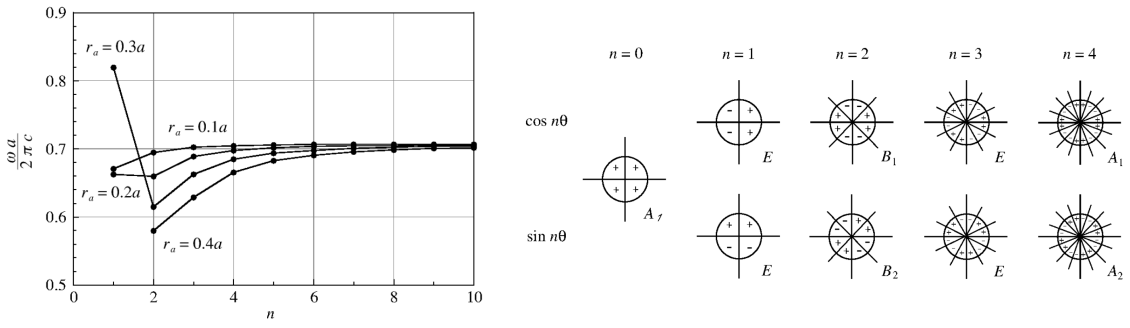

Figure 2.8: Mode frequencies and spacial configuration of modes for surface plasmon polaritons on a conducting rod[32].

important

$$\varepsilon_p(\mathbf{r},\omega) = 1 - \left(\frac{\omega_{pe}(\mathbf{r})}{\omega}\right)\frac{1}{1 - j(\nu_m/\omega)}, \tag{2.4}$$

where ω_{pe} is the electron plasma frequency, and ν_m is the collision frequency.

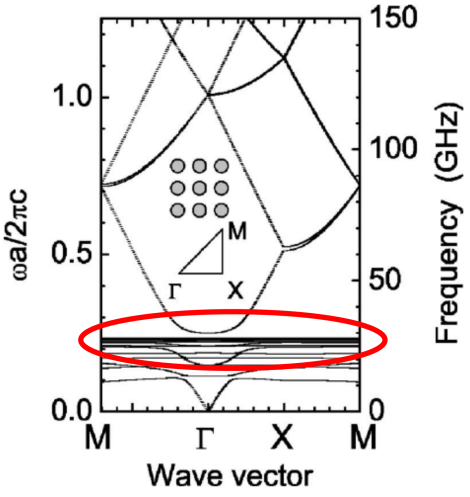

Figure 2.9: Band diagram for PC with $a = 2.5$ mm, $r = 0.5$ mm, and $n_e = 10^{13}\text{cm}^{-3}$. Flat-bands due to surface plasmons are circled in red[33].

When $\omega < \omega_{pe}$, ε_p becomes negative, surface plasmons can form and the crystal enters a plasmonic regime[32]. When confined to a closed surface (cylindrical in 2D and spherical in 3D) these plasmons are non-propagating, and present as "flat bands" in the band diagram (see Fig. 2.9), and result in regions of decreased transmission.

When the frequency of the surface plasmon falls within a bandgap, anomalous transmission can occur, as was seen in a 2D plasma photonic crystal by Righetti et al.[34]. Resonant coupling between adjacent plasma filled columns acted as a transmission line in a region that propagation should not normally occur.

2.2 Plasma photonic crystals

In their simplest form, plasma photonic crystals, or PPCs, are theoretically identical to metallic plasmonic photonic crystals, already a rich field with many potential applications. Additionally, plasmas have many advantages over their solid state counterparts:

- **Plasmas can access the high GHz and THZ frequency band**. Plasmon resonances can occur in the **THz range**, an underutilized portion of the electromagnetic spectrum.

- **Fast control of photonic crystal properties.** Plasmas are created when needed, with lifetimes in the μs, for fast reconfiguration of lattice characteristics.

- **Fast control of plasmonic properties**. Plasma resonant frequencies can be controlled through application of external EM fields.

- **High energy applications**. Absorption can be controlled through collisionality. Plasmas are not subject to phase-change at high temperatures.

- **Self organization**. Plasmas can produce stable (in the time scales of interest) periodic

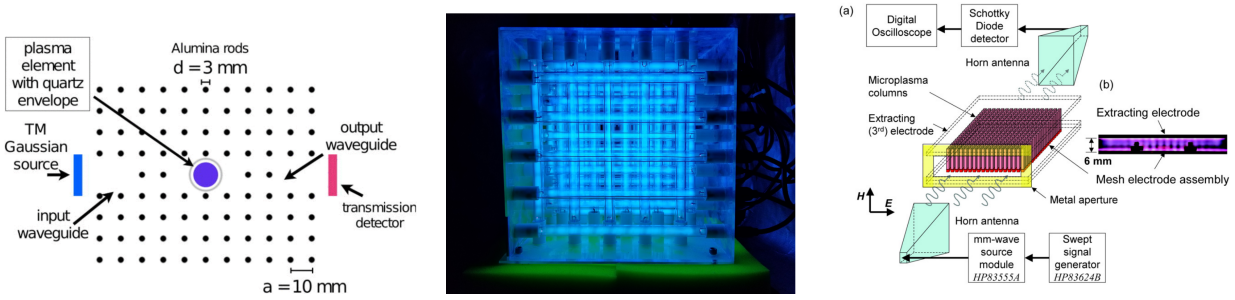

Figure 2.10: (Left) Plasma photonic crystal created by augmenting a traditional photonic crystals[35]. (Center) A microplasma discharge array[36]. (Right) Plasma photonic crystals where plasma forms the principal material[37].

structures. Potential devices could take advantage of naturally occurring periodicity from plasma instabilities.

They can be formed either by augmenting traditional photonic crystals made of dialectics or metals, or as one of the primary materials (see Fig. 2.10). Plasmas with regular periodic density perturbations can also occur naturally as a result of plasma instabilities and self organization (see Fig. 2.11).

As the larger field of photonic crystals is a relatively new field, the study of PPCs is still in its infancy. Plasma photonic crystals and metamaterials were added only in 2017 to the IOP *Plasma Roadmap: Low temperature plasmas science and technology*[12]. No articles appear with the term "plasma photonic crystal" in the title before the seminal paper by Hojo and Mase in 2004[13], and current literature is dominated by a handful of authors. The only review paper to date was done by Sakai et al. in 2012[40]. Plenty of work remains for plasma photonic crystals to become a mature field that produces useful applications.

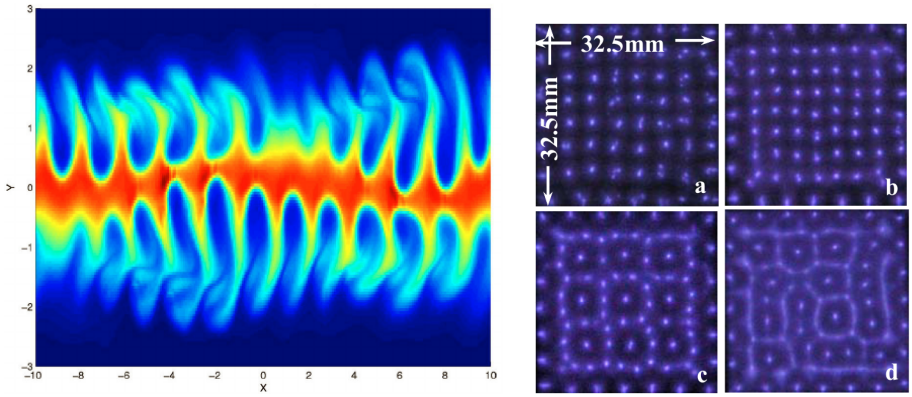

Figure 2.11: (Left) Simulation of the lower hybrid drift instability in a plasma forming a planar current sheet[38]. (Right) Dielectric barrier discharge 2D PPC[39]

2.3 Analytical and numerical methods for EM waves in periodic media

In this section, various analytical and numerical techniques used in understanding EM wave propagation through periodic media are described. They lay the groundwork for the theoretical and computational tools developed in later chapters.

The methods have been sub-classified into two major categories by the properties they aim to describe:

1. **Dispersion.** Methods that result in a dispersion function that establishes the relationship between frequency and wavenumber

$$\mathbb{D}(\omega, k) = 0. \tag{2.5}$$

   Dispersion functions describe what is happening *within* the material: allowable modes, propagation direction, phase velocity and energy flux.

2. **Transmission.** Transmission or scattering methods use a black box approach. Given an electromagnetic wave at a certain frequency, how much is transmitted through, and

how much is reflected back out?

2.3.1 Dispersion properties of infinite crystals

Infinite crystals do not exist in nature, but as in many other problems, studying the ideal case can lead to valuable insights about the important underlying physics. In the study of photonic crystals, copious amounts of inherent symmetry can be harnessed to create tractable problems.

In the following methods, all begin with Maxwell's equations with a spatially varying permittivity (and occasionally permeability)

$$\nabla \times \boldsymbol{E} = -\frac{\partial \boldsymbol{B}}{\partial t}, \tag{2.6}$$

$$\nabla \times \boldsymbol{B} = \mu(\boldsymbol{r})\varepsilon(\boldsymbol{r})\frac{\partial \boldsymbol{E}}{\partial t} + \mu(\boldsymbol{r})\boldsymbol{J}, \tag{2.7}$$

$$\nabla \cdot \boldsymbol{E} = \frac{\rho_c}{\varepsilon(\boldsymbol{r})}, \tag{2.8}$$

$$\nabla \cdot \boldsymbol{B} = 0, \tag{2.9}$$

and some variation on Bloch (or Floquet) theorem, which states that if a wave is moving through a periodic medium, it has the form

$$F(\boldsymbol{r}) = e^{i\boldsymbol{k}\cdot\boldsymbol{r}} u_{\boldsymbol{k}}(\boldsymbol{r}), \tag{2.10}$$

where $u_{\boldsymbol{k}}$ has the same periodicity as the crystal such that

$$u_{\boldsymbol{k}}(\boldsymbol{r}) = u(\boldsymbol{r} + \boldsymbol{n}\cdot\boldsymbol{a}), \tag{2.11}$$

where $\boldsymbol{n}$ is an array of integers, and $\boldsymbol{a}$ is a lattice vector of the crystal.

The analytical dispersion relation

Exact solutions for dispersion relations of Bragg gratings and photonic crystals are few. From the point of view of engineering optical devices finite crystals are by far more prevalent,

and reflectance and transmittance far more useful[20]. Furthermore, sudden changes in the permittivity require a large number of terms and can prove intractable. Therefore, numerical methods dominate in both the calculation of band diagrams for infinite photonic crystals as well as the transmission/reflection characteristics of finite crystals.

That being said, the further a solution can be taken analytically, the more that can be understood about the physical characteristics important to the problem. A valuable outcome of existing analytical solutions are exact expressions for top and bottom frequencies of band gaps.

Yariv and Yeh[18] first derive a dispersion relation for electromagnetic waves in a general periodic dielectric medium. The function takes the form of an infinite set of coupled equations that must be solved for each wave vector $\mathbf{k}$. For a one-dimensional perturbation

$$k^2 A(k) - \omega^2 \mu \sum_l \varepsilon_l A(k - lg) = 0, \tag{2.12}$$

where $A(k)$ are the Fourier components of the electric field $E = \int A(k) e^{-i\boldsymbol{k}\cdot\boldsymbol{x}} d^3k$, ε_l for the dielectric tensor $\varepsilon(x) = \sum_l \varepsilon_l e^{-ilgx}$, a is the perturbation period, and $g = 2\pi/a$ is the reciprocal lattice vector. A direct solution of the first two coupled equations for $k = \frac{1}{2}G$ gives the frequencies of the first band gap edges

$$\omega_\pm^2 = \frac{\pi^2/a^2}{\mu(\varepsilon_0 \pm |\varepsilon_1|)}. \tag{2.13}$$

In 2016, Lehmann et al. adapts the idea for a laser-driven plasma photonic crystal[41, 42]. Beginning with the time harmonic wave equation for the electric field, and assuming a 1D plasma density perturbation with the form

$$n_e = \sum_l \eta_l e^{-ilgx}, \quad \text{where} \quad \eta_l = \frac{1}{a}\int_0^a n_e(x) e^{ilgx} dx, \tag{2.14}$$

where $n_e(x)$ is taken from a Particle in Cell (PIC) simulation. The final dispersion relation for an incoming wave with oblique incidence to the perturbation takes the form of

$$A_l \left[-(k_x + lg)^2 - k_y^2 + \left(\frac{\omega}{c}\right)^2 \right] - \left(\frac{\omega_{pe}}{c}\right)^2 \sum_{l'} \eta_{l-l'} A_{l'} = 0. \tag{2.15}$$

Adapted Kronig-Penny model

The Kronig-Penny model in quantum mechanics is used to describe the idealized propagation of a particle in a periodic rectangular potential well. Hojo and Mase[13] adapted the model for EM waves in plasma-dielectric 1D photonic crystal. They start with a 1D stationary wave equation for the electric field

$$\left[\frac{\partial^2}{\partial z^2} + k_0\varepsilon(z)\right] E(z) = 0, \tag{2.16}$$

where $k_0 = \omega/c$ and the permittivity is defined as

$$\varepsilon(z) = \begin{cases} 1 - \left(\frac{\omega_{pe}}{\omega}\right)^2, & -Ld \leq z \leq 0 \\ \varepsilon_m, & 0 \leq z \leq L \end{cases}, \tag{2.17}$$

and

$$\varepsilon(z \pm L(1+d)) = \varepsilon[z].$$

As the permittivity is periodic, the solution for $E(z)$ must also be. This results in the following constraints on E and it's derivative E'

$$E(L) = \lambda E(-Ld),$$
$$E'(L) = \lambda E'(-Ld),$$

where

$$\lambda = \exp[ikL(1+d)].$$

Assuming a similar solution to the standard Kronig-Penny model, and solving for coefficients, they obtain the following dispersion relations for $\omega < \omega_{pe}$

$$\cos[kL(1+d)] = \frac{\kappa^2 + k_m^2}{2\kappa k_m}\sin(k_m L)\sinh(\kappa L d) + \cos(k_m L)\cosh(\kappa L d) \tag{2.18}$$

and for $\omega > \omega_{pe}$

$$\cos[kL(1+d)] = \frac{k_p^2 + k_m^2}{2k_p k_m}\sin(k_m L)\sinh(k_p L d) + \cos(k_m L)\cosh(k_p L d) \tag{2.19}$$

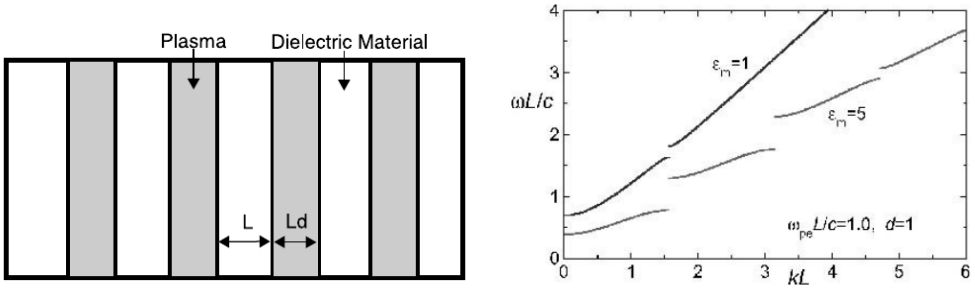

Figure 2.12: Schematic for a 1D plasma-dielectric photonic crystal (left), and its dispersion relation as calculated by Hojo and Mase using an adapted Kronig-Penny model (right).

where $k_p = k_0\sqrt{1-(\omega_{pe}/\omega)^2}$, $\kappa = k_0\sqrt{(\omega_{pe}/\omega)^2-1}$, and $k_m = k_0\sqrt{\varepsilon_m}$.

Despite the initial dissimilarity in appearance to the dispersion relations found in the previous section, when solved numerically for ω and k they take on the same familiar form (see Fig. 2.12).

Plane Wave Expansion Method

The plane wave expansion method (PWEM) takes advantaged of Bloch waves and Floquet theory and reduces the time and space harmonic Maxwell equations to an eigenvalue problem. Frequencies and spatial field distributions of allowed modes can be found by using any numerical eigenvalue solution method. Its disadvantages are the loss of physical meaning in the equation set (the analytical progression stops at the wave equation), and it is slow to converge with sharp changes in permittivity.

In dielectric photonic crystals, the permittivity is only a function of position. Well known derivations can be found in many texts[21][20] and result in the following problem

$$\frac{1}{\varepsilon_r(\boldsymbol{r})}\nabla\times[\nabla\times\boldsymbol{E}] - \frac{\omega^2}{c^2}\boldsymbol{E} = 0 \tag{2.20}$$

$$\nabla\times\left[\frac{1}{\varepsilon_r(\boldsymbol{r})}\nabla\times\boldsymbol{H}\right] - \frac{\omega^2}{c^2}\boldsymbol{H} = 0 \tag{2.21}$$

where ε_r is the relative permittivity, $c = \sqrt{\varepsilon_0 \mu_0}$ and $\frac{\omega}{c} = k_0 = \frac{2\pi}{\lambda_0}\boldsymbol{E}$, with c, k_0, and λ_0 representing the speed, wave number and wavelength of light in a vacuum. The above equations take the form of an eigenvalue problem

$$\Theta \boldsymbol{E} = \left(\frac{\omega}{c}\right)^2 \boldsymbol{E} \tag{2.22}$$

where the eigenvectors $\boldsymbol{E}$ and $\boldsymbol{H}$ from Eqs. (2.20) and (2.21) which are the spatial patterns of the harmonic modes associated with the with eigenvalues $\frac{\omega^2}{c^2}$. This is only solvable if Θ is Hermitian. In a purely dielectric material, this is not a problem.

In plasmas, and other conductors, the permittivity is not only a function of space, but also frequency. Θ then takes on a ω dependence and the natural Hermiticity of the operator is broken. Kuzmiak and Maradudin[43] find a way overcome the problem. They derive a modified the plane wave method for two-dimensions with the following Fourier expansion of the dielectric function

$$\varepsilon_r(\boldsymbol{r}) = \sum_{\boldsymbol{G}} \hat{\varepsilon}_r(\boldsymbol{G}) e^{i\boldsymbol{G}\cdot\boldsymbol{r}}), \tag{2.23}$$

with the Fourier components

$$\hat{\varepsilon}(\boldsymbol{G}_\parallel) = \begin{cases} \varepsilon_d - f\left[1 - \varepsilon_d - \frac{\omega_{pe}^2}{\omega(\omega - i\nu_m}\right], & \boldsymbol{G}_\parallel = 0 \\ f\left[1 - \varepsilon_d - \frac{\omega_{pe}^2}{\omega(\omega - i\nu_m}\right] \frac{2J_1(\boldsymbol{G}\parallel R)}{\boldsymbol{G}\parallel R)}, & \boldsymbol{G}_\parallel \neq 0 \end{cases}, \tag{2.24}$$

where $\boldsymbol{G} = 2\pi/l\boldsymbol{a}$ for $l = 0, \pm 1, \pm 2, ...$ are the reciprocal lattice vectors, a is the lattice constant, $f = \pi R^2/a^2$ is the fill fraction, J_1 is a Bessel function, and R is the radius of plasma column. Substituting this into Eq. (2.20) and Eq. (2.21) and separating terms, they get a fourth order and third order polynomial, respectively, in ω that will not be repeated here. Combining the four $N \times N$ matrices into a single $4N \times 4N$ matrix, they successfully linearize the problem.

Sakai and Sakaguchi[33] adapt the idea from Kuzmiak for plasmas. Sakai et al. find the solution of the problem to be slow and computationally expensive. They are also limited to

a single plasma density profile. Despite this they generate a variety of band diagrams for collisional and collisionless plasma columns.

For other density profiles, they develop a complex field finite difference time domain (FDTD) method (see Sec. 2.3.1).

Qi et al.[44] derive a more computationally tractable eigenvalue problem for the magnetic field $\boldsymbol{B}$ in a collisionless plasma-dielectric photonic crystal. The time harmonic wave equation is then

$$\nabla \times \nabla \times \boldsymbol{B} = \frac{\omega^2}{c^2} \varepsilon_r(\boldsymbol{r}) \boldsymbol{B} \tag{2.25}$$

which does not appear to be correct. Since ε_r is a function of space, it cannot be brought outside the curl differential operator without applying a chain rule. It should be

$$\nabla \times \frac{1}{\varepsilon_r(\boldsymbol{r})} \nabla \times \boldsymbol{B} = \frac{\omega^2}{c^2} \boldsymbol{B} \tag{2.26}$$

which has a non-trivial solution. Nonetheless, Qi et al. find a solution with the following array of rectangular dielectric columns in plasma

$$\hat{\varepsilon}(\boldsymbol{G}) = \begin{cases} \left(1 - \frac{\omega_p^2}{\omega^2}\right) + f\left(\varepsilon_d - 1 + \frac{\omega_{pe}^2}{\omega}\right), & \boldsymbol{G} = 0 \\ f\left(\varepsilon_d - 1 + \frac{\omega_{pe}^2}{\omega}\right) P(\boldsymbol{G}), & \boldsymbol{G} \neq 0 \end{cases} \tag{2.27}$$

where $P(G) = \frac{\sin G_x R/2}{G_x L/2} \frac{\sin G_y R/2}{G_y L/2}$. Much like the PWEM developed by Sakai, that of Qi et al. is limited to a single perturbation with period a. Furthermore, Qi did not derive a solution for TE polarized waves.

Numerical time-domain methods for fixed material properties

Finite Difference Time Domain solvers for band structure analysis of dielectric photonic crystals are many[45, 46, 32, 47]. To accomplish the simulation of an infinite periodic domain, while not restraining the wave modes to only those that are an integer multiple of the domain length, they rely on pseudo-periodic boundaries that apply a phase shift to EM waves propagating through boundaries.

Celuch-Marcysiak et al. were one of the first to develop a complex valued, spatially looped 3D FDTD algorithm for electromagnetic fields with frequency independent permittivity and permeability. This begins with the application of the Floquet theorem to the electric and magnetic fields such that the fields can be expressed as

$$\boldsymbol{E}(\boldsymbol{r}) = \bar{\boldsymbol{E}}(\boldsymbol{r}) \exp(-i\boldsymbol{k} \cdot \boldsymbol{r} + \phi), \tag{2.28}$$

$$\boldsymbol{H}(\boldsymbol{r}) = \bar{\boldsymbol{H}}(\boldsymbol{r}) \exp(-i\boldsymbol{k} \cdot \boldsymbol{r} + \phi) \tag{2.29}$$

, respectively, where $E(\boldsymbol{r})$ is complex, $\bar{E}(\boldsymbol{r})$ is periodic with period $\boldsymbol{a}$, and ϕ is some phase shift. The fields can then be separated into their real and complex parts

$$\begin{aligned} \boldsymbol{E}(\boldsymbol{r}) &= \bar{\boldsymbol{E}} \cos(\boldsymbol{k} \cdot \boldsymbol{r} + \phi) + i\bar{\boldsymbol{E}} \sin(\boldsymbol{k} \cdot \boldsymbol{r} + \phi) \\ \boldsymbol{H}(\boldsymbol{r}) &= \bar{\boldsymbol{H}} \cos(\boldsymbol{k} \cdot \boldsymbol{r} + \phi) + i\bar{\boldsymbol{H}} \sin(\boldsymbol{k} \cdot \boldsymbol{r} + \phi) \end{aligned} \tag{2.30}$$

and evolved separately (assuming the medium is lossless, and there is no coupling within the domain). The only coupling that does occur is at that boundaries, where a phase shift $\psi = \boldsymbol{k} \cdot \boldsymbol{a}$ is applied

$$\boldsymbol{E}^i(\boldsymbol{r}_1) = \boldsymbol{E}^r(\boldsymbol{r}_2) e^{-i\psi}, \tag{2.31}$$

$$\boldsymbol{E}^i(\boldsymbol{r}_2) = \boldsymbol{E}^r(\boldsymbol{r}_1) e^{i\psi}, \tag{2.32}$$

where superscripts i and r denote the real and imaginary parts, and subscripts 1 and 2 are the adjoining edges of periodic boundaries. Maxwell's equations are discretized in the standard way on a Yee grid[45]. A spatial distribution of $\varepsilon(r)$ and $\mu(r)$ are set, a wide bandwith pulse is initialized, and the problem evolved in time until prominent modes emerge. The frequencies of the allowed modes are found through Fourier analysis of the field amplitudes in time. A simulation is then run for each wavenumber $\boldsymbol{k}$ of interest to construct a band diagram (Fig. 2.13).

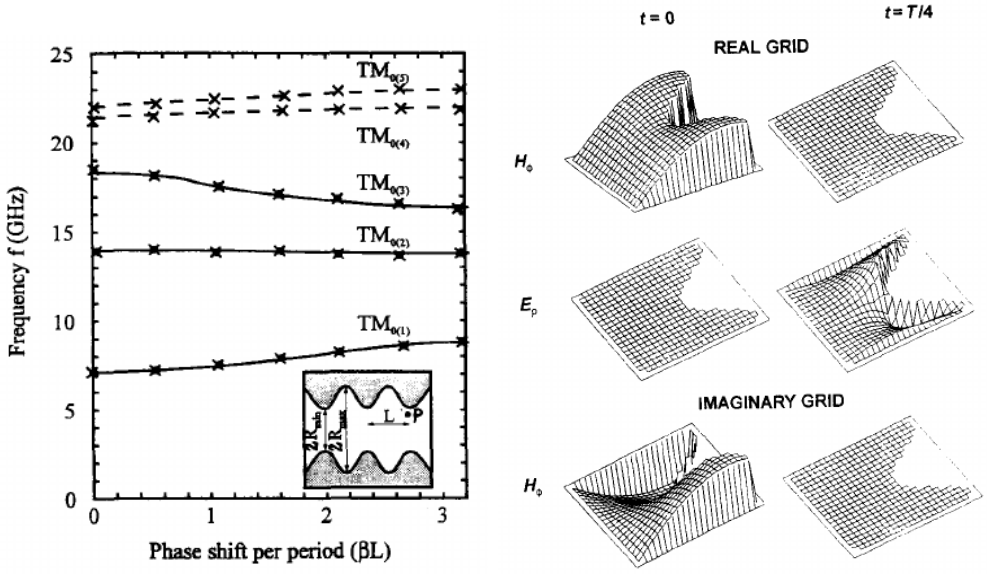

Figure 2.13: (Left) Band diagram of TM mode by complex, specially looped FDTD method per Celuch-Marcysiak et al.[46] for corrugated wave guide with period $L = 1.67$ cm. (Right) the spatial distribution of fields for the same case showing the mode corresponding to $f = 7.717$ GHz and $\beta L = \pi/3$.

Time-domain methods for approximating frequency dependent media

As in all previous methods, adding a frequency dependent permittivity imposes challenges. This is exacerbated by the fact that the calculation is performed in the time domain. Qiu et al.[48] developed a similar algorithm that discretizes Maxwell's equations with the current expressed in terms of a spatially dependent conductivity σ and the electric field (by way of Ohm's Law)

$$\frac{\partial \boldsymbol{H}}{\partial t} = -\frac{1}{\mu(\boldsymbol{r})}\nabla \times \boldsymbol{E}, \tag{2.33}$$

$$\frac{\partial \boldsymbol{E}}{\partial t} = -\frac{1}{\varepsilon(\boldsymbol{r})}\nabla \times \boldsymbol{H} - \frac{\sigma(\boldsymbol{r})}{\varepsilon(\boldsymbol{r})}\boldsymbol{E}. \tag{2.34}$$

This sidesteps the problem of frequency dependence (assuming the incoming wave fre-

quency is well below that of the plasma frequency) and uses only steady state conductivity values.

In the previous section on PWEM solvers (Sec. 2.3.1, Sakai et al.[33] compare their modified PWEM solver to a finite difference algorithm developed by the author[49]. This method discretizes the time harmonic wave equation for a complex electric field

$$\nabla \times \nabla \times \boldsymbol{E} = \frac{\omega^2}{c^2} \varepsilon_r(\boldsymbol{r}) \boldsymbol{E}, \tag{2.35}$$

where

$$\varepsilon_r(\boldsymbol{r}) = 1 - \left(\frac{\omega_{pe}(\boldsymbol{r})}{\omega} \right)^2 \frac{1}{1 - i\left(\nu_m/\omega\right)} \tag{2.36}$$

and uses the same looped boundary conditions derived from Bloch-Floquet theorem as Celuch-Marcysiak et al., expressed in 2D as

$$\boldsymbol{E}(x_0 + a) = \boldsymbol{E}(x_0) \exp(-ik_x a), \quad \boldsymbol{E}(y_0 + a) = \boldsymbol{E}(y_0) \exp(-ik_y a). \tag{2.37}$$

Similarly to the Celuch-Marcysiak approach, a separate simulation must be run for each value of k. Additionally, the permittivity is frequency dependent, meaning a separate calculation must also be run for each frequency and $\varepsilon_p(k)$. A band diagram from 0 to 150 GHz, at 1 GHz resolution, resolving 100 values of k would take 15,000 separate calculations. Finally, a particular k, ω pair is determined to be on a branch if power density at that frequency shows strong peaking in a Fourier analysis of the wave spectrum.

The calculations described by Sakai et al. were performed on a 20x20 grid for both a uniform density plasma column in vacuum and a plasma column with a J_0 Bessel function density profile (see Fig 2.14).

Other approaches, such as the Recursive-Convolution Method, use higher order relationships between the the electric and displacement field

$$D(t) = \varepsilon_0 \varepsilon_\infty \boldsymbol{E}(t) + \varepsilon_0 \int_{\tau=0}^{t} \boldsymbol{E}(t - \tau) \chi(\tau) d\tau. \tag{2.38}$$

Details can be found in Taflove and Hagness[45] but will not be covered here.

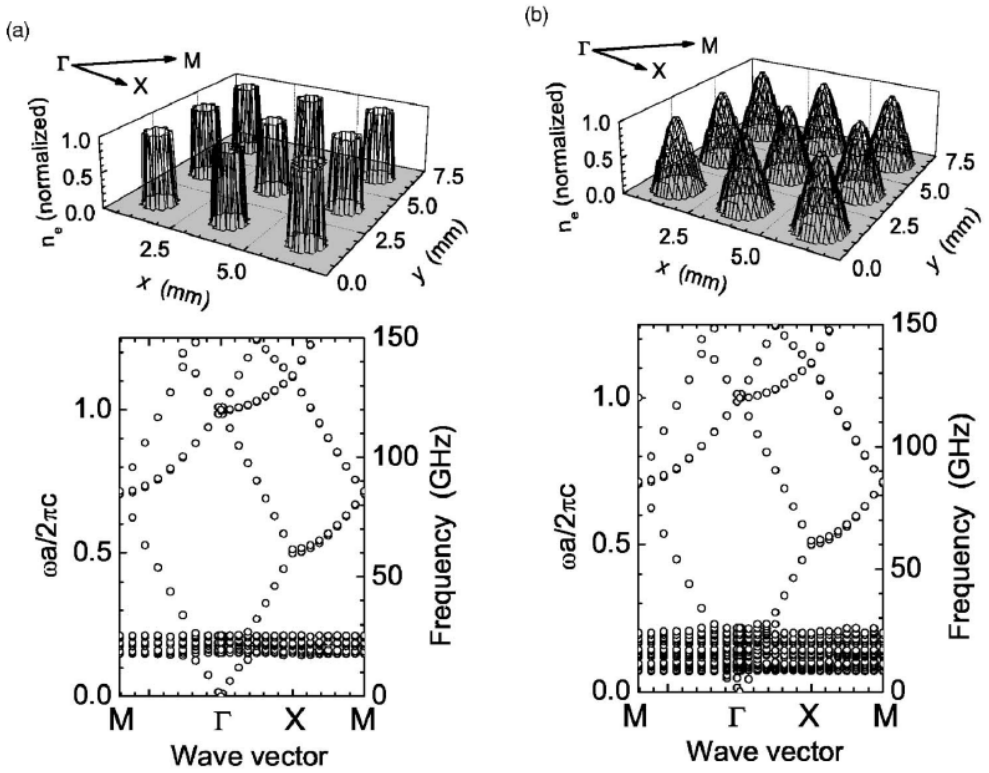

Figure 2.14: (a) Band diagram of TE mode by direct solution method developed by Sakai et al[33] for lattice constant $a = 2.5$ mm, plasma column diameter $d = 1.0$ mm, and a uniform plasma density of $n_e = 10^{19}$ m^{-3}. (b) Band diagram of TE mode for same case as (a) but for a J_0 density profile with maximum $n_e = 10^{19}$ m^{-3} and full width at half maximum of $d = 1.0$ mm.

Time-domain methods with auxiliary differential equations for material dynamics

The most straightforward (although computationally heavy) method used to circumvent the complications of a frequency dependent material response in a time-domain simulation is to evolve material properties self-consistently in time.

For conductive materials, the simplest model is the Drude, or cold plasma model, which describes the evolution of the electron velocity as a function of only the Lorentz force and collisions

$$\frac{\partial \boldsymbol{v}_e}{\partial t} = -\boldsymbol{v}_e \nu_m - \frac{e}{m_e}\left(\boldsymbol{E} - \boldsymbol{v}_e \times \boldsymbol{B}\right). \tag{2.39}$$

This is coupled into Maxwell's equations through the current $\boldsymbol{J} = -en_e v_e$, assuming ions are stationary. The Drude permittivity is obtained directly from this expression

$$\varepsilon(\omega) = \varepsilon_0 \left(1 - \frac{\omega_{pe}^2}{\omega^2}\frac{1}{1 - i\nu_m/\omega}\right) \tag{2.40}$$

therefore, all dispersion calculation methods up until this point are physically and mathematically (if not numerically) identical. In most cases, the simple Drude model is good approximation of plasma-EM wave interactions. Trieschmann et al.[50] use a Particle-in-Cell code to look at the band structure of piecewise constant 1D plasma-dielectric photonic crystal. Unlike in the Drude model, a Maxwellian distribution function is not assumed. The resulting band diagrams are compared to models assuming a cold plasma (or Drude model)[13] and found to coincide exactly (see Fig. 2.15).

While studies like this serve as validations of both simple model assumptions and complex model validity under similar conditions, the primary advantage of the simultaneous evolution of the material system is when amplitudes become large enough to change the properties of the material substantially, and as a consequence alter its dispersion characteristics.

2.3.2 Dispersion properties of infinite crystals with defects

Defects within photonic crystals create propagation of stationary modes where none would normally exist. Narrow bandpass filters with high Q, lossless waveguiding and bending, and photonic crystal fibers are some of the many applications of defected photonic crystals. Some of the common methods are summarized below:

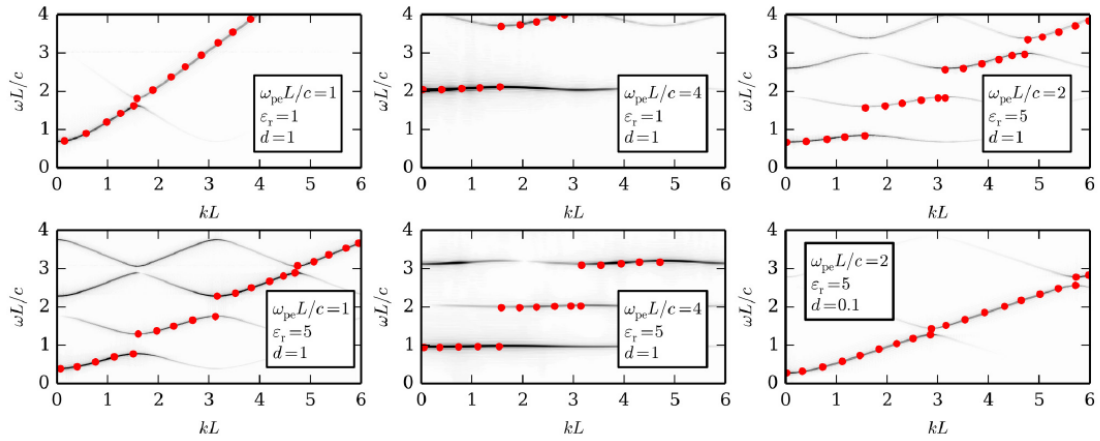

Figure 2.15: Dispersion relations calculated using PIC simulations[50] in black, and the same case using the cold plasma model[13] in red.

- In 1D photonic crystals the defect mode has a known **resonance condition**

$$\omega = \frac{n_1 cp}{L} \tag{2.41}$$

where L is the length of the cavity, $n_1 = \sqrt{\varepsilon_1}$ is the index of refraction of the dielectric layer formed by the defect, and p is an integer. Fig. 2.16 shows the defect resonances and field distributions for $p = 1$, 2, and 3.

- In 2D and 3D crystals, the effect of the defect can be approximated by way of the **Supercell Method**. Here the PWEM is used by reimposing the symmetry lost by creating the defect through the creation of a new, larger unit cell centered on the defect (see Fig. 2.16). As long as the defects in each unit cell are sufficiently separated, the results should closely approximate the true case.

- The most commonly used methods are those based on the **Tight-binding model** for calculating electronic band structures and impurity levels in solid state physics.

These methods are beyond the scope of this thesis, and the reader is referred to other reference for further details[20, 51].

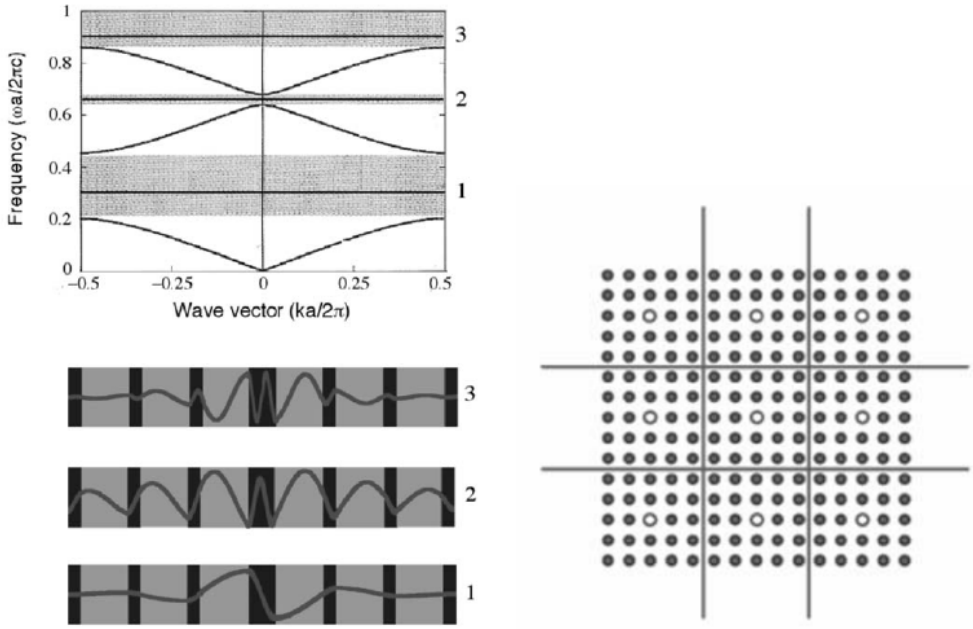

Figure 2.16: (Left) Band diagram and electric field distribution of 1D photonic crystal with defect showing stationary modes at 1, 2 and 3. (Right) Example unit cells used in the Supercell method.

2.3.3 Transmission, reflection, and absorption properties of finite crystals

An infinite crystal will have perfect reflection at frequencies that fall within the bandgap. Crystals with a finite depth will allow some fraction of the energy to be transmitted. In the engineering of photonic devices, it is not enough to know only where bandgaps are located, but also to what degree the signal will be attenuated.

A variety of methods exist for determining the transmission, reflection, and absorption of photonic crystals with finite extent. As they are not the primary focus of the research, they are listed here without further explanation: the transfer matrix methods (TMM), the Pendry method, the scattering matrix method, multi-pole method, or modal method, and the time-domain methods[45].

Chapter 3

PARAMETRIC STUDY OF 1D PLASMA PHOTONIC CRYSTALS WITH SMOOTH AND DISCONTINUOUS DENSITY PROFILES

Due to the nature of plasmas, PPCs differ from their solid state counterparts in several ways. First, the plasma components of a PPC can be created at the time of use and can be tuned on microsecond timescales. Second, once a plasma is fully ionized it will not undergo any further phase change, making PPCs resistant to damage in high power applications. Third, the electron density of atmospheric plasmas ($10^{19} - 10^{25}$ m^{-3}) implies a target frequency of PPC devices in the GHz to THz range. Finally, plasmas are inherently diffuse. Instead of the abrupt changes in material properties that occur in solid-state PCs, PPCs provide more gradual changes in density. Many of the proposed PPC devices have density gradient scale lengths that are large compared to the unit spacing. Understanding how these gradients alter transmission properties is essential to predicting PPC behavior.

Several analytical and numerical studies have been undertaken for plasma photonic crystals with non-piecewise constant density profiles. A scattering matrix type method (SMM) was used to calculate transmission for plasmas with step-function, parabolic, sinusoidal, and Gaussian densities by Lontano and Lunin in 1991[52, 53]. More recently, articles have been published on using the plane wave expansion (PWEM), transmission matrix (TMM), and finite-difference time-domain (FDTD) methods on specific 1D density profiles: sinusoidal[54], Gaussian[55], exponentially graded[56, 57], and physically informed density profiles[42].

In this chapter a parametric study of 1D PPCs with smooth and discontinuous density profiles is performed to demonstrate the impact of density gradients on the transmission

characteristics. A linear model similar to that used by Lehmann and Spatschek[42] is outlined for EM waves in an unmagnetized, collisionless, periodically density modulated plasma. A systematic comparison of a smooth density modulated plasma, a discontinuous plasma-vacuum one-dimensional PPC, and two intermediate cases, is conducted. The results are validated against discontinuous Galerkin (DG) method numerical solutions of the same configurations. Band gap maps are then created from derived group velocity data for a range of average plasma frequencies and density modulation amplitudes. The effects of smooth versus discontinuous density profiles on band gap properties are discussed and the origins of these differences are explored by way of a reduced model. This theoretical framework is then used to infer the band gap characteristics of other types of density profiles. The implications for future PPC devices are discussed.

3.1 Propagation of an EM wave in a cold, unmagnetized, 1D periodic plasma

In the cold plasma limit, the propagation of weak EM waves through an infinite periodic plasma can be reasonably approximated by Maxwell's equations coupled to the Drude equation[58, 59], which describes electron motion in a stationary ion lattice (or gas). Solutions to the system can be found through application of Bloch's theorem[60].

In this section the Maxwell-Drude system is solved in a method similar to that described by Lehmann and Spatschek[42] for a one-dimensional, unmagnetized plasma with an arbitrary periodic density profile. The result is an inhomogeneous wave equation with a source term that depends on the current density $\boldsymbol{j}$. The equation is linearized in time and space resulting in an infinite set of linear equations coupled through source terms. In order to explore the difference between smooth and discontinuous density profiles, specific solutions are found for two cases: a sinusoidally modulated density profile, and a square wave density profile.

3.1.1 The linearized inhomogeneous EM wave equation in an unmagnetized, periodic density modulated plasma in 1D

The behavior of electromagnetic waves in a plasma are governed by Maxwell's equations

$$\nabla \times \boldsymbol{E} = -\frac{\partial \boldsymbol{B}}{\partial t}, \quad \nabla \times \boldsymbol{B} = \mu_0 \boldsymbol{j} + \varepsilon_0 \mu_0 \frac{\partial \boldsymbol{E}}{\partial t}$$
$$\nabla \cdot \boldsymbol{E} = \frac{\rho_c}{\varepsilon_0}, \quad \nabla \cdot \boldsymbol{B} = 0. \tag{3.1}$$

where $\boldsymbol{j}$ is the current density, ρ_c is the charge density, and μ_0 and ε_0 are the vacuum permeability and permittivity, respectively. Faraday's and Ampere's laws can be combined to form an inhomogeneous wave equation for $\boldsymbol{E}$,

$$\nabla \times \nabla \times \boldsymbol{E} + \mu_0 \varepsilon_0 \frac{\partial^2 \boldsymbol{E}}{\partial t^2} = -\mu_0 \frac{\partial \boldsymbol{j}}{\partial t}. \tag{3.2}$$

The current density $\boldsymbol{j}$ is defined as

$$\boldsymbol{j} = \sum_\alpha q_\alpha \boldsymbol{v}_\alpha n_\alpha \tag{3.3}$$

where α denotes the species. A wave equation can also be found for the magnetic field, $\boldsymbol{B}$, but has an inhomogeneous part that is a function of $\nabla \times \boldsymbol{j}$. As plasmas used in PPCs are generally cold (< 1 eV), and EM frequencies of interest are well above the typical ion plasma frequency, the time evolution of the plasma current $\boldsymbol{j}$ is assumed to be dictated entirely by electron dynamics, and well approximated by the Drude model[58, 59]

$$\frac{\partial \boldsymbol{j}}{\partial t} = -\frac{e^2 n(\boldsymbol{r})}{m_e} \boldsymbol{E} - \frac{e}{m_e} \boldsymbol{j} \times \boldsymbol{B} - \nu \boldsymbol{j}, \tag{3.4}$$

where e is the electron charge, m_e is the electron mass, ν is the collisional relaxation rate, and $n(\boldsymbol{r})$ is the electron density as a function of space. Written in terms of the electron plasma frequency squared $\omega_{pe}^2 = e^2 n_e / \varepsilon_0 m_e$, and the electron cyclotron frequency $\omega_{ce} = eB_0/m_e$ where B_0 is a constant background magnetic field

$$\frac{\partial \boldsymbol{j}}{\partial t} = -\varepsilon_0 \omega_{pe}^2(\boldsymbol{r}) \boldsymbol{E} - \omega_{ce} \boldsymbol{j} \times \boldsymbol{B}/B_0 - \nu \boldsymbol{j}. \tag{3.5}$$

For the case of an unmagnetized PPC $\omega_{ce} = 0$. To understand the impact of density profile shape as separate from other effects, the collisional relaxation time is assumed to be large relative to the plasma period, i.e. $\omega_{pe} \gg \nu$. This is not necessarily valid in the case of cold, high density plasmas like those needed to achieve THz frequencies, therefore the potential consequences of a finite electron-ion collision frequency are discussed in Sec. 3.4.

As a result of the above assumptions, the contribution of the 2nd and 3rd terms in Eq. (3.5) are negligible. Substituting the Drude equation, Eq. (3.4), into the wave equation, Eq. (3.2), results in a final inhomogeneous wave equation that describes temporal and spatial variations of the electric field $\boldsymbol{E}$ for a spatially varying electron density $n(\boldsymbol{r})$,

$$\nabla \times \nabla \times \boldsymbol{E} + \mu_0 \varepsilon_0 \frac{\partial^2 \boldsymbol{E}}{\partial t^2} = \mu_0 \varepsilon_0 \left(\frac{e^2 n(\boldsymbol{r})}{m_e \varepsilon_0} \right) \boldsymbol{E}. \tag{3.6}$$

An arbitrary periodic 1D density profile $n(x)$ is approximated by a Fourier series

$$n(\boldsymbol{r}) \approx \tilde{n}(x) = n_0 \sum_{\ell} \hat{n}_\ell e^{i\ell g x}, \quad \ell \in \mathbb{Z}, \tag{3.7}$$

where $n_0 = a^{-1} \int_{-a/2}^{a/2} n(x) dx$ is the average plasma density, $g = 2\pi/a$ is the magnitude of the reciprocal lattice vector, a is the lattice period, and the coefficients $\hat{n}_\ell$ can be found by

$$\hat{n}_0 = \frac{1}{n_0} \left(\frac{1}{a} \int_{-a/2}^{a/2} n(x) dx \right) = 1, \tag{3.8}$$

$$\hat{n}_\ell = \frac{1}{n_0} \left(\frac{1}{a} \int_{-a/2}^{a/2} n(x) e^{i\ell g x} dx \right). \tag{3.9}$$

As the periodic plasma density is invariant under discrete translation of the primitive lattice vector such that $\tilde{n}(x + ma) = \tilde{n}(x)$, where m is an integer, Bloch's theorem[60] states that the solution to the electric field $\boldsymbol{E}$ takes the form of plane waves modulated by a function with the same periodicity as the density. Assuming the electric field is perpendicular to the direction of travel, it can be shown that

$$\boldsymbol{E}(\boldsymbol{r}, t) = \sum_k \sum_\ell E_{k-\ell g} e^{i((k-\ell g)x - \omega t)} \, \hat{z}, \quad k \in \mathbb{R}, \tag{3.10}$$

Equations (3.7) and (3.10) are combined with the wave equation, Eq. (3.6), and a Fourier transform is performed in time and space. Rearranging the order of terms for clarity results in a coupled linear system of equations

$$\left(c_0^2k^2 - \omega^2 + \omega_{p0}^2\right) E_k + \omega_{p0}^2 \left(\sum_{\ell=1}^{\infty} \hat{n}_\ell E_{k-\ell g} + \sum_{\ell=-1}^{-\infty} \hat{n}_\ell E_{k-\ell g} \right) = 0, \tag{3.11}$$

where $\omega_{p0} = (e^2 n_0/m_e\varepsilon_0)^{1/2}$ is the electron plasma frequency of the average density, and $c_0 = (\mu_0\varepsilon_0)^{1/2}$ is the vacuum speed of light. Equation 3.11 represents an infinite system of equations for each value of k. Note that the first term is the dispersion relation for EM waves in a uniform plasma with plasma frequency ω_{p0}, while the second is a series of coupling terms with plane waves offset by integer multiples of g and magnitudes proportional to $\omega_{p0}^2\hat{n}_\ell$. Normalizing Eq. (3.11) by the lattice frequency, $\omega_a = 2\pi c_0/a$, results in the following non-dimensional expression

$$\left(K^2 - \Omega^2 + \Omega_{p0}^2\right) E_K + \Omega_{p0}^2 \left(\sum_{\ell=1}^{\infty} \hat{n}_\ell E_{K-\ell} + \sum_{\ell=-1}^{-\infty} \hat{n}_\ell E_{K-\ell} \right) = 0 \tag{3.12}$$

where $K = k/g$ is the lattice normalized wavenumber, $\Omega_{p0} = \omega_{p0}/\omega_a$ is the lattice normalized average plasma frequency, and $\Omega = \omega/\omega_a$ is the lattice normalized EM wave frequency. The solution is independent of the magnitude of E_k therefore it will be considered non-dimensional from here forward.

The following sections explore the form of the coupling terms in Eq. (3.12) for two density profiles: a sine wave modulation on top of a uniform background density, and a square wave composed of a finite Fourier series.

3.1.2 Sinusoidally modulated plasma density

A sinusoidal density modulation is chosen for the smooth PPC case,

$$n(x) = n_0[1 + \chi \sin(gx)], \quad 0 \leq \chi \leq 1 \tag{3.13}$$

where $\chi = (n_{max} - n_0)/n_0$ is the amplitude of the density modulation. Plasmas with a smooth, sinusoidal density profile are likely to occur through laser-plasma interactions[41, 42] or instabilities[38, 61]. This density profile is also a first order Fourier approximation of any periodic profile shape. Fourier coefficients are found by applying Eq. (3.7) to $n(x)$ in Eq. (3.13),

$$\hat{n}_0 = 1, \quad \hat{n}_{\pm 1} = \pm\frac{\chi}{2i}. \tag{3.14}$$

Since $n(x)$ is real valued, the Fourier coefficients $\hat{n}_{-1}$ and $\hat{n}_1$ are complex conjugates. Substituting the coefficients into the general equation (Eq. (3.12)) results in the following normalized system of equations for an EM wave in a sinusoidally modulated 1D PPC

$$(K^2 - \Omega^2 + \Omega_{p0}^2)E_K + \chi\frac{\Omega_{p0}^2}{2i}\left(E_{K-1} - E_{K+1}\right) = 0. \tag{3.15}$$

Here a single pair of terms couple E_K to modes E_{K-1} and E_{K+1}. While the quantity of density Fourier coefficients is finite this does not limit the number of coupled equations, only the number of coupling terms. The number of E_K plane waves is still infinite. In order to solve the system numerically the system is truncated based on criteria outlined in Sec. 3.2.1.

3.1.3 Discontinuous modulated plasma density

The square wave density profile approximates metal-vacuum photonic crystals with their abrupt changes in material properties. It also allows for comparison with existing studies as most assume discontinuous density profiles, despite such profiles being difficult to achieve with plasmas. The density profile has the form

$$n(x) = \begin{cases} n_0(1+\chi), & a(\ell - 1/2) \le x < a\ell \\ n_0(1-\chi), & a\ell \le x < a(\ell + 1/2) \end{cases} \tag{3.16}$$

where χ is defined as $\chi = (n_{max} - n_0)/n_0$. Fourier coefficients are found by applying Eq. (3.7) to $n(x)$,

$$\hat{n}_\ell = \frac{\sin\pi\ell}{\pi\ell} + \frac{\chi}{i\pi\ell}(1 - \cos\pi\ell). \tag{3.17}$$

Written explicitly for terms $|\ell| \leq 5$

$$\hat{n}_0 = 1, \quad \hat{n}_{\pm 1} = \pm\frac{2\chi}{i\pi}, \quad \hat{n}_{\pm 2} = 0,$$
$$\hat{n}_{\pm 3} = \pm\frac{2\chi}{i3\pi}, \quad \hat{n}_{\pm 4} = 0, \quad \hat{n}_{\pm 5} = \pm\frac{2\chi}{i5\pi}.$$

Note that all even Fourier ($j = \pm 2, \pm 4, \dots$) terms are zero. Substituting the Fourier coefficients into Eq. (3.12) results in the following system for a square density profile approximated by a truncated Fourier series (in this case $N = 5$)

$$(K^2 - \Omega^2 + \Omega_{p0}^2)E_K + \omega_{p0}^2 \frac{2\chi}{i\pi}\left[(E_{K-1} - E_{K+1}) + \frac{1}{3}(E_{K-3} - E_{k+3}) + \frac{1}{5}(E_{K-5} - E_{k+5})\right] = 0. \tag{3.18}$$

The magnitude of the Fourier coefficients (and therefore the magnitude of the coupling terms) fall off like $1/\ell$. As convergence of the series is slow, even Fourier approximations with large N have significant error. At $N = 50$, the l^2-norm of the error is still greater than 5%, and does not fall below 1% until N approaches 2000. The effect of Fourier series truncation on band gap prediction is discussed in Section 3.2.1.

3.2 Method of numerical solution and validation against WARPXM plasma code

To solve the linear coupled system described by Eq. (3.12), it is reformulated as an eigenvalue problem and solved for each wavenumber of interest K. As the number of equations is infinite, even when the number of density Fourier coefficients is finite, the system must be truncated to be solved numerically. Bounds are set on the minimum convergence of the solution as a function of system size. Band diagrams are constructed by evaluating the system for a range of values of K. The band diagram for a discontinuous density profile case is validated against solutions found using a cold plasma model solved with the WARPXM Discontinuous Galerkin (DG)[62, 63] code on a Bloch periodic domain[64]. In order to compare

the impacts of smooth versus discontinuous profiles on PPC transmission characteristics, group velocity band gap maps are constructed from sets of band diagrams where either the density modulation amplitude or lattice normalized electron plasma frequency is varied.

3.2.1 Numerical solution of the problem

As developed in the previous section, the linearized system for an EM wave in plasma with a periodic variation in density consists of an infinite set of coupled equations (Eq. (3.12)). Reformulated as an eigenvalue problem for Ω^2,

$$K^2 E_k + \Omega_{p0}^2 \sum_{\ell=-N}^{N} \hat{n}_\ell E_{K-\ell} = \Omega^2 E_k \tag{3.19}$$

or more compactly as

$$\boldsymbol{A}\boldsymbol{E} = \Omega^2 \boldsymbol{E},$$

where $\boldsymbol{A}$ is a Hermitian banded matrix, and the eigenvectors $\boldsymbol{E}$ are frequency space solutions of the electric field for each eigenvalue Ω^2. To truncate the infinite system, a system size limit $M \geq N$ is chosen such that $\boldsymbol{A} \in \mathbb{R}^{(2M+1)\times(2M+1)}$. The matrix $\boldsymbol{A}$ is then expressed in index notation as

$$A_{i=j} = (K+i)^2 + \Omega_{p0}^2, \quad A_{i=j-\ell} = \hat{n}_\ell \Omega_{p0}^2, \tag{3.20}$$

where $i, j = [-M, M], [-M, M]$. The Fourier coefficients $\hat{n}_\ell$ can be found analytically for simple density profiles or numerically for more complex profiles. In index notation the vector $\boldsymbol{E}$ is

$$E_j = E_{K+j}. \tag{3.21}$$

The system is solved numerically for Ω^2 for a set of $K = [0, 1]$. The square root of the eigenvalues correspond to the frequencies of allowable modes, while the eigenvectors E_K correspond to the wavenumber-space structure of the electric field of each mode. When plotted as a function of K, the frequency corresponding to each eigenvalue form the photonic

band structure of the PPC (see Fig. 3.1). The spaces between bands where no allowable mode exists for any value of K are known as band gaps or forbidden regions.

To ensure that the truncated system is fully converged, a method of determining the minimum acceptable value of M is required. The error increases with increasing band number for truncated systems. In this work, the region of interest is confined to the first eight bands, which sets a lower bound on M. Sufficient convergence is defined as the minimum value of M such that the l^2-norm of the normalized difference between the M and $M-1$ solution for the eighth band is less than 10^{-6}, or

$$||\Delta\Omega_{8,M}||_2 = \sqrt{\frac{\sum_K |\Omega_{8,M} - \Omega_{8,M-1}|^2}{\sum_K |\Omega_{8,M}|^2}} < 10^{-6}. \tag{3.22}$$

3.2.2 Validation of the analytical model with a nonlinear plasma model solved using the WARPXM code

WARPXM, an unstructured Discontinuous Galerkin multi-physics plasma code developed at the University of Washington[63], is used to evaluate the equivalent problem as a system of normalized hyperbolic PDEs

$$\frac{\partial \boldsymbol{p}_e}{\partial t} = \left(\frac{L}{\delta_p}\right)\left(\frac{1}{A_e}\right)\boldsymbol{p}_e \times \boldsymbol{B}, \tag{3.23}$$

$$\frac{\partial \boldsymbol{E}}{\partial t} = (\omega_p\tau)^2\left[\left(\frac{\delta_p}{L}\right)^2 \nabla \times \boldsymbol{B} - \left(\frac{\delta_p}{L}\right)\left(\frac{1}{A_e}\right)\boldsymbol{p}_e\right], \tag{3.24}$$

$$\frac{\partial \boldsymbol{B}}{\partial t} = -\nabla \times \boldsymbol{E}, \tag{3.25}$$

where $\boldsymbol{p}$, $\boldsymbol{E}$, $\boldsymbol{B}$, and t are normalized by reference values $p_0 = m_p n_0 c_0$, $E_0 = c_0 B_0$, $B_0 = (\mu_0 m_p n_0 c_0^2)^{1/2}$, and $\tau = L/c_0$, respectively. The reference density, n_0, is chosen based on typical density values, L is the problem length scale, m_p is the proton mass, and c_0 is the vacuum speed of light. The nondimentional parameters are: δ_p/L, the normalized proton skin depth, $A_e = m_e/m_p$, the proton normalized electron mass, and $\omega_p\tau$, the normalized

proton plasma frequency. Ions are assumed stationary to be consistent with the analytical model described in Sec. 3.1.

The WARPXM code computes the evolution of the electron momentum and electric and magnetic fields by solving Eqs. (3.23), (3.24), and (3.25). A solution is initialized that describes a propagating TE, TM, or TEM wave. To simulate an infinitely periodic system, Bloch boundary conditions[64] are implemented. The WARPXM code applies boundary conditions by setting the value of virtual nodes at the boundaries. The left and right virtual boundary nodes, q_R^v and q_L^v respectively, are functions of the opposite boundary node value, q_L and q_R, and a phase shift, ψ,

$$q_R^v = q_L e^{-i\psi}, \tag{3.26}$$

$$q_L^v = q_R e^{i\psi}, \tag{3.27}$$

where $\psi = ka$, and i here denotes the unit imaginary number. The boundary conditions allow for the representation of an infinite periodic plasma with period a, while permitting EM waves with wavenumbers other than integer multiples of the inverse domain length. Simulations are performed for each k value of interest. Note that real and imaginary components of the electric and magnetic fields are needed for the Bloch boundary conditions, so Eqs. (3.23), (3.24), and (3.25) are complex-valued equations.

Electric and magnetic field values are sampled at regular time intervals for several points in the domain that do not fall on any axis of symmetry. This sampling strategy mitigates inadvertently sampling values at or near field nulls which could lead to weak detection of particular modes. A fast Fourier transform (FFT) algorithm is then applied to the data, and the spectra are averaged over all sampled points.

Band diagrams are assembled by running simulations with different wavenumbers k in the range of interest. Plotting the logarithm of the spectral intensity produces the band diagram from the nonlinear plasma simulations, as is shown in Figs. 3.1 and 3.2, using the real component of the electric field. The band diagram using the imaginary component gives

a similar result. A total of 41 simulations, each with a different value of k, adequately resolve the wavenumber space. Simulations to generate a complete band diagram take approximately five hours using a single core on a modest workstation.

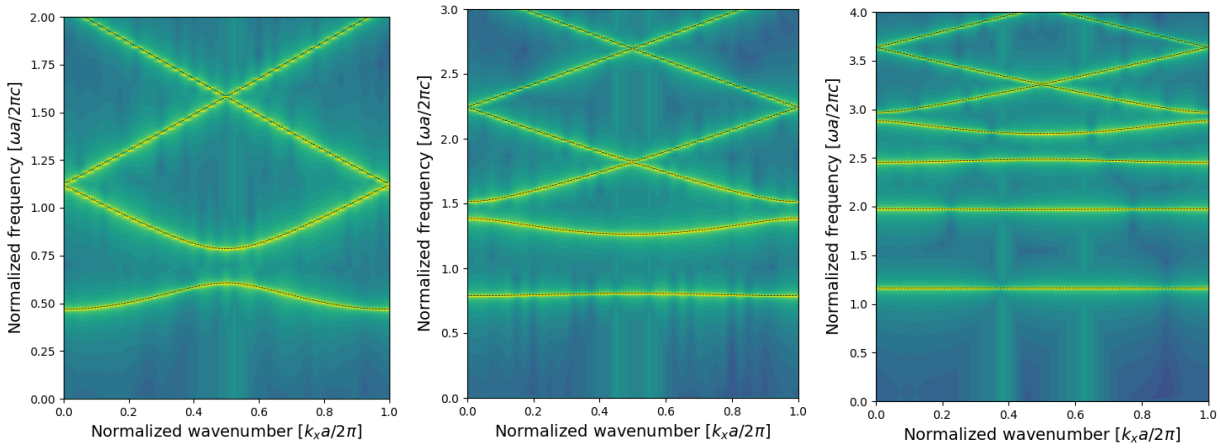

Figure 3.1: Comparison of band diagrams generated by solving the nonlinear plasma system, Eqs. (3.23)-(3.25), using WARPXM (color contours indicate magnitude of spectra) and the analytical model described in Sec. 3.1 (dashed lines) for a sine plasma density profile with $\Omega_{p0} = 0.5$ (left), $\Omega_{p0} = 1$ (middle), and $\Omega_{p0} = 2$ (right). Note that the scale of the y-axis is different for each panel.

The analytical and numerical band diagrams are compared for each band and the l^2-norm of the relative difference is calculated for each band i,

$$||\Delta\Omega^i||_2 = \sqrt{\frac{\sum_k |\Omega^i_{anal} - \Omega^i_{num}|^2}{\sum_k |\Omega^i_{anal}|^2}}. \tag{3.28}$$

Calculated errors for five different density profile cases are shown in Table 3.1. In all cases there is good agreement as the error is on the order of the frequency resolution of the simulation. Large plasma frequencies to lattice frequency ratios Ω_{p0}, and square density profiles generally produce larger errors. This is also reflected in the increase in system size needed to sufficiently resolve the problem.

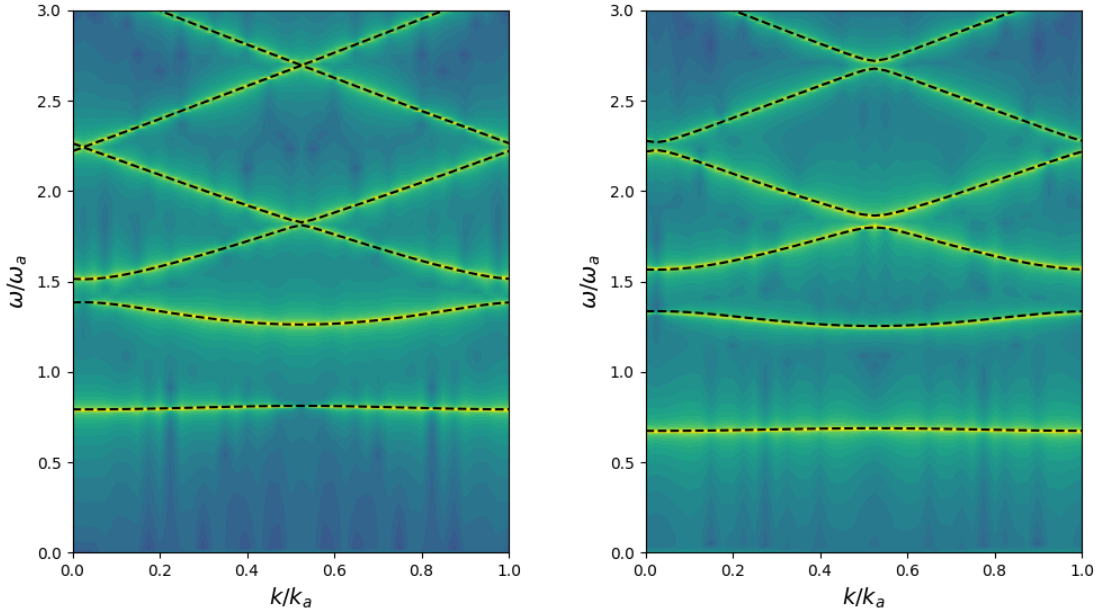

Figure 3.2: Comparison of band diagrams generated by solving the nonlinear plasma system, Eqs. (3.23)-(3.25), using WARPXM (color contours indicate magnitude of spectra) and the analytical model described in Sec. 3.1 (dashed lines) for a sine plasma density profile with $\Omega_{p0} = 1$ and $\chi = (n_{\max} - n_{\text{avg}})/n_{\text{avg}} = 1$ (left), and for a square profile with $\Omega_{p0} = 1$ (right).

3.2.3 Construction of velocity band gap maps

One of the key advantages of plasma photonic crystals over solid state PCs is their tunability. Where parametric studies are useful for device design in dielectric or metal PCs, for plasma PCs they can also be used to describe the operational regime of a single device. As the band gap is generally the most important characteristics of a PC, band gap maps[21] are a convenient representation of a PC's performance.

In solid state PCs, the unitless design parameters most used are the dielectric contrast,

Table 3.1: The l^2-norm of the relative difference between the analytical and WARPXM results for the first five bands, $||\Delta\Omega^i||_2$ (see Eq. (3.28)). In all cases the absolute difference is on the order of the simulation frequency resolution, $\omega_{res}/\omega_a = a/c_0T = 0.25 \times 10^{-2}$, where T is the simulation total run time. System size is chosen by the condition in Eq. (3.22).

		Solution difference, $||\Delta\Omega^i||_2 \times 10^{-2}$				
Density profile	System Size	Band 1	Band 2	Band 3	Band 4	Band 5
Sine[1], $\Omega_{p0} = 0.5$	13×13	0.30	0.31	0.13	0.10	0.06
Sine, $\Omega_{p0} = 1.0$	13×13	0.39	0.25	0.16	0.08	0.07
Sine, $\Omega_{p0} = 2.0$	17×17	0.87	0.36	0.05	0.12	0.09
Square[2], $\Omega_{p0} = 1.0$	21×21	0.60	0.94	0.07	0.09	0.05
Square, $\Omega_{p0} = 2.0$	25×25	0.76	0.77	1.18	0.20	0.41

$\varepsilon_{\text{high}} : \varepsilon_{\text{low}}$, and the fill fraction $f = d_{\text{high}}/a$, where d_{high} is the width of high dielectric constant layer, and a is the lattice spacing. In plasma PCs the plasma density is most often the easiest and fastest tunable parameter, whereas fill fraction is either fixed or a secondary effect that is not easy to control independently of plasma density. For the study of plasma PCs, the primary unitless parameters of interest are chosen to be density modulation amplitude, $\chi = (n_{\max} - n_{\text{avg}})/n_{\text{avg}}$, and the lattice normalized electron plasma frequency of the average density, $\Omega_{p0} = \omega_{pe0}/\omega_a$.

Photonic crystal band gap maps are traditionally formed by plotting band gap edges as a function of either fill fraction or dielectric contrast. Band gap edges can be found either through dispersion data[21] or transmission spectra[65], though density of states contours have also been used[66, 67]. In this work, band gap maps are created by calculating the group velocity for individual bands, which has the added benefit of including more useful information on transmission properties around the band gap edges.

Band gap maps are generated by calculating a series of band diagrams (as in Fig. 3.3), with each band diagram changing the parameter of choice by some small amount. Each band gap map presented in Sec. 3.3 is constructed from 200 band diagrams. Group velocity, $v_g = \partial\Omega/\partial K$, is found by calculating the slope at each value of K from 0 to 1/2 using the central difference operator for interior K values and one-sided difference operators at the boundaries. The calculated slopes are binned by frequency Ω. In forbidden regions where no slope exists the bin is assigned to NaN. Group velocities are normalized to the speed of light and plotted as color contours, and band gaps appear as blank spaces, as seen in Figs. 3.4, 3.5, and 3.8.

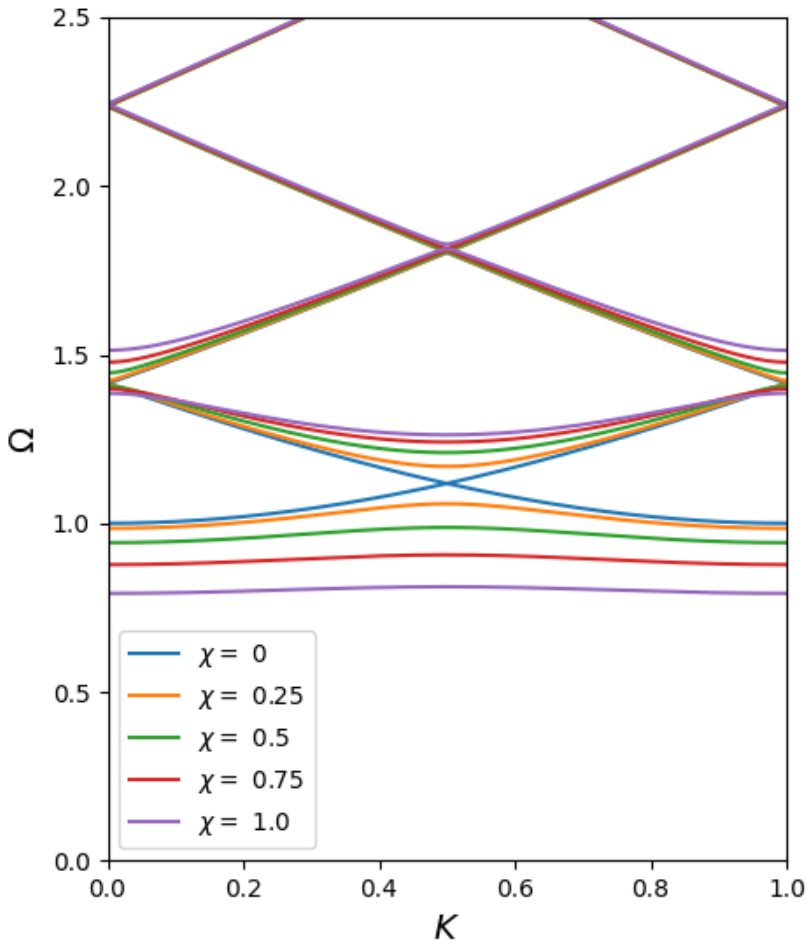

Figure 3.3: Band diagram for a sinusoidally modulated density profile with lattice averaged plasma frequency $\Omega_{p0} = 1$ and modulation amplitude varying from $\chi = 0 - 1$.

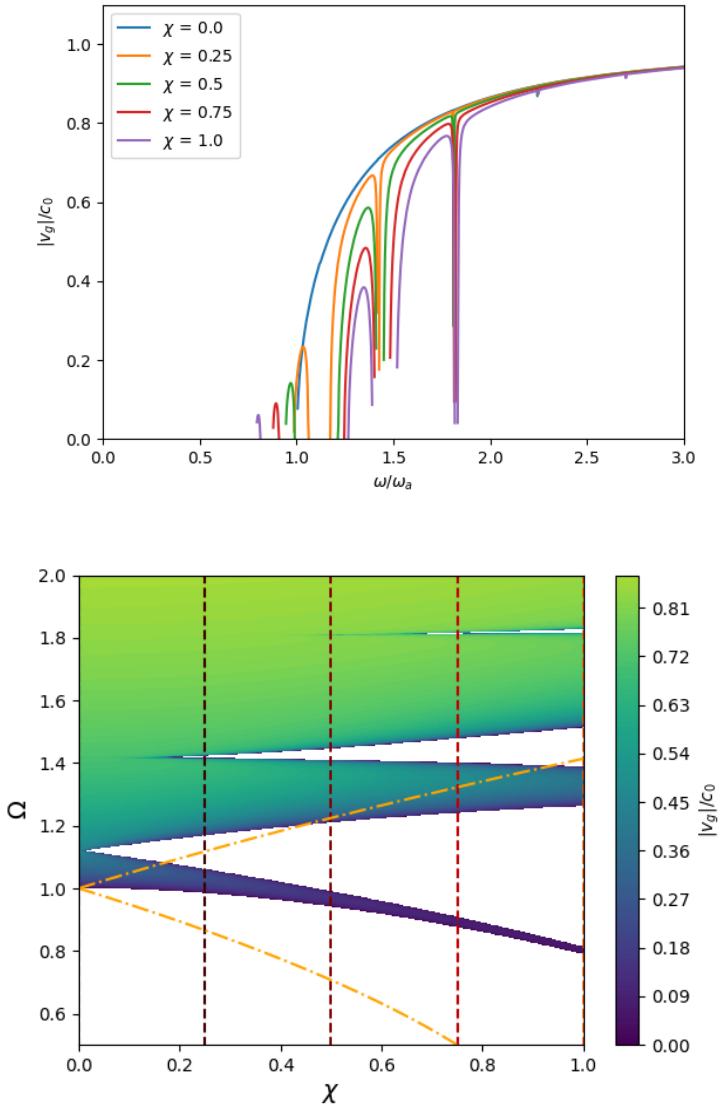

Figure 3.4: (Top) Group velocity for a smooth, sinusoidally modulated density profile with modulation amplitudes varying from 0 to 1, calculated from band diagrams in Fig. 3.3. (Bottom) Contours of group velocity for the same case, which provide a band gap map, which facilitates interpretation of the effects of modulation amplitude on band gaps. Normalized average plasma frequency $\Omega_{p0} = 1$ for all cases. Vertical dashed lines indicate locations of band diagrams in Fig. 3.3 and left panel at $K = 0.25$, 0.5, and 0.75 respectively, and orange dashed-dotted lines indicate locations of plasma frequencies at minimum and maximum densities. Band gaps extend well beyond the maximum plasma frequency.

3.3 Band gap map comparison of smooth and discontinuous density profiles

Group velocity band gap maps are created for the smooth and discontinuous density profiles using the procedures described in Sec. 3.2. The area of interest is confined to lattice normalized average density plasma frequencies between $\Omega_{p0} = 0 - 3$ and lattice normalized EM wave frequencies of $\Omega = 0 - 4$, as this region is sufficient for capturing the dominate band gap features. In this section, the smooth, sinusoidally modulated density profile is explored by varying both χ and Ω_{p0}. The smooth density profile band gap maps are then contrasted with the band gap maps of the discontinuous density profile. The origins of these differences are explored in Sec. 3.4.

3.3.1 Sinusoidally modulated density profile

By plotting contours of the group velocity for a sinusoidally modulated density profile with modulation amplitudes varying from $\chi = 0$ to 1, and $\Omega_{p0} = 1$, a band gap map is produced in Fig. 3.4 that facilitates understanding of the impact of modulation amplitude on photonic bands. The blank contour indicates the absence of bands, or band gaps. The left boundary of the plot, at $\chi = 0$, represents the dispersion of a uniform plasma. The orange dash-dot lines represent the plasma frequency of the maximum and minimum density regions, respectively. As the modulation amplitude increases, the first band gap appears just above the plasma frequency at $\Omega \approx 1.1$. A second and third band gap appear by $\chi = 0.5$, at $\Omega \approx 1.4$ and 1.8 respectively. At $\chi = 1$ the dispersion of the density modulated plasma has deviated significantly from the dispersion of a uniform plasma ($\chi = 0$). Note that all band gaps begin above the plasma frequency of the maximum density.

The gap map in Fig. 3.5 shows the effect of varying the plasma frequency of the average density Ω_{p0}, for two density profiles. Color contours indicate a sinusoidally modulated density profile with a maximum modulation amplitude ($\chi = 1$) and gray shading indicates a uniform plasma ($\chi = 0$) with the same Ω_{p0}. The orange dashed-dotted line in Fig. 3.5 indicates the

plasma frequency of the maximum density for the sinusoidally modulated density profile. The minimum density and plasma frequency are zero for all cases.

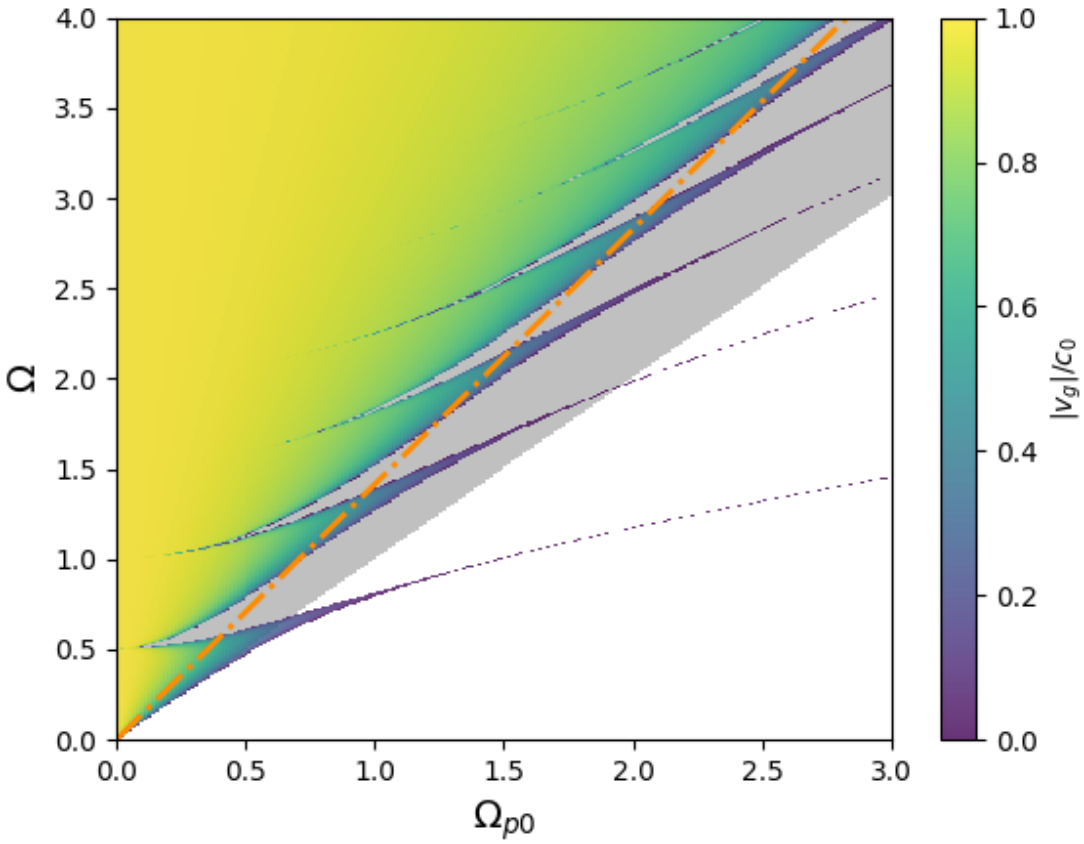

Figure 3.5: Contours of group velocity as a function of the plasma frequency of the average density Ω_{p0} for a sinusoidally modulated (color contours) and uniform plasma (gray contours), or $\chi = 1$ and $\chi = 0$, respectively. The color bar indicates group velocity normalized by c_0. Plasma frequency of the maximum density for the sinusoidally modulated plasma is indicated by the dashed-dotted orange line. Band gaps for the sinusoidally modulated plasma extend well above the maximum plasma frequency.

Several differences between the density modulated and uniform plasma profiles can be readily identified. Despite having the same average plasma frequency, forbidden regions in the density modulated case extend above not only the average plasma frequency, but also above the plasma frequency of the maximum density (upper orange dashed-dotted line). The band gap map provides clues to the origin of individual band gaps: when extrapolated to the left axis, each band gap can be seen to start at half lattice frequency intervals, corresponding to band diagram intersections at $K = 0$ and 0.5. These band gaps continue for EM wave frequencies many times the lattice frequency.

3.3.2 Dirichlet-type density profile

A Dirichlet kernel density profile (see left panel of Fig. 3.6) is the superposition of a finite number of sinusoidal density profiles with the same amplitude. While not necessarily a physically motivated case, the profile is smooth, and the density Fourier content demonstrates an edge case (constant valued Fourier coefficients). In the right panel of Fig. 3.6, a gap map is constructed for a Dirichlet-type density profile with six Fourier coefficients with constant value $\hat{n}_\ell = n_0/3$. In contrast to the gap map for the sinusoidally modulated case (Fig. 3.5), the first six band gaps start at low values of average plasma frequency, while the seventh band gap starts at much higher values of average plasma frequency. The lower band gaps expand uniformly with increasing plasma frequency and track closely with the uniform plasma cutoff (gray contours).

3.3.3 Sawtooth density profile

A sawtooth density profile (see left panel of Fig. 3.7) combines both a linearly increasing plasma density region, and a discontinuity. Like the Dirichlet-type density profile, the sawtooth profile is not physically motivated, but contains interesting Fourier content (coefficients of the density profile fall off like $\hat{n}_\ell \propto 1/\ell$). The gap map in Fig. 3.7 is constructed from a

finite Fourier approximation of sawtooth density profile with N = 5 and $\chi = 1$. In this case, the first five band gaps start at lower values average plasma frequency than the sinusoidal case, but higher than the Dirichlet case. Also, lower band gaps expand faster than higher band gaps. Overall, the shares similarities with both the sinusoidal and Dirichlet-type cases, and sits between the two in both starting band gap plasma frequency an band gap width.

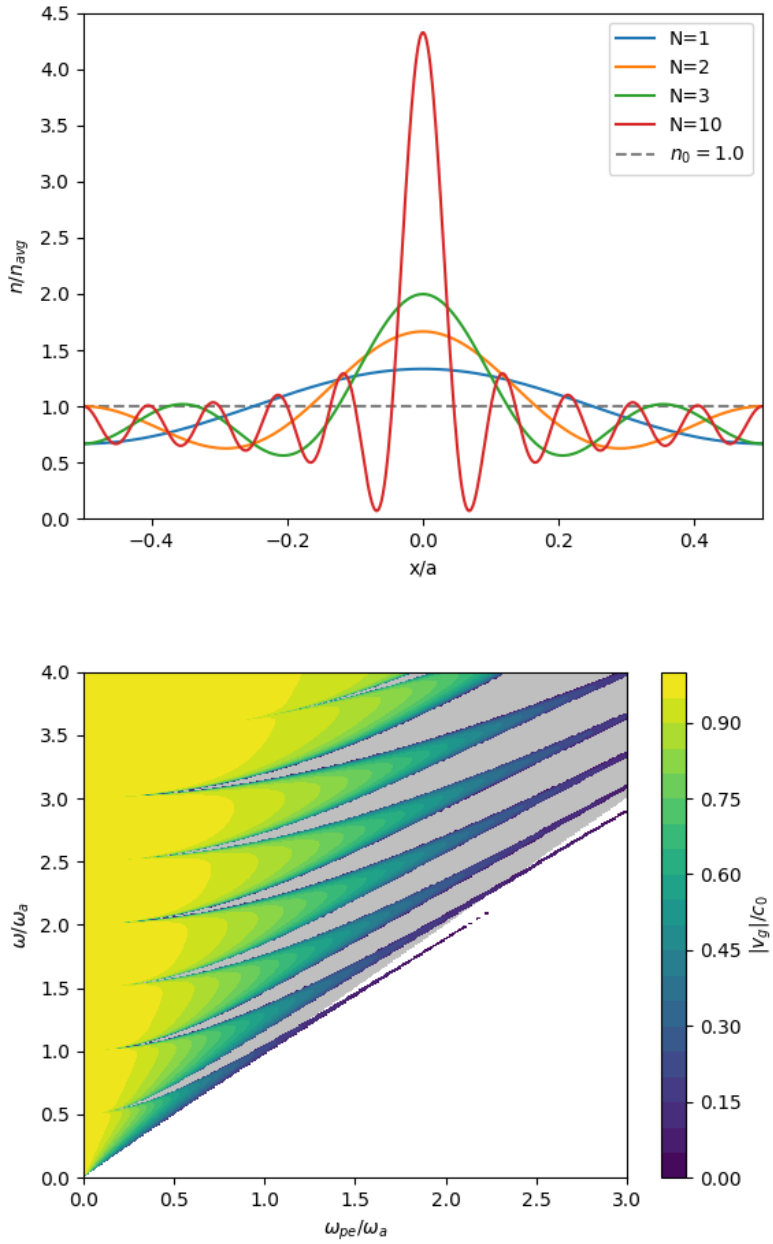

Figure 3.6: (Top) A Dirichlet-type density profile with 1, 2, 3, and 10 finite Fourier terms. In each case, all Fourier terms have the same magnitude $|\hat{n}_\ell| = 1/3$. (Bottom) Contours of group velocity as a function of the plasma frequency of the average density Ω_{p0} for a Dirichlet-type density profile with N = 6 (color contours) and uniform plasma (gray contours). The color bar indicates group velocity normalized by the vacuume speed of light c_0.

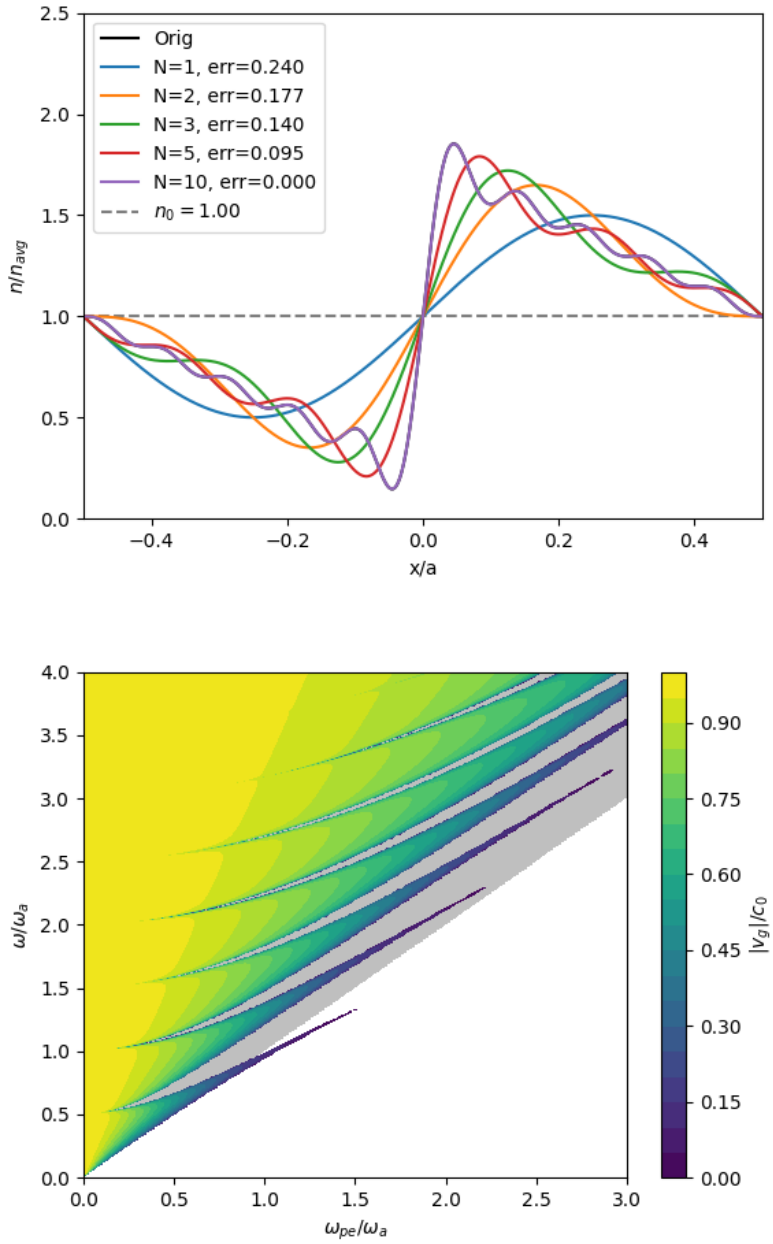

Figure 3.7: (Top) A sawtooth density profile approximated with 1, 2, 3, 5, and 10 finite Fourier terms. Fourier coefficients of the density profile fall off like $\hat{n}_\ell \propto 1/\ell$. (Bottom) Contours of group velocity as a function of the plasma frequency of the average density Ω_{p0} for a finite Fourier approximation of a sawtooth density profile with N = 5 (color contours) and uniform plasma (gray contours). The color bar indicates group velocity normalized by the vacuume speed of light c_0.

3.3.4 Discontinuous, square density profile

The square density profile, as described in Sec. 3.1.3, represents the fully discontinuous case with not finite density gradients. The dispersion of a discontinuous and smooth density profile are compared in the band gap map in Fig. 3.8. The discontinuous density profile gap map (color contours) is overlayed on the smooth density profile gap map from Fig. 3.5 (gray shading). Both profiles have the same modulation amplitude $\chi = 1$ and a filling fraction of $f = d_{plasma}/a = 0.5$, corresponding to equal width regions of low and high density.

There are notable similarities between the band gap maps for both cases. The same number of band gaps are present in both the discontinuous and smooth cases, and the band gaps begin at similar frequencies. In fact, the first band gap, beginning at $\Omega = 0.5$, is almost identical for $\Omega_{p0} \leq 0.5$.

Despite the band gap maps for the discontinuous and smooth density profiles having a similar general structure, major difference are evident. The first significant difference is the appearance of forbidden islands in the discontinuous case at large Ω. The origin of these islands will be explored in Sec. 3.4. Furthermore, the forbidden islands alternate in size and extent, whereas the band gaps in the smooth density profile case all have a similar size and shape. The second major difference are the widths and central frequencies of band gaps at large Ω_{p0}. While the band gaps for the smooth density profile continue to increase in Ω with increasing Ω_{p0}, the band gaps for the discontinuous profile appear to asymptote. This can be explained by understanding that the narrow bands between band gaps at large Ω_{p0} correspond to stationary modes trapped in density troughs. Similar to an electron in a potential well, the frequency of the trapped modes is a strong function of potential well shape. Rectangular potential wells have stationary mode frequencies independent of potential well depth beyond a minimum. In contrast, the sides of shaped wells steepen with increasing depth, causing trapped mode frequencies to change.

Just as the smoothly modulated plasma is not well approximated by a homogeneous

plasma of the same average density, the discontinuous density profile plasma is not well approximated by a smoothly modulated plasma with the same minimum and maximum densities. This is especially true at higher frequencies. In the next section, the origins of these differences is explored.

3.4 Understanding the origins of band gaps through a reduced model

Many of the differences between the band gap characteristics of the smooth and discontinuous density profiles can be explored through studying the interaction of pairs of electromagnetic wave modes. The infinite system in Eq. (3.12) is truncated to include only two waves: E_K and $E_{K\text{-}j}$, where $j \geq 1$ and indicates the number of the band gap of interest. All other modes are set to zero, reducing the system to two coupled equations

$$\begin{aligned} \left(K^2 - \Omega^2 + \Omega_{p0}^2\right) E_K + \hat{n}_j \Omega_{p0}^2 E_{K\text{-}j} = 0, \\ \left((K-j)^2 - \Omega^2 + \Omega_{p0}^2\right) E_{K\text{-}j} + \hat{n}_{\text{-}j} \Omega_{p0}^2 E_K = 0. \end{aligned} \tag{3.29}$$

In the case of a uniform plasma, $\hat{n}_j = \hat{n}_{\text{-}j} = 0$, the equations become decoupled (see the blue line in Fig. 3.9). The first equation is the dispersion relation for EM waves traveling in a cold, homogeneous plasma. The second is the same dispersion relation, shifted in K by j. The two dispersion relations intersect at $K = j/2$ where the E_K wave has a positive group velocity, and the $E_{K\text{-}j}$ wave's group velocity is negative. The two waves are counter propagating, but not interacting.

For non-zero values of $\hat{n}_{\pm j}$, the system is coupled and the counter propagating waves begin to interact. In Fig. 3.9, the orange, green, and red lines show the reduced model solution for $\chi = 0.1$, 0.5 and 1, respectively. Even at small modulation amplitude coupling between forward and backward propagating modes leads to a band gap in the vicinity of the band intersection. Physically, this translates to reflection of all frequencies within the band gap. With increasing modulation amplitude this reflection band increases dramatically, and distorts the two original bands from the unmodulated case.

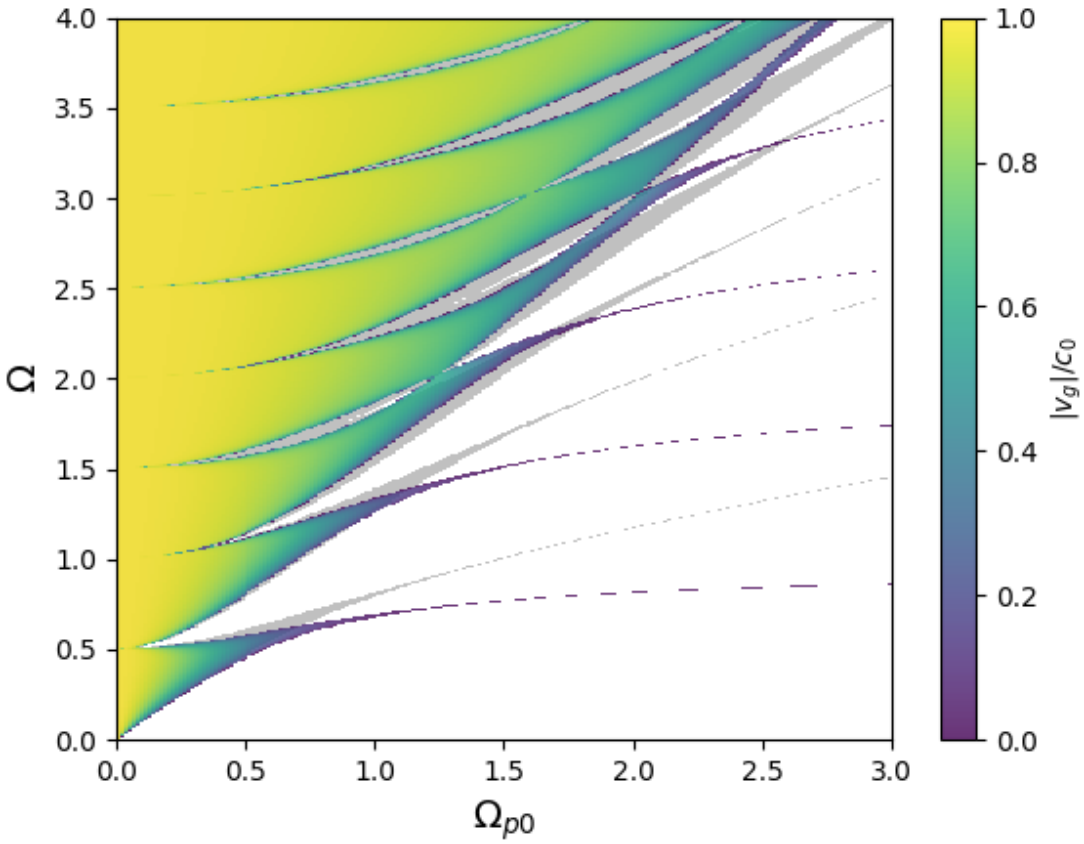

Figure 3.8: Contours of group velocity for a discontinuous and smooth density profile. The discontinuous density profile gap map (color contours) is overlayed on the smooth density profile gap map from Fig. 3.5 (gray shading). Both profiles have the same modulation amplitude $\chi = 1$ and a filling fraction of $f = d_{plasma}/a = 0.5$. The plasma frequency of the average density, Ω_{p0}, is shown in the x-axis. Contour colors indicate group velocity normalized by c_0. The band gap maps for discontinuous and smooth density profiles differ significantly.

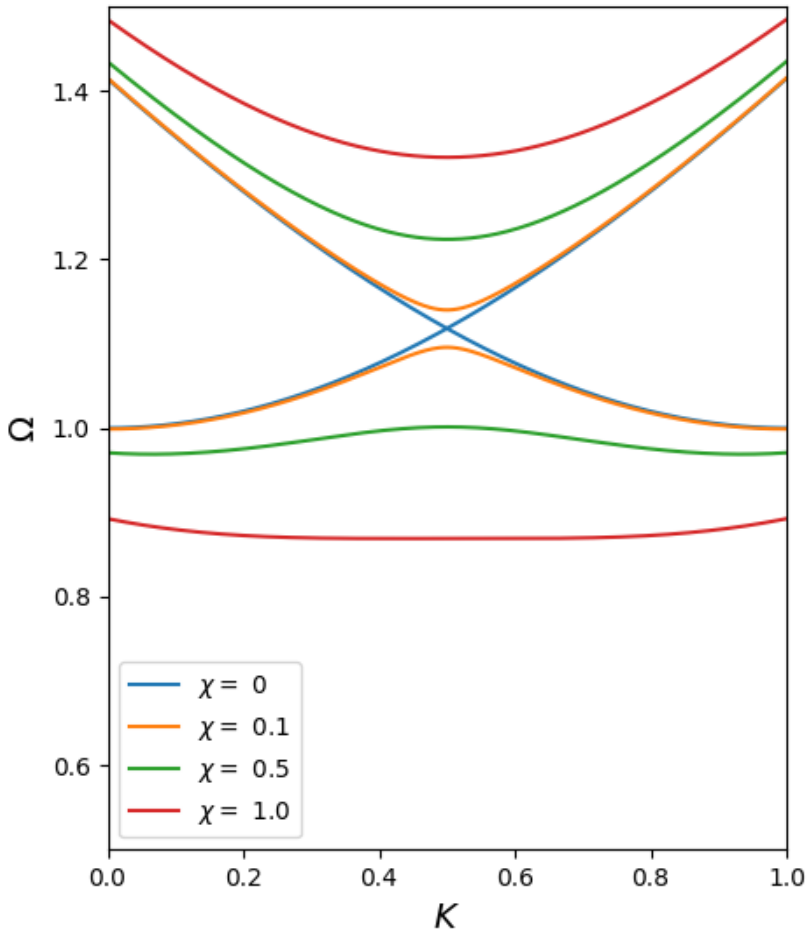

Figure 3.9: Band diagram given by the reduced model for a uniform plasma (blue) and sinusoidally modulated plasma with modulation amplitudes of $\chi = 0.1$ (orange), $\chi = 0.5$ (green) and $\chi = 1$ (red). Lattice normalized plasma frequency of $\Omega_{p0} = 1$ for all cases. Increased density modulation amplitude leads to increased mode coupling around the band intersection at $K = 0.5$, generating, and then expanding the band gap at $\Omega \approx 1.1$.

The upper and lower bounds of the band gap can be found analytically given the system in Eq. (3.29). Solving for Ω at $K = j/2$, and using the fact that that $\hat{n}_{-j}$ is the complex conjugate of $\hat{n}_{+j}$, results in two values for Ω,

$$\Omega_{\pm j} = \sqrt{\Omega_{p0}^2(1 \pm |\hat{n}_j|) - (j/2)^2} \tag{3.30}$$

where Ω_{+j} and Ω_{-j} indicate the normalized frequency of the upper and lower bounds of the jth band gap, respectively. Each band gap j is a function of Ω_{p0} and the magnitude of the jth density Fourier coefficient, $|\hat{n}_j|$.

In Fig. 3.10, the reduced model predictions of the cut-off region (blue) and band gaps (orange) for the smooth density profile are compared against the converged numerical solution (gray). At low normalized plasma frequencies, $\Omega_{p0} < 0.5$, the two solutions are very similar, indicating two-mode wave coupling is dominant in this region.

As the lattice normalized plasma frequency increases, the solutions increasingly diverge. Not only does the reduced model over predict the width and average frequency of band gaps at these higher frequencies, but it fails to predict higher band gaps entirely. This can be understood from the dependence of Eq. (3.30) on $|\hat{n}_j|$. The sinusoidally modulated case has only non-zero values for $\hat{n}_{\pm 1}$, resulting in the reduced model predicting only one band gap. In reality, more than two modes are present and interact through higher order coupling. In the band gap map, this higher order coupling appears as harmonics of the first band gap repeated at integer multiples of half the lattice frequency $\Omega_a/2$.

Figure 3.11 compares the reduced model and converged solution for the discontinuous density profile. In contrast to the smooth density profile case, some (but not all) of the higher band gaps are predicted by the reduced model. This is expected as the discontinuous density profile has non-zero density Fourier coefficients for odd values of j; therefore, the reduced model predicts finite odd band gaps. Reduced models of the Dirichlet and sawtooth density profiles (not shown) support this conclusion as band gaps associated with non-zero Fourier coefficients are predicted.

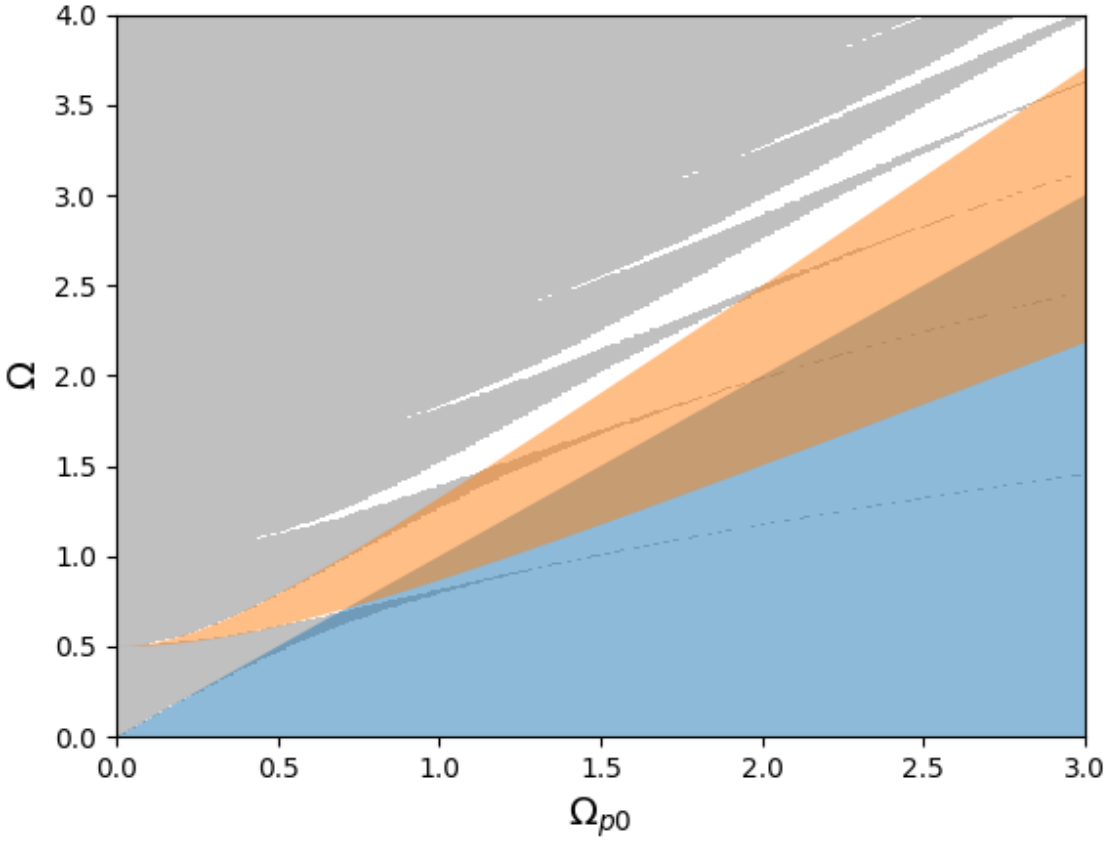

Figure 3.10: The smooth density profile gap map (gray) is overlaid with predictions by the two-mode reduced model for the cut-off region (blue) and first band gap (orange). Models agree well for $\Omega_{p0} < 0.5$, but depart with increasing Ω_{p0}. Higher band gaps are not predicted by the reduced model as they result from higher order coupling effects.

The reduced model again well approximates the converged model for smaller values of Ω_{p0}, but diverges with increasing Ω_{p0}. Also like the smooth case, not all band gaps are predicted by the reduced model. These unpredicted band gaps are all even (band gaps 2, 4, and 6 in Fig. 3.11), and are distinguishable from the predicted band gaps by beginning later,

at higher values of Ω_{p0}. Again, these unpredicted band gaps can be understood as harmonics that results from higher order coupling.

The most prominent difference between the smooth and discontinuous profile band gap maps, the forbidden islands, are not predicted by the two-mode reduced model. Therefore the band gap islands appear to be the result of interactions between first-order mode coupling and higher order harmonics. Interestingly, when density profiles have both even and odd non-zero density Fourier content (such as Gaussian or saw-tooth profiles) no forbidden islands are formed.

The sinusoidally modulated and discontinuous density profiles represent useful limits of possible density profiles, while the Dirichlet and sawtooth profiles represent intermediate cases with predictable Fourier content. Many proposed PPC devices include both gradual changes in density and abrupt changes due to dielectric components or barriers. Given that the Fourier content of the density profile is the ultimate origin of band gap features, choices can be made in advance to achieve desirable transmission characteristics. In cases where only the first band gap is of interest, sinusoidal density profiles are sufficient. Where higher band gaps are desired in order to target frequencies well beyond achievable lattice spacing and plasma frequencies, dielectric barriers or low fill fraction density profiles may be necessary in order to introduce higher Fourier content.

Dissipative effects have not been included in this study, though they are likely to be non-negligible in THz plasmas. Prior work on dissipation in both metallic and plasma PCs[43, 68] have shown that absorption of EM wave energy by a dissipative material peaks at frequencies with a slow group velocity. The physical interpretation is that slow moving waves have more time to interact and transfer energy than fast moving waves. As a result, increasing the electron relaxation rate does not lead to a change in the band structure per se, but does increase absorption around band gap edges leading to the appearance of a wider band gap in transmission spectra.

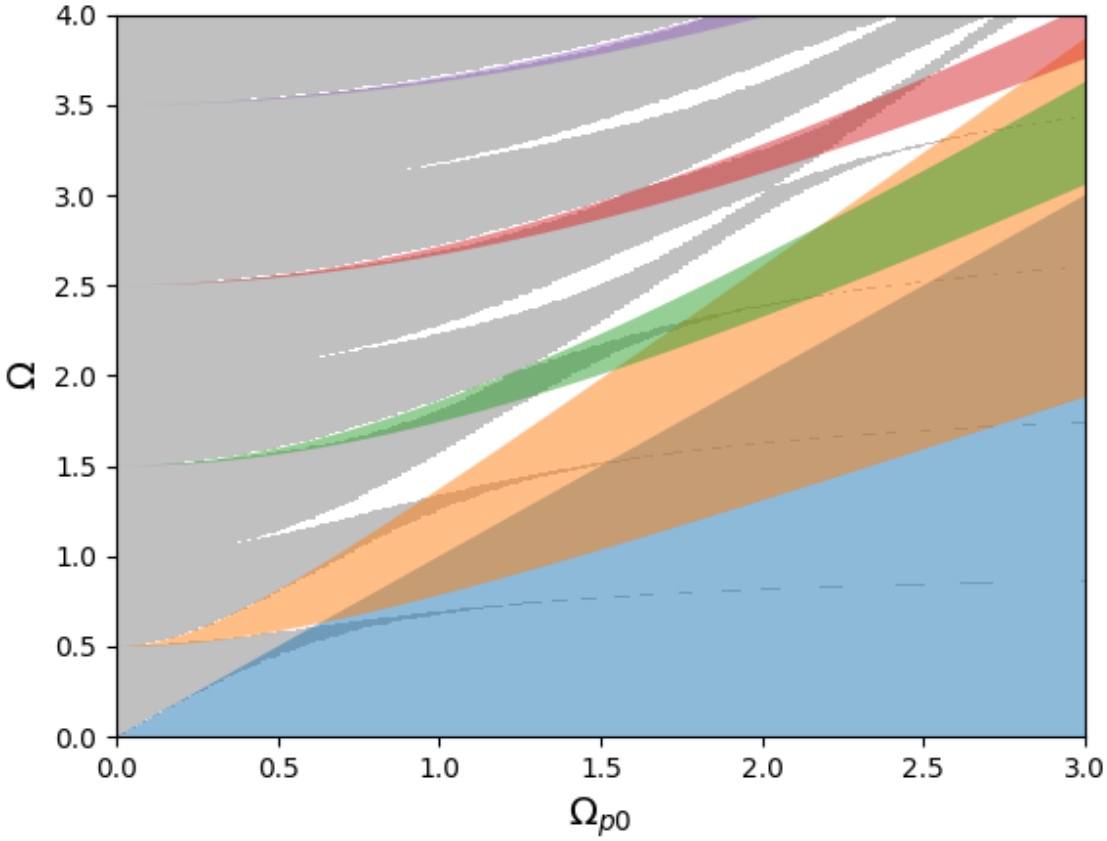

Figure 3.11: Discontinuous density profile gap map (gray) is overlaid with predictions of the two-mode reduced model. This includes the cut-off region (blue), and the first (orange), third (green), fifth (red), and seventh (purple) band gaps. As in the smooth density profile case, models agree well only for $\Omega_{p0} < 0.5$. The formation of forbidden islands in the band gap map is not predicted by the reduced model, and is a result of the interaction of three or more modes. The even-numbered band gaps are also not predicted as they result from higher order coupling effects not captured by the reduced model.

3.5 Conclusions

PPCs have a smoothly varying density structure as compared to solid state PCs which have discontinuous changes in material properties. A systematic understanding of the effect of smooth and discontinuous density profiles on transmission properties of PPCs is important to understanding and designing future PPC devices.

In this work, two one-dimensional density profiles are chosen that represent the limiting cases of smooth and discontinuous PPCs. Band diagrams are constructed for each assuming an un-magnetized, non-dissipative, cold plasma with stationary ions. Group velocity band gap maps are then assembled from sets of band diagrams for a range of modulation amplitudes and lattice normalized plasma frequencies, and compared for both density profiles. The results are further examined through a reduced model to elucidate the origins of major band gap features.

Several general trends are identified. First, two profiles with the same lattice constant and average, maximum, and minimum densities can have different band gap behavior. Second, the width of higher-order band gaps is strongly correlated with density profile Fourier content. Stated more explicitly, the frequency and width of the j-th band gap are a function of the lattice normalized plasma frequency and the magnitude of the j-th Fourier component. Third, high-order interactions of band gaps can lead to complex effects like forbidden islands, where band gaps open and close with increasing plasma frequency.

These results have interesting implications for the design of future PPC devices. Density profile shape becomes yet another parameter that can be tuned to achieve desired results. By designing the Fourier content of a density profile, through finer control of plasma shape or inserting solid components to create discontinuities, higher order band gaps can be directly controlled.

Group velocity band gap maps prove to be a powerful technique in both PPC design and understanding the operating regime of a single device. While the system linearization

technique used in this study to generate band diagrams is optimized for cold, un-magnetized, and non-dissipative plasmas, the group velocity band gap map is agnostic to calculation method. Group velocity band gap maps can either be generated directly for PPCs that include additional physics, or single band diagrams can be compared to these results for a deeper understanding in cases where computations are too costly.

This technique is also applicable to PPCs of higher dimensions. In the next chapter, the transmission properties of smooth and discontinuous two-dimensional PPCs is explored.

Chapter 4

PARAMETRIC STUDY OF 2D PLASMA PHOTONIC CRYSTALS WITH SMOOTH AND DISCONTINUOUS DENSITY PROFILES

In Chapter 3 a linear model is derived for a one-dimensional cold-plasma photonic crystal with an arbitrary density profile and is used to elucidate the impact of smooth versus discontinuous density profiles on 1D PPCs. In this chapter, the same model is extended to two-dimensional PPCs with arbitrary density profiles for both TM and TE polarization.

Two-dimensional PPCs differ from their one-dimensional counterparts in a number of ways. First, dispersion characteristics are a strong function of EM wave polarization. As a result, complete band gaps (forbidden transmission regions for all polarizations and propagation directions) are rare. Second, TE polarized waves excite trapped plasma modes on the surface of plasma columns leading to absorption bands near the plasma frequency. These plasmon resonances can couple with spatial modes and lead to enhanced attenuation[34].

Previous work on 2D PPCs with non-uniform density profiles was conducted by Sakai *et al.*[33] using a FDTD method to compare PPCs with uniform density columns and plasma columns with a J_0 Bessel function density profile. Band diagrams were generated for plasmas with a peak density $n_e = 10^{19}$ m^{-3}, a column space of $a = 2.5$ mm, and a column radius of $d = 1.0$ mm (see Fig. 2.14). Both PPCs have a lattice frequency of $\omega_a/2\pi = c/a = 120$ GHz, a maximum electron plasma frequency of $\omega_{pmax}/2\pi = (e^2 n_e/\varepsilon_0 m_e)^{1/2} = 28.5$ GHz, and a fill fraction of $f = \pi r^2/a^2 = 0.126$. Sakai found that for TE polarization the smooth density profile had a flat-band region (due to plasmon resonances) that was wider than for the discontinuous case. This increase in the flat-band region width was attributed to the density

gradient exposing more plasma densities, and therefore more plasmon resonance frequencies, to interact with the TE wave. Sakai did not see any noticeable difference in the dispersion characteristics at frequencies above ω_{pmax}.

The work in the previous chapter revealed that density gradients have a strong impact on band gap characteristics when the plasma frequency approaches or exceeds the lattice frequency. As the Sakai work only considered a PPC with plasma frequency to lattice frequency ratio of $\omega_{pmax}/\omega_a < 1/4$, impacts of density gradients on band gap behavior would not be expected. This work explores the impact of density gradients for a high plasma frequency to lattice frequency ratios for 2D PPCs.

4.1 The linearized inhomogeneous EM wave equation in an unmagnetized, two-dimensional periodic density modulated plasma

An electromagnetic wave propagating in an unmagnetized, cold, dissipationless, density-varying plasma takes the form of the following inhomogeneous wave equation, as derived in Chap. 3

$$\nabla \times \nabla \times \boldsymbol{E} + \mu_0 \varepsilon_0 \frac{\partial^2 \boldsymbol{E}}{\partial t^2} = \mu_0 \varepsilon_0 \left(\frac{e^2 n(\boldsymbol{r})}{m_e \varepsilon_0} \right) \boldsymbol{E}, \tag{4.1}$$

where $\boldsymbol{E}$ is the electric field, e and m_e are the charge and mass of an electron, and μ_0 and ε_0 are the vacuum permeability and permittivity. The electron number density $n(\boldsymbol{r})$ is assumed an arbitrary, periodic 2D function of space, with periodicity defined by a set of lattice vectors $\boldsymbol{R}$ such that

$$n(\boldsymbol{r} + \boldsymbol{R}) = n(\boldsymbol{r}) \tag{4.2}$$

where $\boldsymbol{R}(\ell) = \ell_1 \boldsymbol{a}_1 + \ell_2 \boldsymbol{a}_2$, $\ell_{1,2}$ are integers, and $\boldsymbol{a}_{1,2}$ are the primitive lattice vectors. This representation differs from similar methods by Kuzmiak[43] and others in that plasma electromagnetic properties are captured through the electron density dependent right hand side, and not through a spatially varying dielectric function. As it is periodic, the density can be

expanded in a infinite Fourier series

$$n(\boldsymbol{R}) = n_0 \sum_{\boldsymbol{G}} \hat{n}_{\boldsymbol{G}} e^{i\boldsymbol{G}\cdot\boldsymbol{R}} \tag{4.3}$$

where n_0 is an average plasma density, $\boldsymbol{G}(h) = h_1\boldsymbol{b}_2 + h_2\boldsymbol{b}_2$ are the reciprocal vectors, and are related to the primary lattice vectors by

$$\boldsymbol{a}_i \cdot \boldsymbol{b}_j = 2\pi\delta_{i,j} \tag{4.4}$$

The coefficients $\hat{n}_G$ can be found by

$$n_0 = \frac{1}{a_c} \iint_C n(\boldsymbol{R}) dC, \tag{4.5}$$

$$\hat{n}_0 = \frac{1}{n_0} \left(\frac{1}{a_c} \iint_C n(\boldsymbol{R}) dC \right) = 1 \tag{4.6}$$

$$\hat{n}_{\boldsymbol{G}\neq 0} = \frac{1}{n_0} \left(\frac{1}{a_c} \iint_C n(\boldsymbol{R}) e^{i\boldsymbol{G}\cdot\boldsymbol{R}} dC \right) \tag{4.7}$$

where C is the surface defined by the primitive unit cell and $a_C = |\boldsymbol{a}_1 \times \boldsymbol{a}_2|$ is its area.

4.1.1 TM polarized plane waves

Transverse magnetic polarization requires that the magnetic field be out of plane of the density modulation, which in this case is chosen to be the xy plane. Therefore the electric field takes on the form of system of plane waves in $\hat{z}$

$$\boldsymbol{E}(\boldsymbol{R}) = \sum_{\boldsymbol{G}} \hat{E}_z(\boldsymbol{k}, \boldsymbol{G}) e^{i(\boldsymbol{k}+\boldsymbol{G})\cdot\boldsymbol{R} - i\omega t} \hat{z} \tag{4.8}$$

where $\boldsymbol{k} = k_x\hat{x} + k_y\hat{y}$ is the 2D wave vector. Substituting the above into the general dispersion relation (Eq 4.1), and Fourier transforming the complete expression, results in the following linearized equation

$$\left(c_0^2|\boldsymbol{k}+\boldsymbol{G}|^2 + \omega^2 - \omega_{p0}^2\right) E(\boldsymbol{G}) - \omega_{p0}^2 \sum_{\boldsymbol{G}'\neq\boldsymbol{G}} \hat{n}(\boldsymbol{G}-\boldsymbol{G}') E_z(\boldsymbol{G}') = 0 \tag{4.9}$$

where $\boldsymbol{G}' \in \boldsymbol{G}$, $\omega_{p0}^2 = \frac{e^2 n_0}{m_e \varepsilon_0}$ is the average electron plasma frequency squared, and $c_0^2 = \mu_0 \varepsilon_0$. The above represents an infinite system of equations for each value of $\boldsymbol{k}$. Note that the first term in Eq. 4.9 is the dispersion relation for EM waves in a uniform plasma, while the second is a series of coupling terms with plane waves offset by $\boldsymbol{G}$ and magnitudes proportional to $\omega_{p0}^2 \hat{n}_\ell$.

4.1.2 TE polarized plane waves

Transverse electric polarization requires that the electric field be out of plane. Therefore the electric field takes on the form of system of plane waves in $\hat{x}$ and $\hat{y}$.

$$\boldsymbol{E}(\boldsymbol{R}) = \sum_{\boldsymbol{G}} \left(\hat{E}_x(\boldsymbol{k}, \boldsymbol{G})\hat{x} + \hat{E}_y(\boldsymbol{k}, \boldsymbol{G})\hat{y} \right) e^{i(\boldsymbol{k}+\boldsymbol{G})\cdot\boldsymbol{R} - i\omega t} \tag{4.10}$$

where $\boldsymbol{k} = k_x\hat{x} + k_y\hat{y}$ is the 2D wave vector as in the TM formulation. Substituting the above into the general dispersion relation (Eq 4.1), and Fourier transforming the complete expression, results in two sets of coupled linearized equations

$$\begin{aligned} \hat{x}: \quad & \left(c_0^2(k_y + h_2)^2 - \omega^2\right)\hat{E}_x(\boldsymbol{G}) + (k_x + h_1)(k_y + h_2)\hat{E}_y(\boldsymbol{G}) + \\ & \omega_{p0}^2 \sum_{\boldsymbol{G}'} \hat{n}(\boldsymbol{G}')\hat{E}_x(\boldsymbol{G} - \boldsymbol{G}') = 0 \end{aligned} \tag{4.11}$$

$$\begin{aligned} \hat{y}: \quad & \left(c_0^2(k_x + h_1)^2 - \omega^2 2\right)\hat{E}_y(\boldsymbol{G}) + (k_x + h_1)(k_y + h_2)\hat{E}_x(\boldsymbol{G}) + \\ & \omega_{p0}^2 \sum_{\boldsymbol{G}'} \hat{n}(\boldsymbol{G}')\hat{E}_y(\boldsymbol{G} - \boldsymbol{G}') = 0 \end{aligned} \tag{4.12}$$

where h_1 and h_2 are the components of the reciprocal lattice vector $\boldsymbol{G}$, the summation is over vectors $\boldsymbol{G}' \in \boldsymbol{G}$, the plasma frequency of the average plasma density is defined as $\omega_{p0} = \sqrt{\frac{e^2 n_0}{m_e \varepsilon_0}}$, and $c_0^2 = \mu_0 \varepsilon_0$ is the vacuum speed of light squared. Like the system for TM plane waves, the above represents an infinite system of equations for each value of $\boldsymbol{k}$. While slightly more complicated, the system is still Hermitian and results in a standard eigenvalue problem as shown in the next section.

The following sections explore the form of these terms for two density profiles: a 2D sine wave modulation on top of a uniform background density, and a rectangular lattice of uniform density plasma rods in vacuum.

4.1.3 Two-dimensional sinusoidally modulated density profile

A two-dimensional sinusoidally modulated plasma (see Fig. 4.1) represents a smooth density profile, similar to what could be created by two perpendicular laser induced Bragg gratings[41]

$$n(\boldsymbol{r}) = n_0 \left(1 + \frac{\chi}{2}\cos(G_1) + \frac{\chi}{2}\cos(G_2)\right) \tag{4.13}$$

where $\chi = (n_{max} - n_0)/n_0$, and n_0 is the average plasma density. The Fourier coefficients found through application of Eqs. (4.5) are

$$\hat{n}_0 = \begin{cases} 1 & \text{for } \boldsymbol{G} = (0,0), \\ \chi/4 & \text{for } \boldsymbol{G} = (\pm 2\pi/a, 0) \text{ and } (0, \pm 2\pi/a). \end{cases} \tag{4.14}$$

All other $\hat{n}_{\boldsymbol{G}}$ values are zero.

4.1.4 Circular plasma columns in vacuum

Uniform density plasma columns in vacuum (see Fig. 4.2, top left) represent the solid state, discontinuous limit, and are indistinguishable from metal cylinders with the same electron density.

$$n(\boldsymbol{r}) = n_{col} H(r_c - |r|) \tag{4.15}$$

where n_{col} is the electron density in the column, $H(x)$ is the Heaviside function, and r_c is the column radius. The average density is $n_0 = \pi r_c^2 n_{col}/a_c$. The Fourier coefficients found through application of Eqs. (4.5) are

$$\hat{n}_0 = \begin{cases} 1 & \text{for } \boldsymbol{G} = (0,0), \\ 2J_1(Gr_c)/Gr_c & \text{for } \boldsymbol{G} \neq (0,0), \end{cases} \tag{4.16}$$

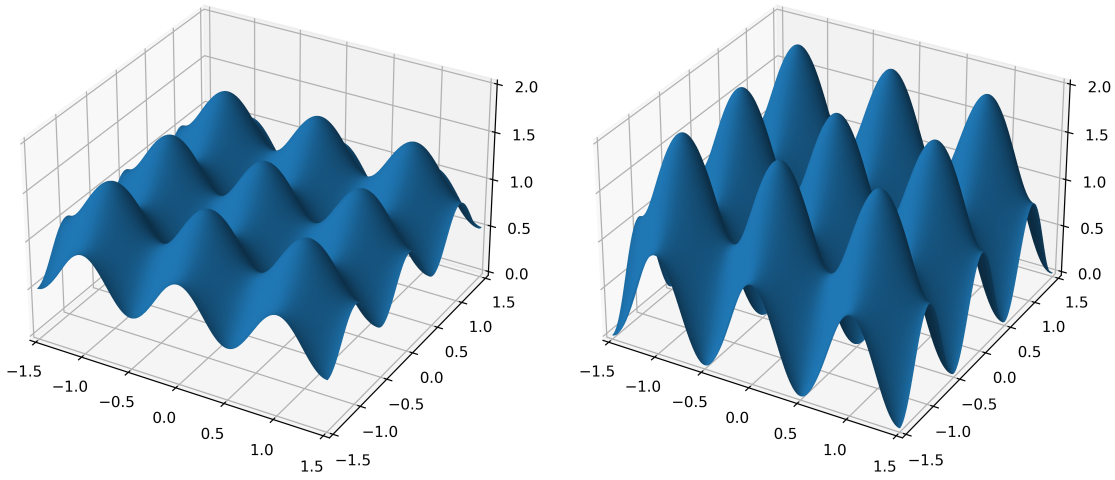

Figure 4.1: A two-dimensional sinusoidally modulated density profile with density normalized such that $\tilde{n}(\boldsymbol{r}) = n(\boldsymbol{r})/n_0$. The modulation amplitudes $\chi = 0.5$ (left) and $\chi = 1$ (right).

where $J_1(x)$ is a Bessel function of the first kind, and $G = |\boldsymbol{G}|$. Fourier representations can be truncated at some number M, where $\boldsymbol{G} = (2\pi\alpha/a, 2\pi\beta/a)$ for integers $\alpha, \beta \in [-M, M]$. When $M = 1$, the Fourier reconstruction is a periodic array of J_0 Bessel functions (see Fig. 4.2, bottom right).

4.2 Method of numerical solution and validation against WARPXM plasma code

To solve the linear coupled systems described in Eqs. (4.9) and (4.11), they are reformulated as eigenvalue problems and solved for each wave number of interest $\boldsymbol{k}$. A subset of cases are compared with solutions found using a cold plasma model solved with an discontinuous Galerkin (DG) finite element method (FEM) on a Bloch-Floquet periodic domain.

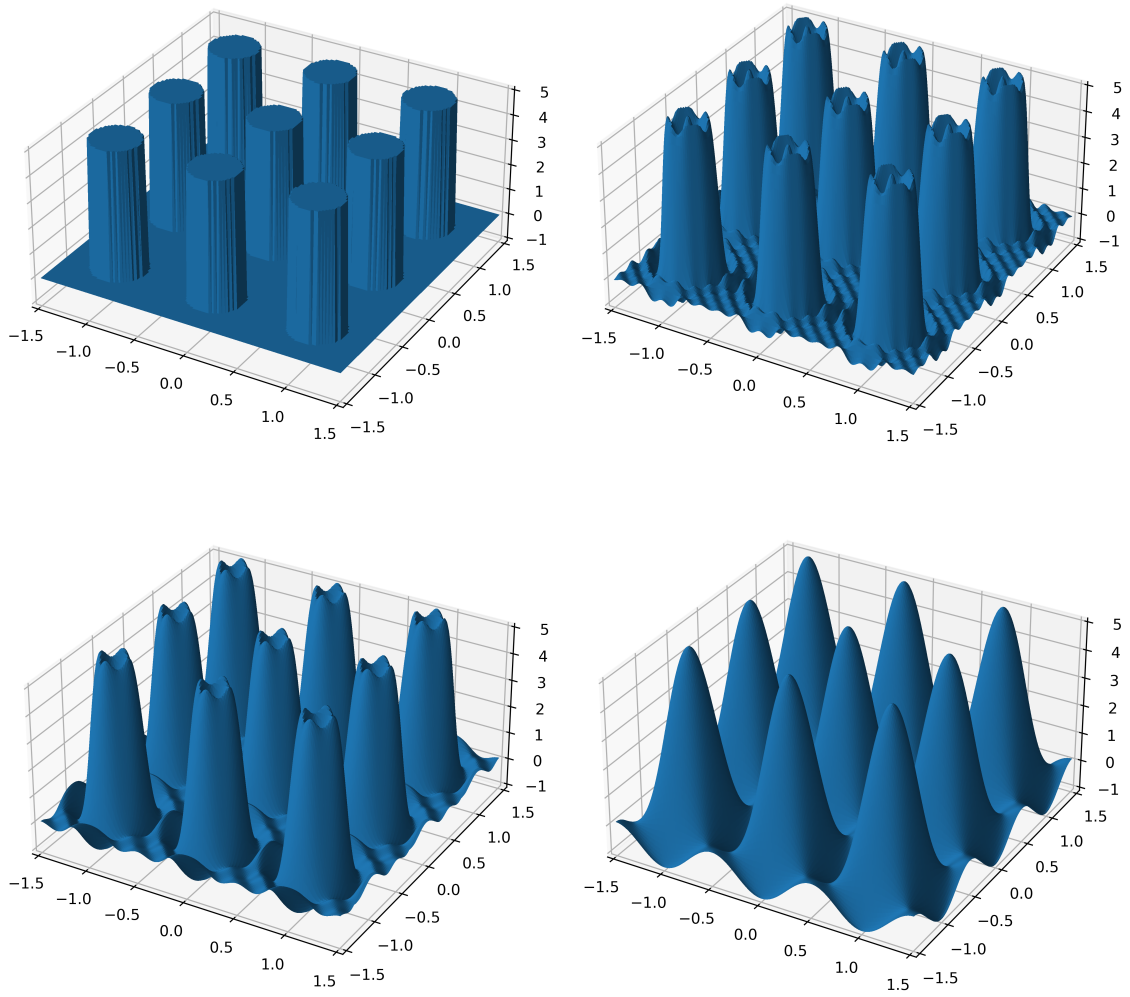

Figure 4.2: A circular column density profile normalized such that $\tilde{n}(\boldsymbol{r}) = n(\boldsymbol{r})/n_0$ (top left) and normalized column radius $r_c/a = 1/4$. Finite Fourier reconstructions of the same profile for $M = 5$ (top right), $M = 3$ (bottom left), and $M = 1$ (bottom right)

4.2.1 Numerical solution of the problem.

In contrast to the one-dimensional problem solved in Ch. 3, the two-dimensional solution requires the assembly of a large block diagonal system where each block has size $(2M+1)\times(2M+1)$ for TM and $(4M+1)\times(4M+1)$ for TE, and $M \leq N$, where $2N+1$ is the number of block diagonals,

$$\boldsymbol{A}(\boldsymbol{k})\boldsymbol{E} = \omega^2 \boldsymbol{E}, \tag{4.17}$$

where for TM, the matrices $\boldsymbol{A}$ and $\boldsymbol{E}$ is defined in index notation as

$$A = \begin{bmatrix} A_M & D_1 & D_N \\ & \cdots & \\ D_{-1} & A_i & D_1 \\ & \cdots & \\ D_{-N} & D_{-1} & A_{-M} \end{bmatrix}, \quad E = \begin{bmatrix} E_M \\ \vdots \\ E_i \\ \vdots \\ E_{-M}. \end{bmatrix} \tag{4.18}$$

Each diagonal block A_i and sub-vector E_i

$$A_i = \begin{bmatrix} a_{j=k=M} & & a_{j=k-1} & & a_{j=k-M} \\ & & \vdots & & \\ a_{j=k+1} & \cdots & a_{jk} & \cdots & a_{j=k-1} \\ & & \vdots & & \\ a_{j=k+M} & & a_{j=k+1} & & a_{j=k=-M} \end{bmatrix}, \quad E_i = \begin{bmatrix} E_{i,j=M} \\ \vdots \\ E_{i,j=0} \\ \vdots \\ E_{i,j=-M} \end{bmatrix} \tag{4.19}$$

where

$$a_{j=k} = (K_x + i)^2 + (K_y + j)^2 + \Omega_{p0}^2 \hat{n}(0,0), \tag{4.20}$$

$$a_{j=k-\beta} = \begin{cases} \Omega_{p0}^2 \hat{n}(\boldsymbol{G}_{0,\beta}) & \text{for} \quad \beta \in [-N, N] \\ 0 & \text{for} \quad \beta \notin [-N, N] \end{cases} \tag{4.21}$$

The off-diagonal blocks D_α are defined as

$$(D_\alpha)_{p=q-\beta} = \begin{cases} \Omega_{p0}^2 \hat{n}(\boldsymbol{G}_{\alpha\beta}) & \text{for} \quad \beta \in [-N, N] \\ 0 & \text{for} \quad \beta \notin [-N, N] \end{cases} \tag{4.22}$$

where $G_{\alpha\beta} = \alpha h_1 \hat{b}_1 + \beta h_2 \hat{b}_2$.

The TE polarization problem is similar, except that each block A_i, D_α, and E_i are composed of sub-blocks

$$A_i = \begin{bmatrix} B^x & C \\ C & B^y \end{bmatrix}_i, \quad D_\alpha = \begin{bmatrix} G & 0 \\ 0 & G \end{bmatrix}, \quad E_i = \begin{bmatrix} E^x_{i,j=N} \\ E^y_{i,j=N} \\ \vdots \\ E^x_{i,j=-N} \\ E^y_{i,j=-N} \end{bmatrix} \tag{4.23}$$

where

$$(B_i^x)_{j=k} = (K_y + j)^2 + \Omega_{p0}^2 \hat{n}(0,0), \tag{4.24}$$

$$(B_i^y)_{j=k} = (K_x + i)^2 + \Omega_{p0}^2 \hat{n}(0,0), \tag{4.25}$$

$$(B_i^x)_{j=k-\beta} = (B_i^y)_{j=k-\beta} = \begin{cases} \Omega_{p0}^2 \hat{n}(\boldsymbol{G}_{0,\beta}) & \text{for} \quad \beta \in [-N, N] \\ 0 & \text{for} \quad \beta \notin [-N, N] \end{cases}. \tag{4.26}$$

Off diagonal sub-blocks C_i and G_α are defined as

$$(C_i)_{j=k} = (K_x + i)^2 (K_y + j)^2, \tag{4.27}$$

$$(G_\alpha)_{p=q-\beta} = \begin{cases} \Omega_{p0}^2 \hat{n}(\boldsymbol{G}_{\alpha\beta}) & \text{for} \quad \beta \in [-N, N] \\ 0 & \text{for} \quad \beta \notin [-N, N] \end{cases}, \quad \alpha \neq 0. \tag{4.28}$$

The systems are solved for each wavevector $\boldsymbol{k}$ of interest. As the wavenumber space is two-dimensional, values of $\boldsymbol{k}$ are chosen along axes of symmetry, which correspond to points along the reciprocal lattice vectors $\boldsymbol{G}$. These slices are traditionally named by the vertices they connect. Vertices for PCs with rectangular symmetry are denoted as Γ, X and M (see Fig. 2.3).

4.2.2 Validation of the analytical model with a plasma model solved using the WARPXM code

To validate the model, the equivalent problem is solved with the WARPXM code, an unstructured Discontinuous Galerkin multi-physics plasma code developed at the University of Washington[63]. For details on problem set up and boundary conditions, see Sec. 5.3.

Simulations are run for the sinusoidally perturbed plasma and the plasma column for both TM and TE polarizations and compared with results for the analytical method in Figs. 4.3 and 4.4, respectively. Agreement is good for all cases, except for the width of the flat-band region in the plasma column with TE polarization. The analytical model predicts that the flat-band region will extend from $\omega = 0$ to the maximum plasma frequency $\omega_{p,max}$, whereas in the simulation the flat-band region is confined to $\omega = 0.5\omega_{p,max} - \omega_{p,max}$.

The flat-bands are due to surface plasma resonances, stationary modes on the surface of the plasma column (see Sec. 2.1.3 and Fig. 2.8). The frequency of these flat bands is a function of plasma frequency and the ratio of plasma column radius to column spacing r_c/a. As was shown by Sakai *et al.*[33], introducing gradients in the plasma density increases the variety of plasmon surface resonances, widening the flat-band region. The analytical model requires the Fourier representation of the density be truncated, therefore the density profile will never be truly discontinuous (see the finite Fourier approximations of plasma columns in Fig. 4.2). Furthermore, low and high density regions are "bumpy", and could give rise to their own plasmon resonances. This indicates a possible limitation to the utility of the analytical model when dealing with discontinuous density profiles.

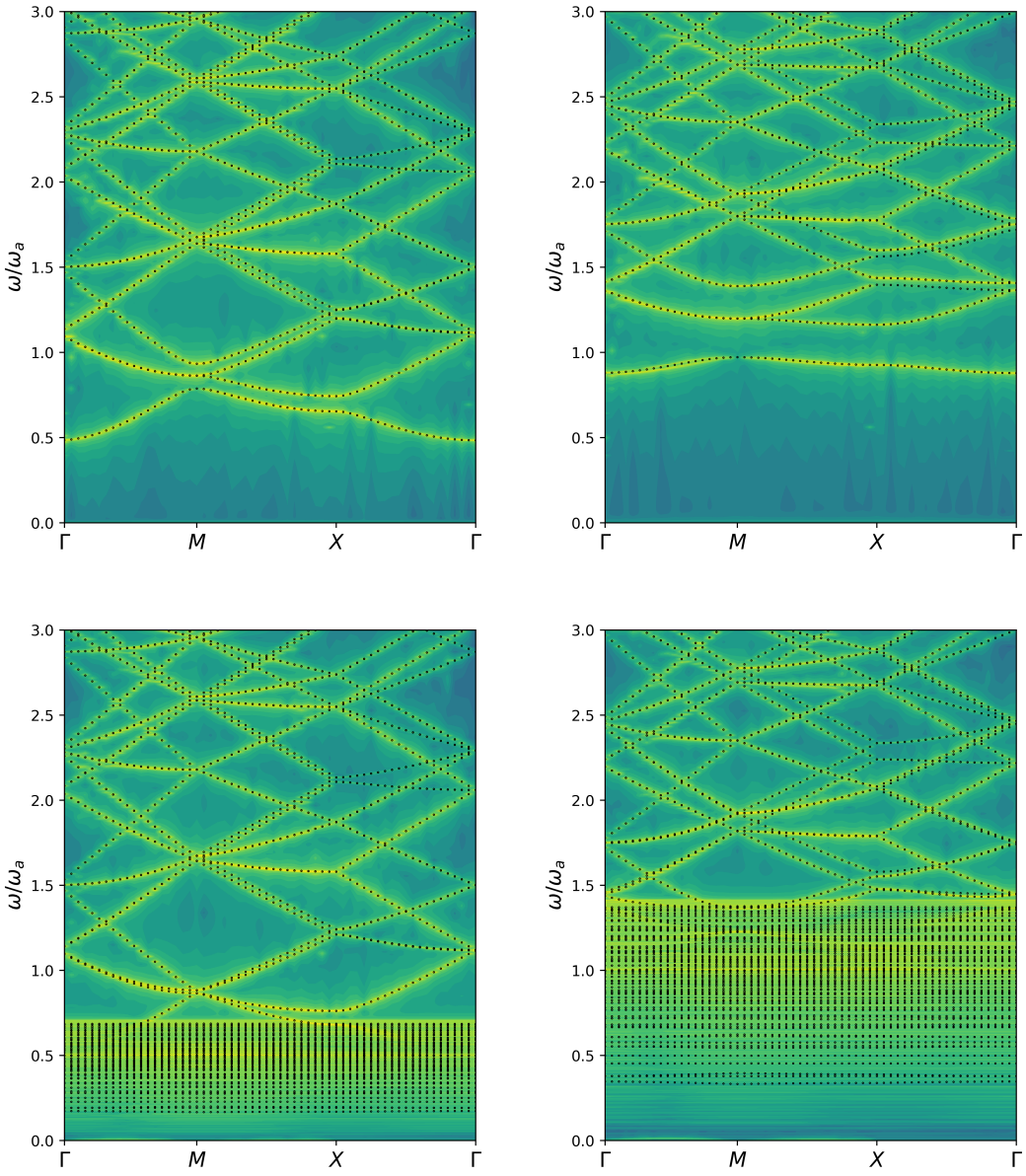

Figure 4.3: Comparison of band diagrams for a 2D sine density profile, generated by solving the plasma system, using WARPXM (color contours indicate magnitude of spectra) and the analytical model described in Sec. 3.1 (dashed lines) with $\chi = (n_{max} - n_{avg})/n_{avg} = 1$ for both TE (top) and TM (bottom) polarization, and $\Omega_{p0} = \omega_{p0}/\omega_a = 0.5$ (left) and $\Omega_{p0} = 1$ (right).

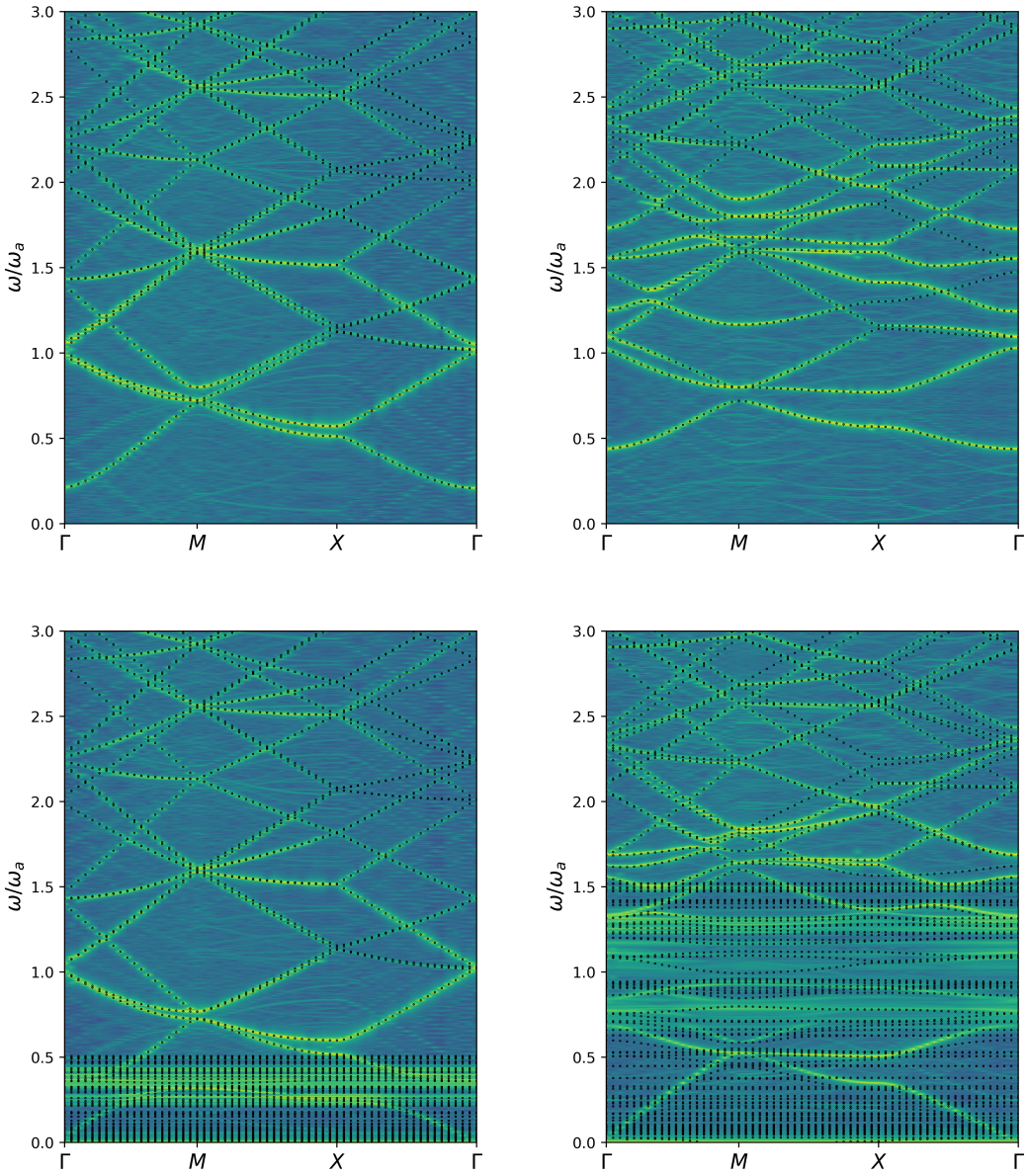

Figure 4.4: Comparison of band diagrams for a plasma column in vacuum, generated by solving the plasma system, using WARPXM (color contours indicate magnitude of spectra) and the analytical model described in Sec. 3.1 (dashed lines) with $r_c/a = 1/4$, for both TE (top) and TM (bottom) polarization, and $\Omega_{p,max} = \omega_{p,max}/\omega_a = 0.5$ (left) and $\Omega_{p,max} = 1.5$ (right). $\Omega_{p0} = 0.22$ and 0.67, respectively. Convergence with the simulation was achieved with a finite Fourier representation of $M = 5$ for the analytical model. The analytical model agrees with the simulation, except in the width of the flat-band band region in TE polarized waves that is an artifact of the finite Fourier representation.

4.3 Impacts of smooth and discontinuous plasma density on dispersion characteristics

The impacts of smooth and discontinuous density profiles on dispersion characteristics are explored though band diagrams generated with the analytical model developed in Sec. 4.1. Each figure overlays the band diagrams of a specific PPC configuration with one variable characteristic (modulation amplitude for the 2D sinusoidally modulated case, or number of density Fourier terms in the plasma column case). Broadening of bands indicates the degree of impact of modulation amplitude or number of Fourier terms on dispersion. Band deflection or curving near band intersections indicates mode coupling and the possible formation of band gaps. When bands maintain a constant trajectory through an intersection, even if broadening is present in one of the intersecting bands, indicates that modes are not being coupled.

In the following sections, the sinusoidally modulated and plasma column density profiles are explored in the presence of TM and TE polarization for a variety of parameters.

4.3.1 TM polarization

An electromagnetic wave in TM polarization will have a magnetic field in the plane of density variation, and an electric field perpendicular to that plane. The electric field causes electrons to oscillate up and down in the infinite dimension, as they would in a homogeneous plasma. As a result, TM wave dispersion in a 2D photonic crystal shares many similarities to dispersion in a 1D PPC: a cutoff region exists below the plasma frequency, and band gaps appear and broaden with increasing modulation amplitude and lattice normalized plasma frequency.

In Fig. 4.5, a sinusoidally modulated plasma with the lattice normalized average plasma frequency $\Omega_{p0} = \omega_{p0}/\omega_a = 0.5$ and 1, is plotted for a range of modulation amplitudes $\chi = (n_{max} - n_{avg})/n_{avg}$. The broadening of bands with increasing modulation amplitude

indicates the separation of modes that are degenerate in a homogeneous plasma. Mode coupling is indicated by the diverging of bands at intersections, and possibly the formation of a band gap. The cut off region is evident below Ω_{p0}, and similar to the 1D sinusoidally modulated PPC, a slow band migrates into the cut off region with increasing modulation amplitude and Ω_{p0}.

Unlike in the 1D sinusoidally modulated case, some bands remain relatively unaffected by modulation amplitude, while others at the same frequency change dramatically. Also, mode coupling does not occur at all intersections of similar frequency. This is likely due to the symmetry of the density perturbation in relation to the symmetry of the spatial mode associated with the band. In the 2D sinusoidally modulated case, density Fourier modes only exist in two directions. In the plasma column case (see Fig. 4.6) density Fourier modes exist in more directions (though some with more amplitude than others due to the symmetry of the crystal), and mode coupling occurs at more intersections.

The band diagrams in Fig. 4.6 are for the plasma column in vacuum density profile with finite Fourier representations of $M = 1$, a J_0 Bessel function, and $M = 5$, which is considered a fully converged approximation for the discontinuous profile for the frequency range of interest. Bands with different solutions for the $M = 1$ and 5 finite Fourier approximations are bands that are sensitive to the presence of discontinuities. The plasma frequency of the average density Ω_{p0} is the same as for the sinusoidally modulated cases, but the maximum plasma frequency is higher: $\Omega_{p,max} = \omega_{p,max}/\omega_a = 1.1$ and 2.2, compared to 0.7 and 1.4, respectively.

The primary difference between the sinusoidally modulated and the plasma column cases is the complexity of the bands. More band intersections display signs of coupling, and more degenerate bands are separated. The complexity increases with increasing discontinuity and with plasma frequency Ω_{p0}. This is in agreement with the differences between 1D smooth and discontinuous density profiles.

An additional difference predicted by the 1D PPC study is that the cut off region is much smaller for the plasma column case, and remains relatively constant despite increasing plasma density. The shape of the low density region in the discontinuous cases is constant in shape and density, whereas the smooth profiles have low density regions that steepen with increasing plasma density, changing the frequency of allowed modes.

TM polarization in a 2D PPC shares much in common, both physically and dispersion-wise, with the 1D PPC, albeit more complex. Next, the same density profiles are examined for TE polarized EM waves.

4.3.2 TE polarization

Electromagnetic waves that are TE polarized have electric fields transverse to the plane of density variation, and a magnetic field orthogonal to that plane. Where TM electric fields accelerated electrons in the homogeneous dimension, TE electric fields accelerate electrons against spatial density gradients. Electrons deform away from background ion density profiles, electric fields are generated, and surface plasmons are excited. As discussed in Sec. 2.1.3, the frequency of these modes is a function of the plasma frequency and the plasma radius to lattice constant ratio, and mode number. Since the different mode numbers will have slightly different resonant frequencies, the surface plasmons appear in the band diagrams as a band of flat-bands. The greater the spread of radii and plasmas frequencies, the wider the flat-band region.

The analytical model in this work uses a finite Fourier representation of the plasma density. As the Fourier representation is finite, there will always be finite density gradients, especially in the vicinity of discontinuities. This leads the model to over-predict the width and density of flat-band regions, as discussed in the validation section. Despite this limitation when it comes to truly discontinuous density profiles in TE polarized EM waves, for smooth density profiles like those found in plasmas, the model agrees very well with simulation (see

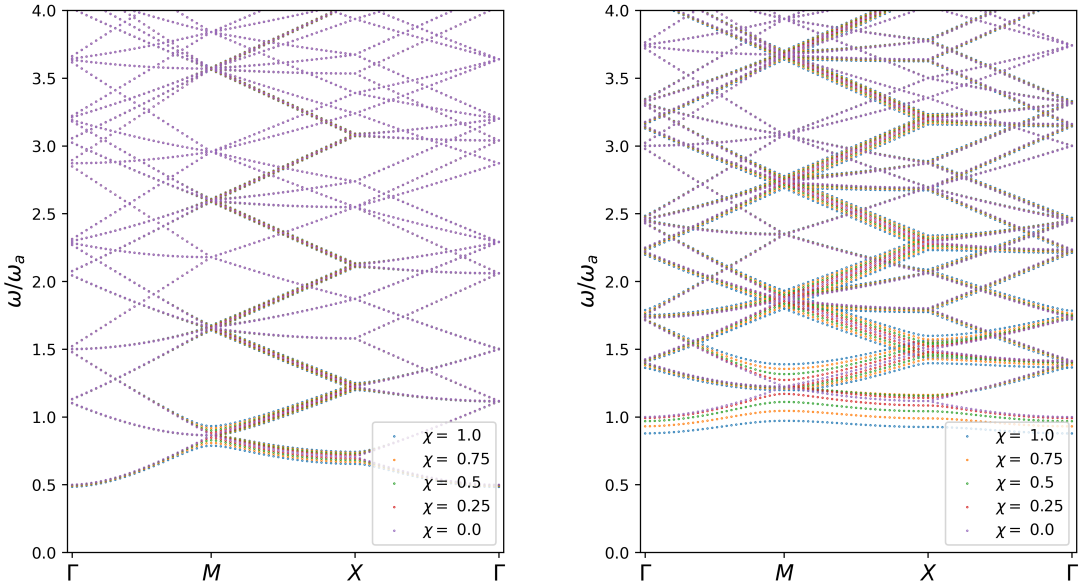

Figure 4.5: Comparison of band diagrams for a 2D sine density profile the analytical model described in Sec. 3.1 with TM polarization and a range of modulation amplitudes $\chi = (n_{max} - n_{avg})/n_{avg}$ for $\Omega_{p0} = \omega_{p0}/\omega_a = 0.5$ (left) and $\Omega_{p0} = 1$ (right). Broadening of bands indicates the impact of modulation amplitude on dispersion. Band deflection at intersections indicates mode coupling.

Fig. 4.3).

In Fig. 4.7, the band diagrams for a 2D sinusoidally modulated plasma with varying modulation amplitude are compared for TE polarized EM waves. The expected flat bands are present from a low frequency up to $\Omega_{p,max} = 0.7$ and 1.4, for the $\Omega_{p0} = 0.5$ and 1 cases, respectively. There are no allowable propagation modes below the flat-band region, which is consistent with the simulation, and with the fact that all low density regions are isolated, and not continuously connected, leading to density wells and trapped modes.

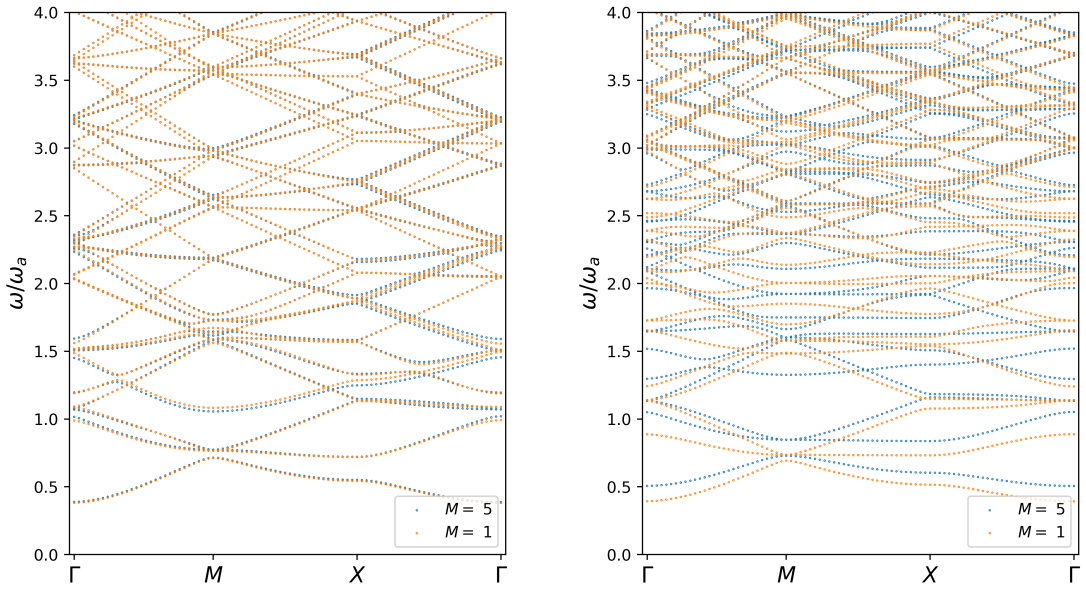

Figure 4.6: Comparison of band diagrams for a plasma column in vacuum calculated with the analytical model described in Sec. 3.1 for TM polarization and finite Fourier representations $M = 1$, a J_0 Bessel function, and $M = 5$, which is considered a fully converged approximation for the discontinuous profile for the frequency range of interest. A low density, with lattice averaged plasma frequency $\Omega_{p0} = 0.5$ (left) and high density $\Omega_{p0} = 1$ (right), with $\Omega_{p,max} = \omega_{p,max}/\omega_a = 1.1$ and 2.2, respectively. Bands with divergent solutions for the $M = 1$ and 5 finite Fourier approximations are bands that are sensitive to the presence of discontinuities.

The band diagrams for plasma column in vacuum in Fig. 4.8 demonstrate the overabundance of predicted flat bands. As the peak plasma density is higher, the flat band region now extends even beyond the maximum plasma frequencies $\Omega_{p,max} = 1.1$ and 2.2 (for the $\Omega_{p0} = 0.5$ and 1 cases, respectively) due to Gibbs phenomenon creating density overshoots around discontinuities. Bands with non-zero group velocities can be faintly seen through the

flat bands at low frequencies, and it is known from experiment and simulation that there is no cutoff region.

The potential impacts of TE flat-bands and surface plasmons on real PPC devices will be discussed in the next section.

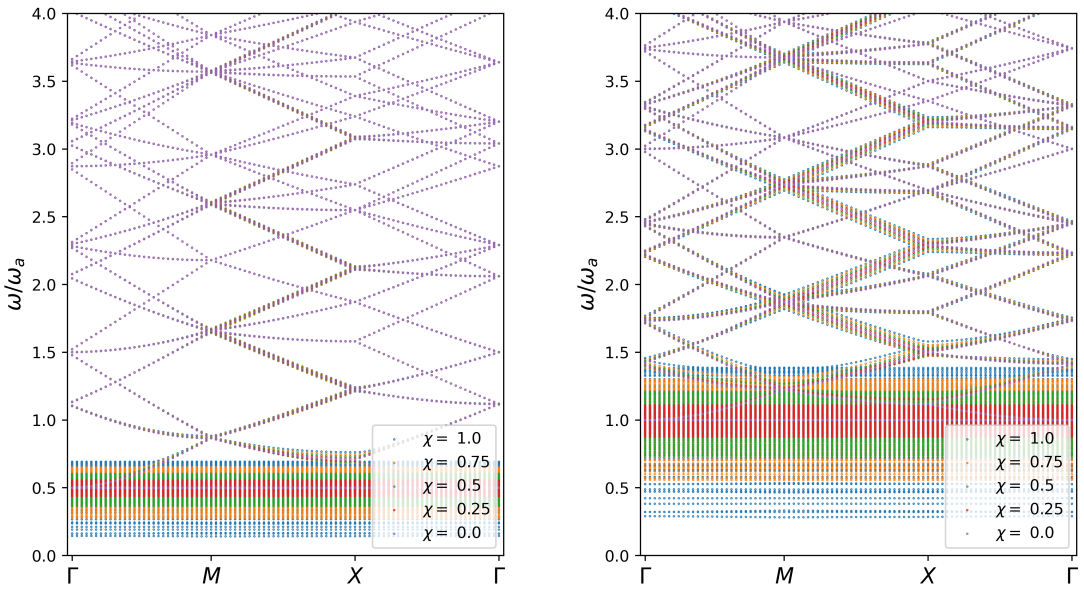

Figure 4.7: Comparison of band diagrams for a 2D sine density profile the analytical model described in Sec. 3.1 with TE polarization and a range of modulation amplitudes $\chi = (n_{max} - n_{avg})/n_{avg}$ for $\Omega_{p0} = \omega_{p0}/\omega_a = 0.5$ (left) and $\Omega_{p0} = 1$ (right). Broadening of bands indicates the impact of modulation amplitude on dispersion. Band deflection at intersections indicates mode coupling. The flat-band region broadens with diverging minimum and maximum plasma densities.

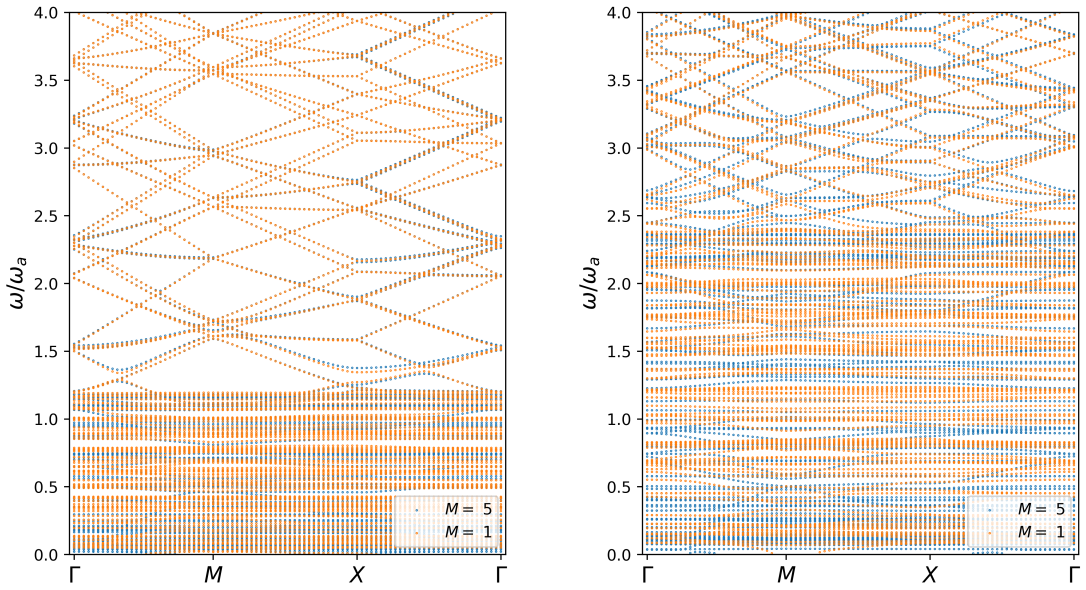

Figure 4.8: Comparison of band diagrams for a plasma column in vacuum calculated with the analytical model described in Sec. 3.1 for TE polarization and finite Fourier representations $M = 1$, a J_0 Bessel function, and $M = 5$, which is considered a fully converged approximation for the discontinuous profile for the frequency range of interest. A low density, with lattice averaged plasma frequency $\Omega_{p0} = 0.5$ (left) and high density $\Omega_{p0} = 1$ (right), with $\Omega_{p,max} = \omega_{p,max}/\omega_a = 1.1$ and 2.2, respectively. Bands with different solutions for the $M = 1$ and 5 finite Fourier approximations are bands that are sensitive to the presence of discontinuities.

4.4 Implications of density profile shape on 2D plasma photonic crystals

The intention of this study is to elucidate the impacts of smooth density gradients in two-dimensional plasma photonic crystals as compared to their discontinuous solid-state counter parts. A two-dimensional sinusoidal plasma modulation serves as both an analog to the one-

dimensional sinusoidally modulated plasma, but also represents potential devices formed through perpendicular laser Bragg gratings. In TM polarized waves, the dispersion behaves very much like the 1D case. In TE polarized waves, the presence of flat-bands due electric fields transverse to density gradients adds an extra layer of complexity. Flat-bands due to surface plasmons create stop-band regions at all frequencies below the maximum plasma frequency, as compared TM polarization where the cutoff region extends to the average plasma frequency only.

Plasma columns in vacuum are analogous to metal rods in vacuum. Finite Fourier representations of the plasma columns approximate density profiles of plasmas in many experimental PPC devices. In agreement with previous work by Sakai *et al.*, PPCs with a small lattice normalized average plasma frequency, $\Omega_{p0} \lesssim 0.5$, the absence or presence of discontinuities has only slight impacts on dispersion characteristics of plasma column style dispersion relations. But when the lattice normalized plasma frequency is large $\Omega_{p0} \gtrsim 0.5$, the importance of discontinuities becomes significant, and leads to mode coupling and band gaps at higher band intersections than a smooth density profile. This was predicted by the work in the previous chapter in 1D smooth and discontinuous PPCs, and evidently holds true in higher dimensions. Future work will involve assembling band gap maps to study the specific characteristics of complete and partial band gaps as a function of gradients.

Ultimately, flat-bands in TE polarized waves are the biggest difference between 1D and 2D PPCs. Gradients have a large impact on the width of the flat-band region. If a low frequency TE pass band is desired, dielectric barriers are necessary to avoid gradients at low density. It may also be possible to introduce gradients intentionally in order to overlay a photonic band gap with flat bands to create a Fano-like resonance, as described by Righetti *et al.*[34].

In an experiment by Wang *et al.*[37], a two-dimensional plasma photonic crystal formed from a rectangular array of plasma filled quartz discharge tubes, the measured transmission

spectra for TE polarized GHz waves proved to be far more complex than a simulated spectra by a HFSS model assuming uniform plasma density, especially in cases where the assumed average plasma frequency approached the lattice frequency (see Fig. 5.5). The broadening of the band gap region associated with surface plasmon resonances as compared to the simulation is a likely indicator of the presence of density gradients, while the smaller but still significant band gaps at higher frequencies suggests that discontinuities in density due to the quartz tube are also important. In summary, the combination of finite density gradients and discontinuities can lead to complex transmission spectra not well approximated by only smooth, or only discontinuous, models.

4.5 Conclusion

PPCs have a smoothly varying density structure as compared to solid state PCs which have discontinuous changes in material properties. In Chaps. 3 and 4, smooth and discontinuous density profiles in one and two dimensions were explored with a linear dispersion model. Band diagrams and group velocity band gap maps were used to develop a systematic understanding of the impact of density gradients on dispersion, and ultimately transmission, characteristics.

The primary conclusion resulting from the investigation is that density profile shape has a significant impact on transmission characteristics when the plasma frequency is comparable to the lattice frequency of the crystal. More specifically, each Fourier mode of the density profile can be related directly to a specific band gap. Density Fourier content can be modified through the introduction of discontinuities in the form of dielectric lattices or barriers to access higher band gaps, extending the operational frequency range of a device well beyond its lattice frequency. This is particularly useful in accessing THz frequencies that would otherwise require micron scale lattices.

In the specific context of two-dimensional PPCs, gradients expand flat-band regions in TE polarized waves. Discontinuities broaden traditional photonic band gaps at higher fre-

quencies. Both gradients and discontinuities can exist simultaneously to create complex transmission spectra not well represented by models that assume only smooth or discontinuous profiles. In the pursuit of THz PPC devices that push the boundaries of current PPC sizes and densities, a thorough understanding of the interplay of these effects is crucial. With a sophisticated understanding of these effects, density profile shape can become yet another knob in the already rich space of PPC design parameters.

In the next chapter, the impact of other non-ideal and non-linear aspects of PPCs are explored with a finite two-dimensional plasma simulation code.

Chapter 5

FULLY IONIZED PPC RESPONSE TO HIGH POWER MICROWAVES

Most existing PPC modeling efforts use methods adapted from, or directly intended for, metal PCs. These models use a Drude model picture of electron transport and assume uniform and static material properties. Plasma models allow for intrinsic dynamics, such as plasma heating and plasma deformation in response to strong fields. Once validated, these plasma models can push into regimes hard to access with current experiments. Plasma fluid models can also approximate some of the complexities of physical embodiments, like finite size, or diagnostic configurations, versus ideal analytical or theoretical models that look at the ideal case. Furthermore, models can explore real time plasma and field dynamics allowing for a greater intuitive understanding of plasma-field interactions.

In this section, a high fidelity two-fluid (electron-ion) 5-moment plasma model is solved with the discontinuous Galerkin (DG) finite element method on unstructured grids to analyze the response of a fully ionized two-dimensional plasma-vacuum photonic crystal. Simulation results are compared to those of standard PC software (ANSYS HFSS) and to experimental results from a GHz plasma photonic crystal and the effects of changes in PPC configuration are explored. Finally, a THz laser plasma photonic crystal is explored numerically for non-ideal and non-linear effects including: finite PPC size, finite temperature, density gradients, and the presence of strong electric fields.

5.1 Two-fluid, 5-moment plasma model

A two-fluid (ions and electrons) 5-moment plasma model[63] is chosen for this work due to its versatility. As the system is written below it can capture electromagnetic waves and their self consistent interaction with charged fluid species, ion dynamics, a finite electron mass, as well as finite temperature effects. With relatively little difficulty, inter- and intra-species collisions, diffusion, and reactions can also be included (see Chap. 6). Small deviations from Maxwellian and non-isotropic pressures can be included through Braginskii type closure terms[69]. Large deviations from Maxwellian particle distributions cannot be captured, therefore applicability is limited to plasmas with Knudsen numbers much less one ($\mathrm{Kn} = \lambda_{mfp}/L \ll 1$).

Additionally, terms can be dropped in order to approximate more simple models, as was done in Chaps. 3 and 4 in order to validate an analytical model based on the Drude model of electron transport. The following conservative, normalized form of 5-moment equations is used for the work in this chapter. In certain cases in this chapter some terms are dropped, but are made clear in the text.

The 5-moment model evolves each species α (ions and electrons) through the conservation of mass density

$$\frac{\partial \rho_\alpha}{\partial t} + \nabla \cdot \boldsymbol{p}_\alpha = 0, \tag{5.1}$$

momentum density

$$\frac{\partial \boldsymbol{p}_\alpha}{\partial t} + \nabla \cdot \left(\frac{\boldsymbol{p}_\alpha \otimes \boldsymbol{p}_\alpha}{\rho_\alpha} + P_\alpha \overleftrightarrow{\boldsymbol{I}} \right) = \left(\frac{L}{\delta_p} \right) \left(\frac{Z_\alpha}{A_\alpha} \right) (\rho_\alpha \boldsymbol{E} + \boldsymbol{p}_\alpha \times \boldsymbol{B}),$$

and energy density

$$\frac{\partial \varepsilon_\alpha}{\partial t} + \nabla \cdot \left((\varepsilon_\alpha + P_\alpha) \frac{\boldsymbol{p}_\alpha}{\rho_\alpha} \right) = \left(\frac{L}{\delta_p} \right) \left(\frac{Z_\alpha}{A_\alpha} \right) \boldsymbol{p}_\alpha \cdot \boldsymbol{E}, \tag{5.2}$$

coupled with Maxwell's equations

$$\frac{\partial \boldsymbol{E}}{\partial t} = (\omega_p \tau)^2 \left[\left(\frac{\delta_p}{L} \right)^2 \nabla \times \boldsymbol{B} + \left(\frac{\delta_p}{L} \right) \boldsymbol{j} \right], \tag{5.3}$$

$$\frac{\partial \boldsymbol{B}}{\partial t} = -\nabla \times \boldsymbol{E}, \tag{5.4}$$

where ρ, $\boldsymbol{p}$, $\boldsymbol{E}$, $\boldsymbol{B}$, and t are normalized by reference values $m_p n_0$, $p_0 = m_p n_0 c_0$, $E_0 = c_0 B_0$, $B_0 = (\mu_0 m_p n_0 c_0^2)^{1/2}$, and $\tau = L/c_0$, respectively. The energy density is a sum of both internal and kinetic energy

$$\varepsilon_\alpha = \frac{1}{\gamma_\alpha - 1} P_\alpha + \frac{1}{2\rho_\alpha} \boldsymbol{p}_\alpha^2 \tag{5.5}$$

where γ_α is the ratio of specific heats, P_α is the isotropic pressure, and total current $\boldsymbol{j}$ is defined as

$$\boldsymbol{j} = \sum_\alpha \frac{Z_\alpha}{A_\alpha} \boldsymbol{p}_\alpha. \tag{5.6}$$

The reference density, n_0, is chosen based on typical density values, L is the problem length scale, m_p is the proton mass, and c_0 is the vacuum speed of light. The nondimentional parameters are: δ_p/L, the normalized proton skin depth, $A_\alpha = m_\alpha/m_p$, the proton normalized particle mass, and $\omega_p \tau$, the normalized proton plasma frequency.

5.2 WARPXM computational framework

The above 5-moment model is solved in WARPXM, an unstructured discontinuous Galerkin (UDG) multi-physics plasma code developed at the University of Washington[63]. The code is a collaborative effort, built off of the work of many current and former students. The 5-moment model, Maxwell's equations, as well as spatial and temporal integrators had all been implemented and expanded by others[14, 63, 70, 71, 72, 73, 74, 75] prior to this work.

The WARPXM framework is a powerful tool for looking at non-linear effects in plasma photonic crystals for several reasons. Modular implementation of arbitrary hyperbolic and parabolic equations allows for flexible physics. The unstructured mesh permits modeling complex geometries. Furthermore, the domain can be decomposed in subdomains where different equation sets (and therefore different physics) can be evolved. An inherent feature of the UDG method is that it is highly parallelizable, allowing the code to take advantage

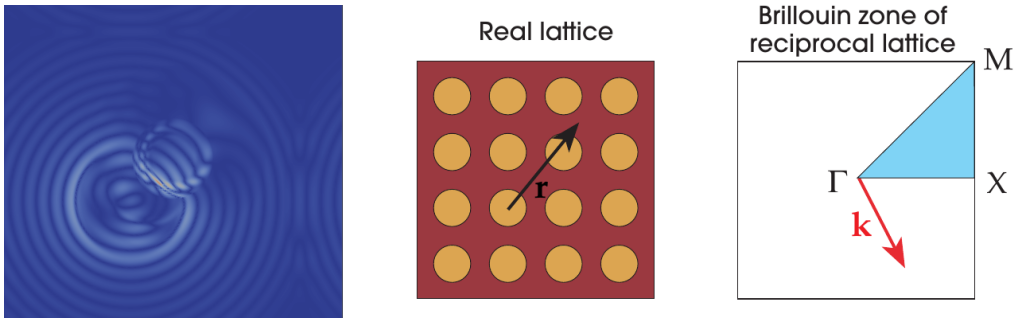

Figure 5.1: (Left) Example unit cell crystal domain shortly after initialization. Contours are real electric field magnitude. (Right) The Brillouin Zone (smallest unit of symmetry) for a rectangular crystal lattice, with lines of symmetry and symmetry points used for determining important **k** wave vectors[21].

of high performance computing resource.

Finally, the modularity of the code allows for the implementation of advanced boundary conditions. In this work, both virtual (BCs between subdomains) and real (BCs at domain boundaries) are implemented and used. See Appxs. A and B for further details.

5.3 Infinite crystal

The infinite crystal is useful as it can provide information about propagation bands and band gaps. For this model, a two-dimensional mesh of a single crystal unit cell is used. Bloch periodic boundary conditions (see Appx. A) are imposed on all boundaries. A plasma, or other material model, is initialized and evolved in the center subdomain. A complex field is evolved everywhere through two sets of Maxwell field equations (real and imaginary). The plasma and field are coupled through source terms.

A radial sinc function is initialized in the real field in order to excite a broad range of wave numbers in all directions. A series of simulations are run, each having a different **k**

vector applied on the Bloch boundary conditions that corresponds to reciprocal points on crystal lines of symmetry. The region defined by this region on the reciprocal lattice is the Brillouin Zone.

The simulation is run long enough to allow for the emergence of constructively interfering modes. A Fourier analysis is performed on data collected at specific points in space to determine the frequency of these modes. Modes are then plotted per $\mathbf{k}$ to construct a band diagram. A single unit cell (see Fig. 5.1), with Bloch-Floquet boundary conditions, is used to simulate the infinite plasma

$$\mathbf{E}^L(\mathbf{x}) = \mathbf{E}^R(\mathbf{x})e^{j\psi}, \quad \mathbf{E}^R(\mathbf{x}) = \mathbf{E}^L(\mathbf{x})e^{-j\psi}, \quad \text{where} \quad \psi = \mathbf{k}\cdot\mathbf{a}. \tag{5.7}$$

See Appendix A for a detailed description of the boundary condition implementation. The Bloch periodic boundary conditions are used in the simulations presented in Chaps. 3 and 4.

5.4 2D GHz plasma photonic crystal

As THz PPCs are still difficult to manufacture, a GHz PPC is chosen as a bench mark case for the numerical model. The experiment chosen is a regular array of plasma discharge tubes by Wang and Cappelli[37] at Stanford. The discharge tube array is chosen due to its geometric simplicity, the existence of quality experimental transmission spectra, and previous comparison to a simulation from ANSYS. The WARPXM simulation results are benchmarked against the experimental results, and then expanded to explore a wider range of radiation frequencies, as well as a variety of plasma column arrangements.

5.4.1 Experimental GHz PPC parameters

The two-dimensional PPC experiment consists of a 7x7 array of plasma discharge tubes[37, 76] (see Fig. 5.2). The discharge tubes contain an argon gas seeded with mercury. The quartz tubes have a lattice spacing of $a = 38.1mm$, and an inner radius of $r = 6.5$ mm, which results

in a lattice frequency of $f_a = c_0/a = 7.9$ GHz. Variable amperage applied to the plasma discharge tubes is the primary control of plasma parameters. Three amperages are chosen that correspond with an estimated plasma density of $n_e = 1.1,\ 5.8$, and 7.8×10^{17} m^{-3} ($f_{pe} = 3.0,\ ,6.9$, and 8.0 GHz, with plasma frequency to lattice frequency ratio $f_{pe}/(c_0/a) = 0.4-1.0$.). The measured spectra published in Ref. [76] are compared with HFSS simulations of a semi-infinite seven row crystal, with a 1 mm quartz envelope ($\epsilon = 3.8$) and uniform density plasma with $r = 4.6$ mm. Collision frequency is assumed to be $\nu = 1.0$ GHz for the HFSS ANSYS simulation.

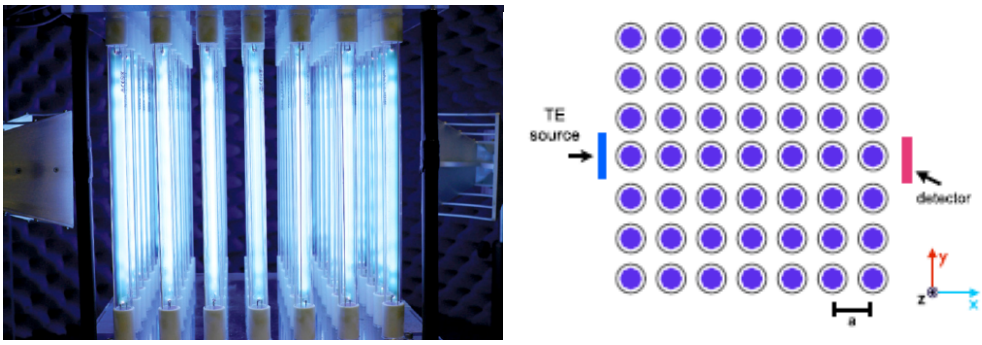

Figure 5.2: Stanford plasma photonic crystal experimental setup[37]. Quartz discharge tubes contain an argon gas seeded with mercury. Lattice spacing $a = 38.1$ mm, $r = 7.5$ mm.

5.4.2 WARPXM simulation parameters

The simulated domain consists of an array of regular, fully ionized, hydrogen plasma filled columns in a vacuum, with a uniform plasma density (see Fig. 5.3). A microwave source is initialized on the left side of the domain with a sinc function plane wave (the Fourier transform of band limited rectangular function) with a frequency range of 1–75 GHz. The electric and magnetic fields are sampled at probe locations to the right of the PPC region. The plasma is evolved using the two-fluid (ion and electron) 5-moment model coupled with

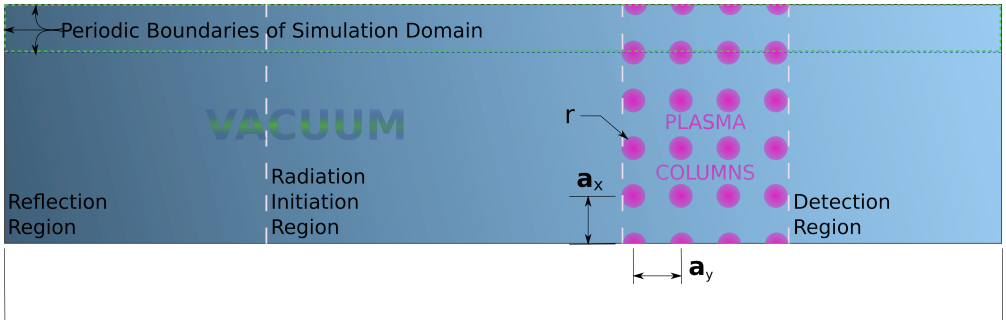

Figure 5.3: The WARPXM simulation domain consists of a reflection region (left), an EM wave initialization region where a sinc waveform is initialized with a right facing Poynting vector (center left), a plasma column region (center right), and a detection region where the EM fields are sampled at several locations (right). The domain is periodic in both x and y, and is made sufficiently to prevent EM waves transiting the periodic boundary in either direction and effecting the detection region. Maxwell's equations are evolved everywhere (Eqs. (5.3) and (5.4)), and the complete two-fluid plasma model (Eqs. (5.1)-(5.2)) are solved in the plasma columns only.

full Maxwell equations, implemented on a 2D, unstructured mesh. The density profile in columns is uniform to match the ANSYS HFSS simulation, with the same lattice constant and plasma column radius. Unlike the HFSS simulation, the quartz envelope is not included and collisional effects are not modeled.

5.4.3 Comparison of WARPXM with experimental transmission spectra

Transmission spectra are calculated for the WARPXM simulations and overlayed on transmission spectra found experimentally and with ANSYS HFSS in Fig. 5.5. The experimental spectra tend to be broader, and shallower. The impact non-uniform density profiles was already examined in Chaps. 3 and 4, and found that density gradients broaden both photonic

Figure 5.4: The simulation domain described in Fig. 5.3 overlayed with contours of E_y for four simulation times: in descending order, $t = 0,\ 0.5,\ 1$, and 1.5 ns. Locations of plasma columns are indicated in pink. The sinc waveform interacts with the plasma array causing certain wave lengths to be reflected, while most pass through unaffected.

bands and plasmon resonance related bands in TE mode EM waves. The effect of finite arrays, and the impact of non-uniform density profiles on transmission spectra specifically (not captured by either simulation) on band gap width and depth are discussed in the following sections. The HFSS spectra (dashed lines) show a narrow band gap at 9 GHz that do not appear in either the experimental or WARPXM spectra, and is likely due to the quartz envelope. A narrow, sharp feature occurs at $\sim$ 3, 6, and 9 GHz in the HFSS spectra which does not seem to be heavily dependent on plasma density and is likely due to bands associated with the quartz envelope. As there is possible reflection of some of the narrow bands in the experimental data, but none in the WARPXM spectra, these bands are likely due to photonic band gaps associated with the quartz tubes. A WARPXM simulation with the quartz tube and non-uniform profile would be necessary to determine if this is the case.

In other ways, the WARPXM results show good agreement with experiment. Locations of all major features in the experimental results are reflected in the WARPXM spectra, especially at higher frequencies, where they are not all captured with HFSS. With a baseline

validation of and understanding of the transmission spectra provided by the 2D WARPXM simulations, several numerical studies of plasma densities and configurations not covered by the experiment are taken in the following sections.

5.4.4 Plasma frequency dependence of transmission characteristics

Control of electron plasma frequency (f_{pe}) is the primary real-time tunable parameter for the control of transmission in a plasma based photonic crystal. As can be seen from the experimental spectra in Fig. 5.5 (as well as supported by the gap map analysis in Chaps. 3 and 4) the band gaps are more complex as the plasma frequency approaches, and exceeds the lattice frequency f_a. The GHz PPC experiment did not explore plasma frequencies any greater than $f_{pe} = f_a$. In this section, the plasma frequency is varied to $> 4f_a$ in order to elucidate the impact of large plasma frequencies on transmission spectra. In Fig. 5.6 simulations using a four row semi-infinite crystal with plasma radius and spacing the same as the experimental configuration (configuration A in Fig. 5.8) are run to generate transmission spectra for plasma frequencies ranging from 10-25 GHz ($f_{pe} = 1.1f_a - 2.5f_a$).

With increasing plasma frequency, the dominant band gaps also increase in frequency and width, as expected from the band diagram analysis in Chap. 4. The depth of band gaps is not as easy to infer from dispersion information of infinite crystals. Examining the band diagrams in Fig. 4.4 for uniform plasma columns, the flat band region due to surface plasmon resonances covers a wide band between $f = 0.5f_{pe} - f_{pe}$. The transmission spectra reflect this fact with broad band gaps occurring in the same regions for a given plasma frequency. The photonic band gaps (forbidden regions) for wave vectors in the $\gamma - X$ orientation (far right on the dispersion relations in Fig. 4.4) appear at certain band intersections both above and below the flat band region. In the transmission spectra, this is reflected in the narrow band gaps with relatively constant frequencies (see gap at ~ 7 GHz). What cannot be seen in the band diagram is the photonic bands obscured within the flat band region. These

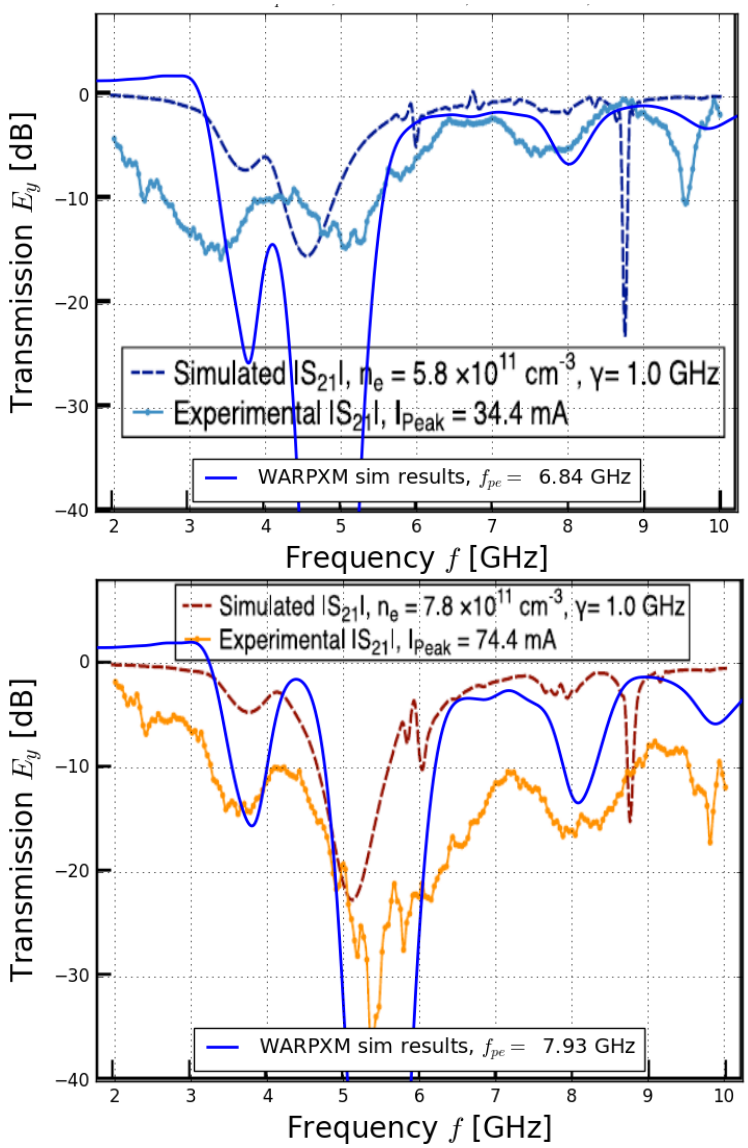

Figure 5.5: Transmission spectra of E_y for TE microwaves from the experiment (solid thick lines), ANSYS HFSS Drude model simulation (dashed), and WARPXM semi-infinite 5-moment fluid model (solid dark blue). In both simulations, plasma density is assumed to be uniform within the tube. Electron density is $n_e = 5.8 \times 10^{17}$ and $7.8 \times 10^{17}\mathrm{m}^{-3}$ respectively.

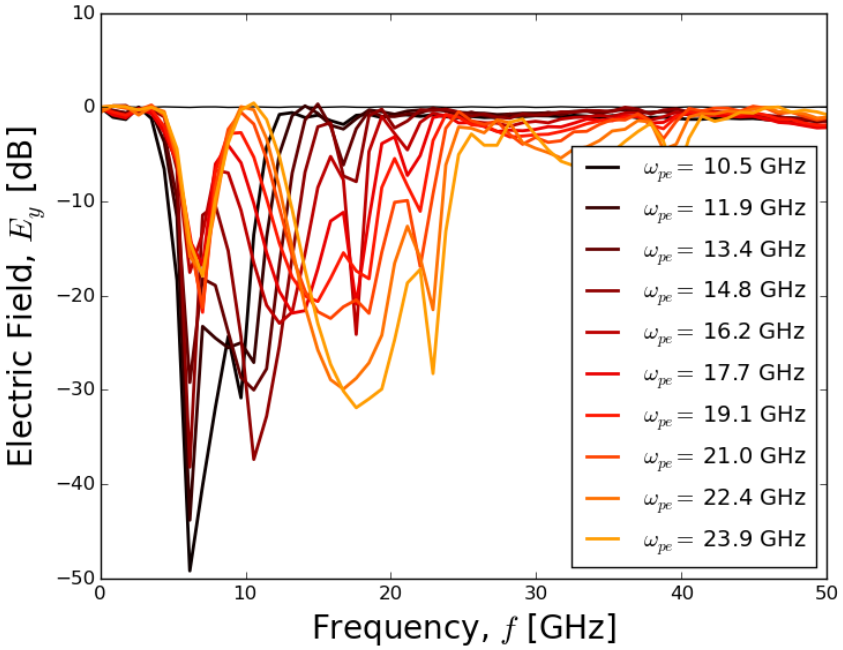

Figure 5.6: Transmission spectra in E_y for TE polarized fields with f_{pe}=10.5-23.9 GHz. With increasing plasma frequency, the dominant band gaps also increase in frequency and width, as expected from the band gap map analysis.

obscured photonic band gaps appear as troughs within the flat band attenuation bands, adding complexity. This complexity only increases with plasma frequencies much larger than the lattice frequency (see Fig. 5.7).

5.4.5 Array configuration dependence of transmission characteristics

In order to understand how specific transmission features are effected by the physical configuration of the array, a series of simulations are compared for several array configurations (see Fig. 5.8). The first configuration variation is in the spacing of rows in the direction of wave propagation (configuration B in Fig. 5.8). The horizontal spacing between columns

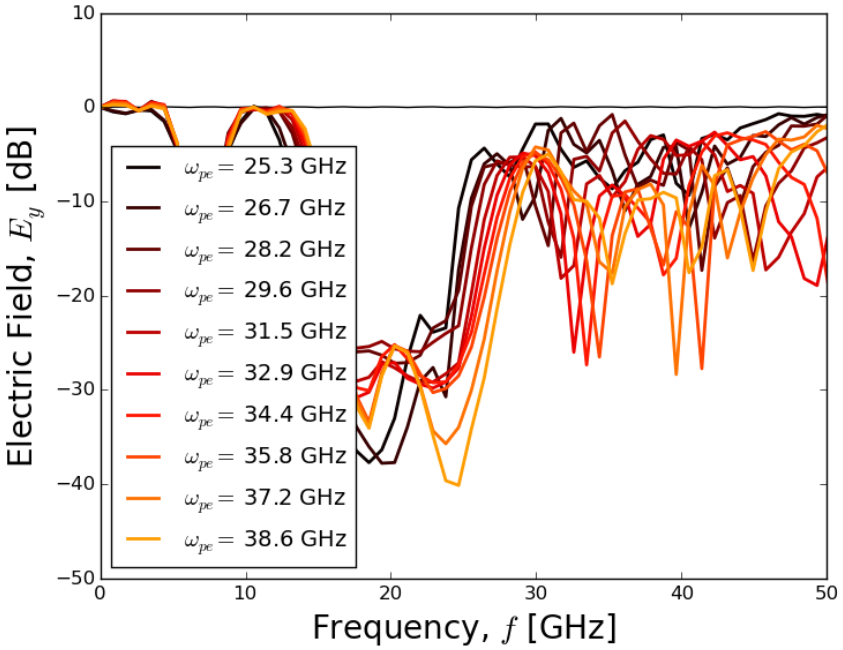

Figure 5.7: Transmission spectra in E_y for TE polarized fields with f_{pe}=25.3-38.6 GHz. The stationary photonic band gap persists at $\sim$ 7 GHz (obscured behind the legend), while the flat-band band gap shifts to higher frequencies with increasing plasma frequency. Complex interactions between flat-band and photonic band gaps can be seen above 30 GHz.

was increased by 25% to 2.5 cm from the experimental configuration (configuration A in Fig. 5.8). The transmission spectra are compared in Fig. 5.9. As the large plasma frequency space holds the most complexity, and is the least explored, plasma frequencies $f_{pe} \approx 3f_a$ and $4f_a$ are considered. The large flat-band band gaps (between $0.5f_{pe}$ and f_{pe}) remain relatively unchanged, while the narrow photonic band gaps both outside of, and within the flat-band region see considerable variation. This is understandable, as the flat-band frequency is dependent only on the plasma frequency, and the photonic band gaps are also functions of the lattice parameters.

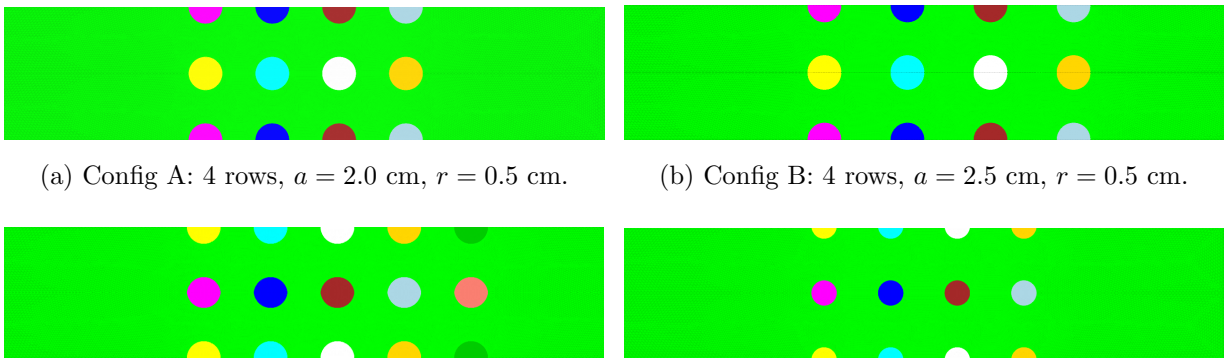

(a) Config A: 4 rows, $a = 2.0$ cm, $r = 0.5$ cm.

(b) Config B: 4 rows, $a = 2.5$ cm, $r = 0.5$ cm.

(c) Config C: 5 rows, $a = 2.0$ cm, $r = 0.5$ cm.

(d) Config D: 4 rows, $a = 2.0$ cm, $r = 0.375$ cm.

Figure 5.8: Simulation domain configurations used in Sec. 5.4 to examine array configuration impacts on transmission characteristics.

The next configuration parameter varied is the quantity of rows of plasma columns (4 in configuration A, and 5 in B). While the overall array length similar to configuration B (9 and 8.5 cm respectively), the effect on transmission spectra is much less pronounced (see Fig. 5.10). Low frequency spectra (< 15 GHz) are almost identical between the two cases, while there is more variation in the shallow, high frequency band gaps. A 25% increase in small scale spacing has a much larger effect than a 25% increase in column quantity, or overall array length. This also indicates that for some low frequency features, 4 rows of plasma columns is likely sufficient to approximate transmission characteristics of an array with any arbitrarily larger number of rows.

Finally, the plasma radius is varied relative to the lattice spacing. Configuration D (see Fig. 5.8) decreases the plasma column radius by 25% to 0.375 cm relative to configuration A (a 44% decrease in cross sectional area). Transmission spectra is compared for two plasma frequency cases in Fig. 5.11. While the lower band gaps (at 7 and 20 GHz) remain at the same frequencies, if somewhat less prominent, the higher frequency band gaps shift to lower

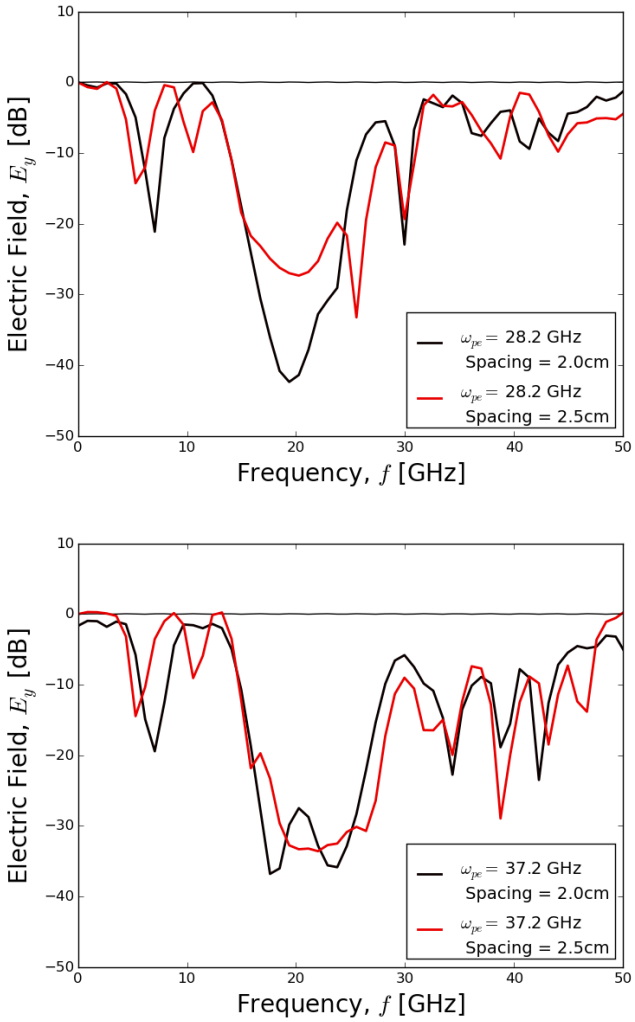

Figure 5.9: Transmission spectra for plasma column spacing at 2 cm (black) and 2.5 cm (red) in direction of wave propagation (configurations A and B in Fig. 5.8) for two different plasma frequencies. The large flat-band band gaps (between $0.5f_{pe}$ and f_{pe}) remain relatively unchanged, while the narrow photonic band gaps both outside of, and within the flat-band region see considerable variation.

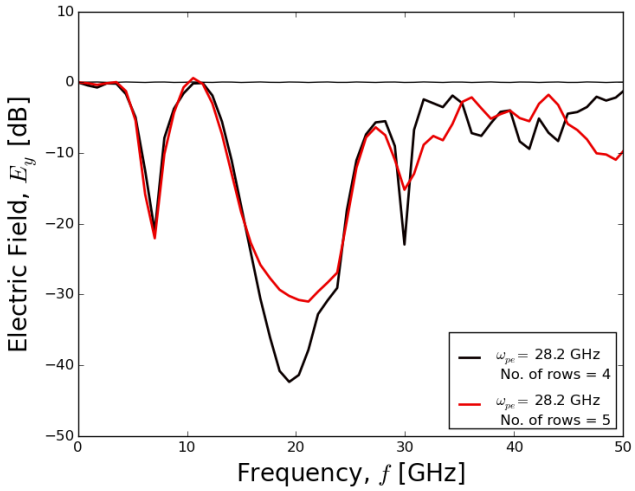

Figure 5.10: Transmission spectra for plasma column spacing at 2 cm and 4 (black) and 5 (red) plasma column rows (configurations A and C in Fig. 5.8) for $f_{pe} \approx 3f_a = 28.2$ GHz. Low frequency spectra (< 15 GHz) are unaffected by number of rows, while there is more variation in the shallow, high frequency band gaps.

frequencies by as much as 5 GHz.

5.4.6 Discussion and conclusions

In this section, the spectra generated by WARPXM simulations of a GHz plasma discharge tube PPC are compared to experimental results and are found to agree within expectations, with differences explainable by non-uniform density profiles in the real PPC and the existance of the quartz tube. Previous work in this dissertation had suggested that more intersting band gap behaviour would be exhibited when plasma frequencies are large compared to the lattice frequency, while the experiment was confined to $f_{pe} \leq f_a$. A series of simulations was undertaken to explore the regime of high f_{pe}/f_a ratios (up to $f_{pe}/f_a = 4$). Array configuration was also varied by 25% in array horrizontal spacing, number of columns, and column radius

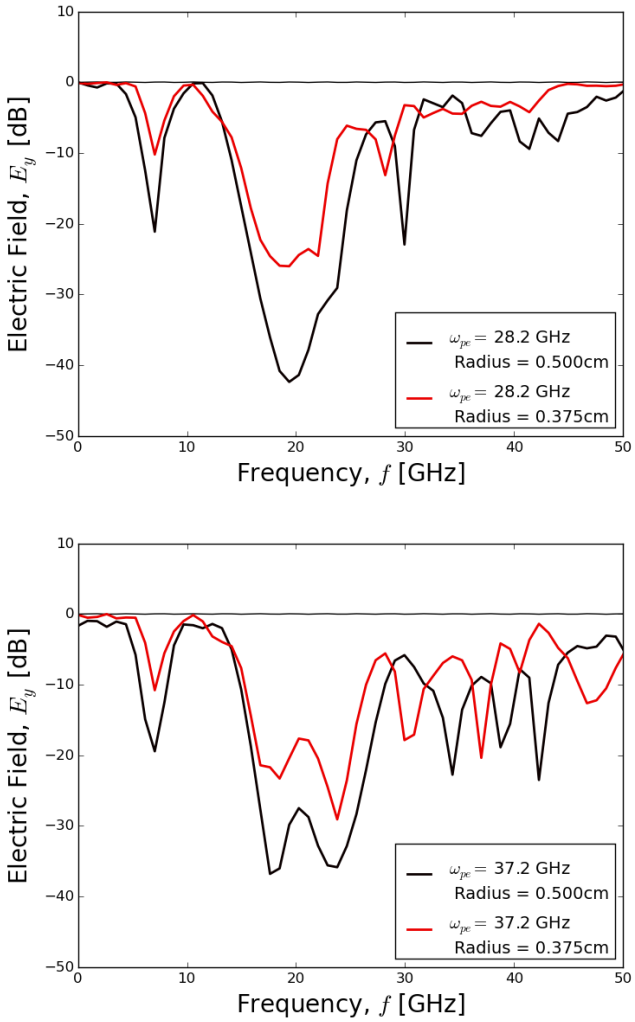

Figure 5.11: Transmission spectra for plasma column radii of 0.500 cm (black) and 0.375 cm (red) (configurations A and D in Fig. 5.8). Higher frequency band gaps shift to lower frequencies by as much as 5 GHz with a 25% change in column radius.

in order to understand the effects of physical configuration on high f_{pe}/f_a PPCs. Band gaps associated with flat-bands and surface plasmon resonances are found to be least effected by changes in array configuration, while photonic band gaps are the most effected.

Next, the findings in this section are be extended to a 2D THz plasma photonic crystal, and various non-ideal and non-linear phenomenon are studied: finite array extent, finite plasma temperature and non-uniform density profiles.

5.5 2D THz plasma photonic crystal

The GHz PPC explored in the previous section provided a basis for understanding the transmission spectra of 2D plasma photonic crystals, and how simulated spectra relate to experimental spectra of physical devices. It also allowed for an exploration of high f_{pe}/f_a PPCs and an understanding of how array configuration can effect higher frequency band gaps.

In order to expand this understanding to THz plasma photonic crystals, a similar PPC (rectangular 2D plasma column array) based on a cesium vapor plasma photonic crystal investigated by Righetti and Cappelli[77] is chosen as reference case. The lattice spacing of this device is $a = 500$ μm ($f_a = 0.6$ THz), and measured peak densities of $n > 10^{20}$ m^{-3} ($f_{pe} \approx 0.1$ THz). As the peak densities in the experiment are limited to well below the plasma frequency, the experimental parameters are used as a starting point for exploration of higher density, and therefore higher plasma frequency, theoretical PPC device. In this section, the 2D THz PPC is subjected to various non-ideal and non-linear phenomenon (finite array extent, finite plasma temperature, and non-uniform density profiles) and the effect on transmission spectra is explored.

5.5.1 THz PPC experimental parameters

The 2D THz PPC used as a reference configuration for the work in this section was created by Righetti and Cappelli[78, 77] by passing a TiSap constant wave laser through a microlense array, splitting the beam into a regularly spaced array (see Fig. 5.12). The laser array was then directed through a heated cesium filled cell. The laser excites a $6S_{1/2} - 6P_{3/2}$ transition

at 852 nm that results in laser ionization based on resonace saturation (LIBORS). The process can achieve plasma densities of $n > 10^{20}$ m^{-3} at input total laser power of 2.5 W, achieving filiment spaceings of $a = 500$ μm, column radii of $r = 75 - 100$ μm, total array diameter of $d \approx 4$ mm. Tranmission was measured for electromagnetic waves from 50 GHz to 0.6 THz in both TE and TM polarization.

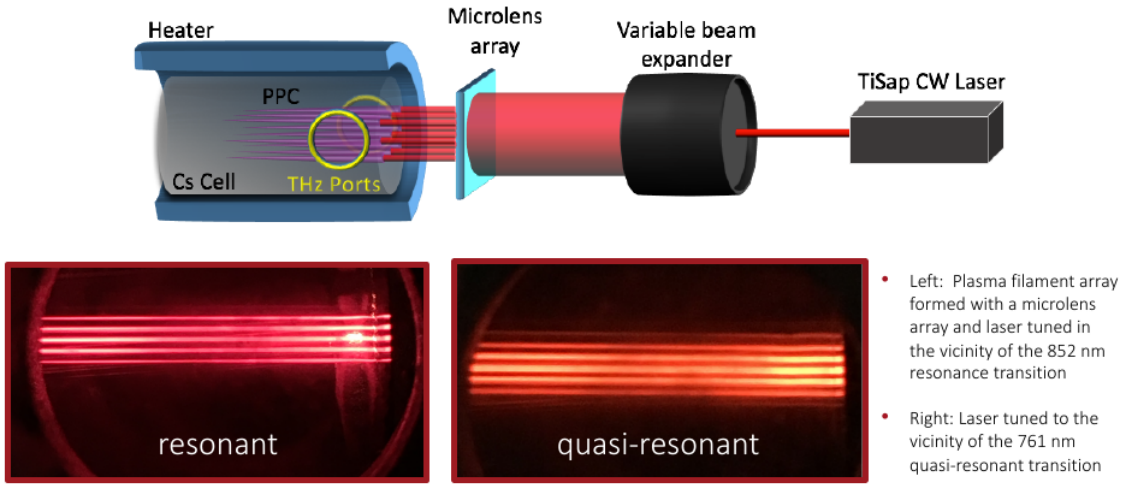

Figure 5.12: Cesium vapor plasma photonic crystal experimental set up (top), and visible light images of laser produced plasma filaments within the cesium cell for two different laser wavelengths[78].

5.5.2 Simulation parameters

The simulation effort looks to tackle several non-ideal aspects of the THz PPC: finite array size, non-uniform density profiles, finite temperature plasma, and plasma deformation in the presense of strong fields. Each of these aspects are explored independently in order to understand the impact of each. For all cases, the high f_{pe}/f_a is the region of interest.

The reference case is identical to that used to model the GHz PPC in Sec. 5.4: a semi-

infinite PPC (infinite perpendicular to the direction of wave propagation), with a cold, uniform density plasma columns in vacuum. Ions are assumed stationary for all cases, and collisional effects are not include. Modifications to the reference case are described in each section.

5.5.3 Cold, semi-infinite, uniform plasma PPC

The cold, semi-infinite, uniform plasma PPC is used as a base case against which non-ideal and non-linear PPC transmission characteristics are compared. In all "cold" plasma models, the full two-fluid model is reduced to the Drude-type model described in Eqs. (3.23), (3.24), and (3.25). As collisionless photonic crystals are scale indepent, the primary features of the THz PPC are identical to that of the GHz PPC the same fill fraction $f = \pi r^2/a^2$ and plasma frequency to lattice frequency ratio f_{pe}/f_a. In Fig. 5.13 the transmission spectra for a range of plasma frequencies ($f_{pe} = 0.25f_a - 2.2f_a$) are presented. The complex interplay of plasmon and photonic band gaps is clear. The large band gaps at frequencies above the lattice frequency for large $f_{pe} = 2.2f_a$ (purple) are even more obvious in this particular spectra example.

As the radius of the plasma filaments is not known with certainty, two different radii are compared in Fig. 5.14 for a subset of plasma frequencies. Similar to the radius comparison in Fig. 5.11 for the GHz PPC, the smaller radius shifts the band gaps of plasma frequencies below $f_a/2$ to higher frequencies, and those above to lower frequencies. The depth of attenuation is generally lower for the smaller radii, though not universal.

5.5.4 Cold, semi-infinite, non-uniform plasma PPC

Non-uniform density profiles are ubiquitous in plasmas, as discussed in Chaps. 3 and 4. Both the GHz and THz experimental PPCs have gradients in density, with the latter having only smooth profiles and no discontinuities. Additionally, large plasma deformations due to

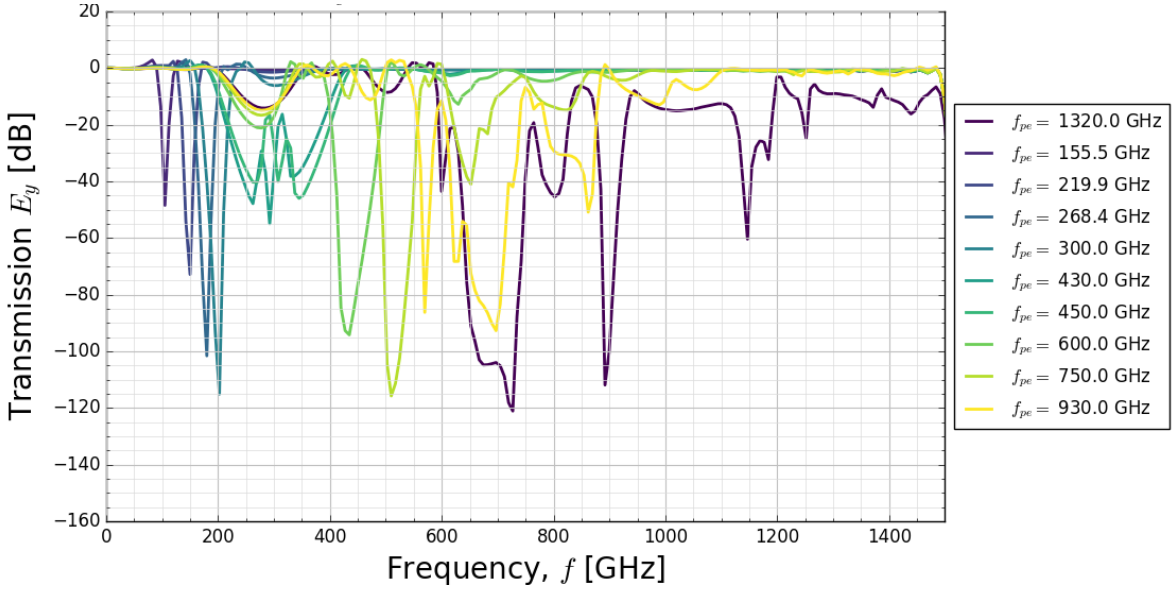

Figure 5.13: Transmission spectra in TE for the cold, semi-infinite, uniform plasma density THz PPC (4 rows, $a = 500$ μm, $r = 100$ μm) for a range of plasma frequencies ($f_{pe} = 0.25f_a - 2.2f_a$). As in the GHz case, large band gaps exist at frequencies above the lattice frequency for large $f_{pe} = 2.2f_a$ (purple).

strong fields also cause non-uniform profiles. While the effect of non-uniform density profiles has been explored in this disseration through dispersion and band gap maps, the impact on transmission spectra has not yet been discussed. To understand how non-uniform profiles effect transmission spectra, a series of simulations is performed with inverted parabolic density profiles of increasing order (see Fig. 5.15).

Two plasma frequencies are chosen to demonstrate the impact of density gradients on plasmon resonance band gaps and band gaps that contain both plasmon and photonic effects. The first case (left panel Fig. 5.15) maintains a maximum plasma frequency is $f_{pe} = f_a/6 = 100$ GHz. The band gap is due to plasmon resonances only and expands to lower frequencies with increasing gradients, as was shown in Chap. 4. What cannot be seen from dispersion

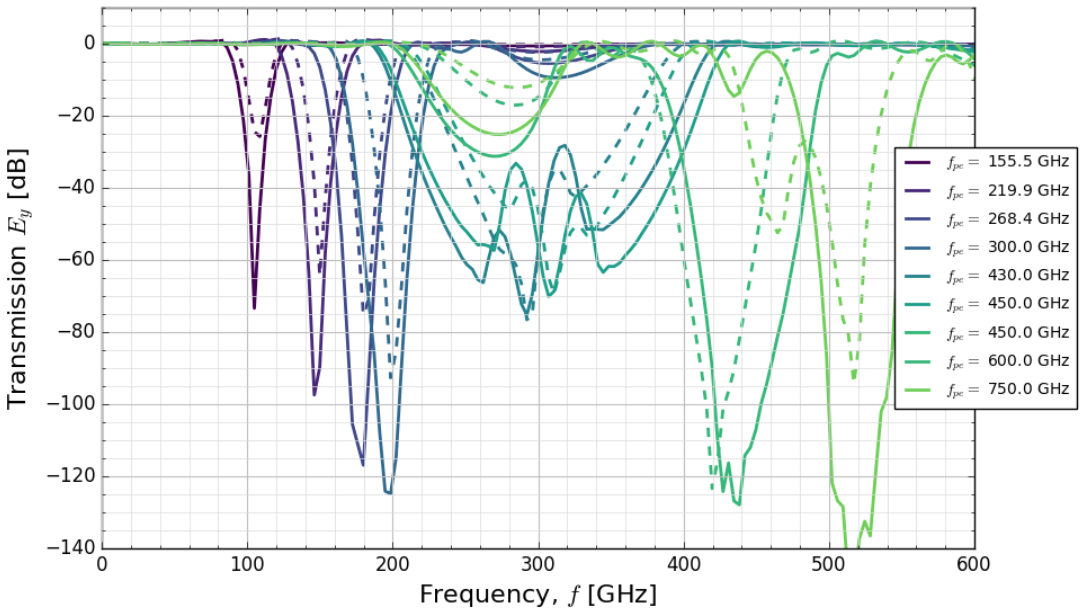

Figure 5.14: Transmission spectra in TE for the cold, semi-infinite, uniform plasma density THz PPC (4 rows, $a = 500$ μm) for two plasma radii, $r = 100$ μm (solid) and $r = 100$ μm (dashed) for a range of plasma frequencies ($f_{pe} = 0.25f_a - 1.25f_a$).

information is how not all parts of the flat band region attenuate equally, and that even though the overall width of the band gap remains constant for all cases with gradients, the frequency of the maximum attentuation shifts to lower and lower frequencies.

In the second case (right panel Fig. 5.15), the maximum frequency is $f_{pe} = 2f_a/3 =$ 400 GHz. Wiggles in spectra are due to simulation spatial resolution and are not physical. In this case the band gap is a combination of photonic and plasmonic effects. The narrow photonic band gap ($\sim$ 300 GHz) creates a Fano-type resonance, as described by Righetti *et al.*[34]. As the density gradients become more pronounced, the resonance becomes less so.

Overall, the transmission spectra created with the semi-finite PPC simulation support

the findings with the infinite model in the previous chapter, as well as further support the analysis of the experimental versus simulation spectra. Density gradients cause band gaps to both become more broad, and more shallow, as well as soften the effect of sharp Fano-type resonant features. Sharp gradients enforced by quartz tubes could sharpen the Fano resonance type features (of which there is some evidence in the experimental GHz spectra). On the other hand, the THz PPC should have little or no Fano-type resonance activity.

5.5.5 Cold, finite, uniform plasma PPC

Real world photonic crystals are finite in all dimensions. Understanding the impact of finite array extent is therefore also important in interpreting and predicting the performance of potential devices. In this section, the simulation domain is modified to contain a finite 2D PPC array surounded by vacuum (see Fig. 5.16). As the domain is much larger in the y direction than the semi-infinite case, the relfection and detection regions are trunkated, and replaced with a lacuna based open boundary condition implemented for this purpose (see Appx. B).

The transmission spectra are compared with semi-inifinite PPC spectra with the same quantity of rows in Fig. 5.17. The most interesting difference occurs at low f_{pe} band gaps where diffraction around crystal edges cause constructive interference for wavelengths on the order of the total crystal size ($\lambda = 1-3$ mm, or $f = 100-300$ GHz). Otherwise array extent perpendicular to the direction of propegation does not significantly impact the location and shape of the transmission spectra.

5.5.6 Warm, semi-infinite, uniform plasma PPC

All simulations presented thus far in this dissertation have assumed cold plasma, and have reduced the plasma model to the Drude model for electron transport. The model choice is a common one, and was shown earlier in this chapter to agree fairly well with experiment.

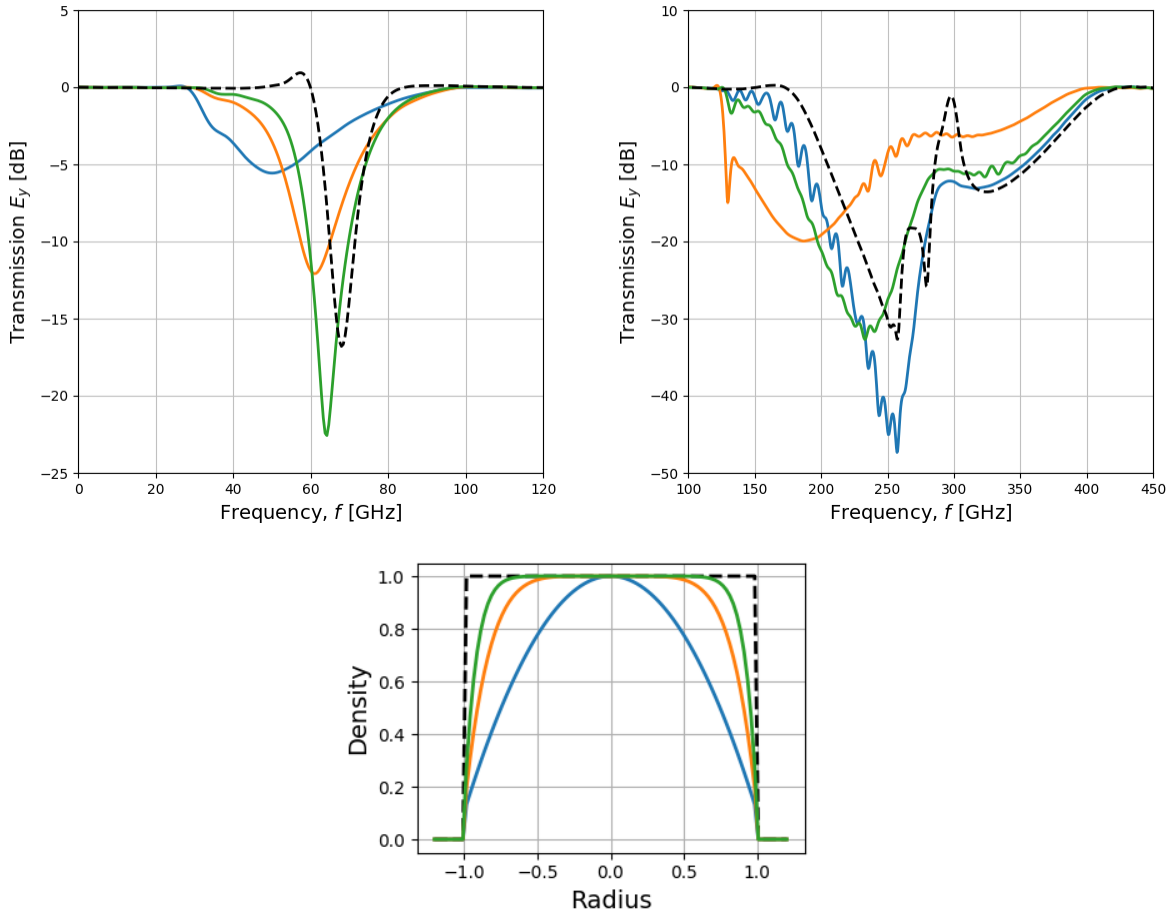

Figure 5.15: Transmission spectra for the cold, semi-infinite THz PPC with parabolic density profiles (bottom). (Left) Maximum plasma frequency is $f_{pe} = f_a/6 = 100$ GHz, the band gap is due to plasmon resonances only, which expands with increasing gradients as shown in Chap. 4. (Right) Maximum frequency is $f_{pe} = 2f_a/3 = 400$ GHz, and the band gap is a combination of photonic and plasmonic effects. Wiggles in spectra are due to simulation spatial resolution and are not physical. The Fano-type resonance at ~ 300 GHz, becomes less sharp with increasing gradients.

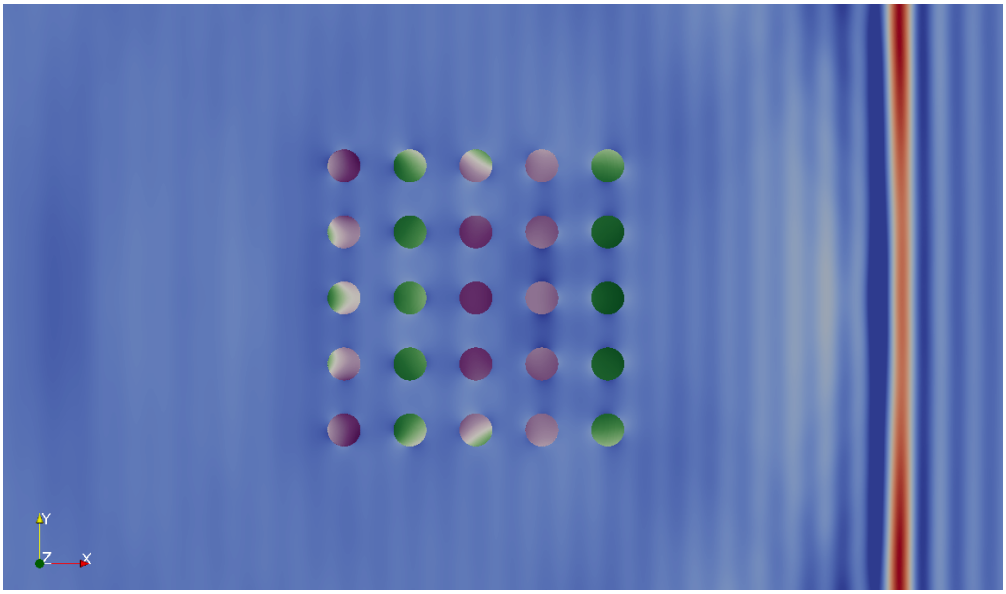

Figure 5.16: A finite 2D PPC simulation domain for a 5x5 array. Background contours (blue-red) are electric field magnitude. Column contours (purple-green) are electron momentum in y.

In high power PPCs, plasmas may absorb energy from the incident THz waves and can no longer be assumed to be cold. In this section, the full electron fluid model described in Eqs. (5.1)-(5.2) is evolved and compared with the Drude-type model transmission spectra for the same case (see Fig. 5.18). The warm plasma is set at $T_e = 100$ eV. As is clear from the comparison, plasma temperature has almost no effect on transmission characteristics.

This can be understood from the effective permittivity of the plasma, on which the transmission properties depend

$$\epsilon_{eff} = 1 - \frac{\omega_{pe}^2}{\omega^2(1 + i\nu_m/\omega)} \tag{5.8}$$

where ν_m is the electron momentum-transfer collision frequency. In this work, the collision frequency is assumed to be much less than the plasma frequency ($\nu_m \ll \omega_{pe}$). While not

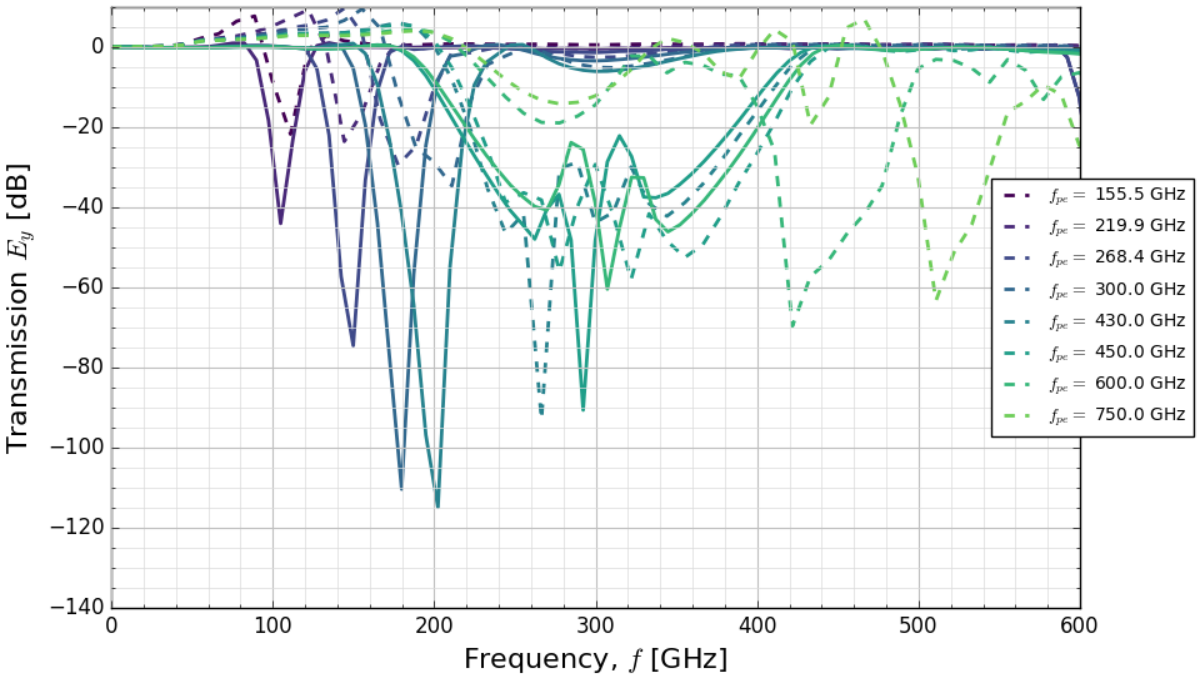

Figure 5.17: Transmission spectra for the cold THz PPC with semi-infinite 3 row (solid) and finite 3x3 (dashed) plasma column arrays. The low band gaps are reduced in intensity, and are proceeded by a greater than unity transmission region due to lensing around the crystal.

strictly true for the plasmas of interest, the effect of dissipation on PPC transmission characteristics has been well characterized[43, 54], and is not the primary objective of this study. Neglecting collisions removes any direct dependence of ϵ_{eff} on temperature. Furthermore, ν_m in a full ionized plasma is due to Couloumb collisions, which is an inverse function of temperature. It is therefore not expected that plasma temperature should have a significant impact on transmission spectra of fully ionized plasmas, except to decrease the collision frequency and lessen absorption.

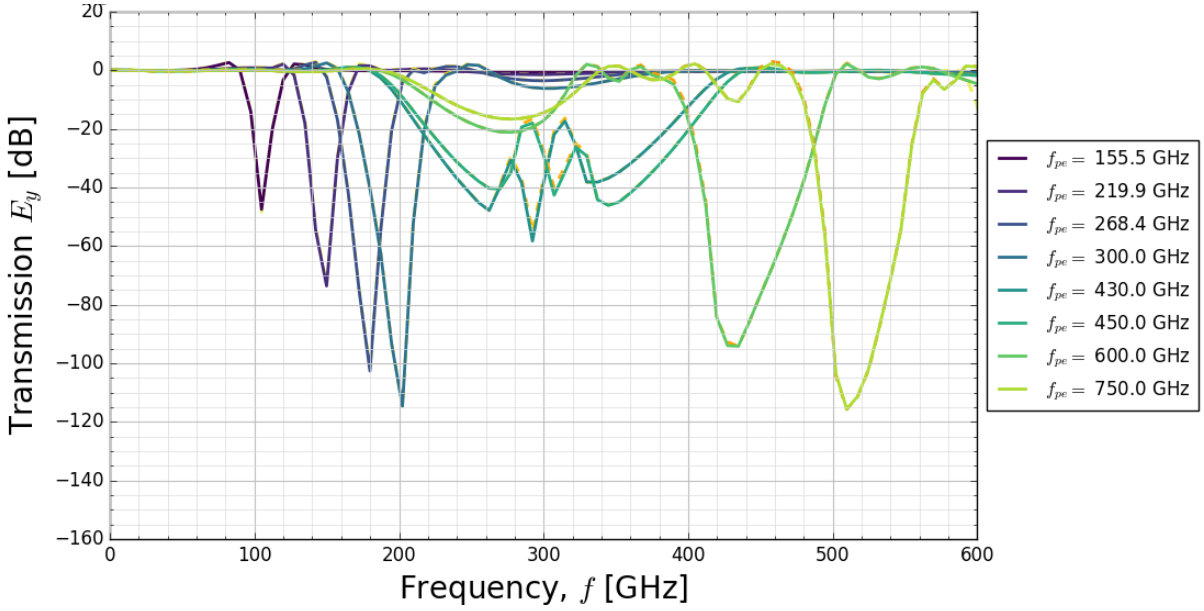

Figure 5.18: Transmission spectra at two different temperatures: 0.028 eV (solid) and 100 eV (dashed).

5.5.7 Warm, uniform plasma in the the presence of strong fields

In this last section, the presence of strong fields in a fully ionized THz PPC is explored. These high amplitude fields can be due to high power incident THz radiation, but can also arise from resonances within the PPC that accumulate energy over time. One example is defects created in PPCs by removing a single element within the array. The cavity accumulates EM wave energy to the point of breakdown (see Chap. 6 for a further discussion). Surface plasmons can also accumulate energy within the plasma columns when subject to EM frequencies close to the surface plasmon frequency. As discussed in Chap. 2, surface plasmons have frequencies that are a function of plasma frequency, fill fraction, and mode number (see Fig. 5.19). Surface plasmons in PPC arrays couple with neighboring plasmons constructively or destructively, depending on spacing. In Fig. 5.20, neighbooring columns continue to

oscillate after a broad band THz pulse has passed by.

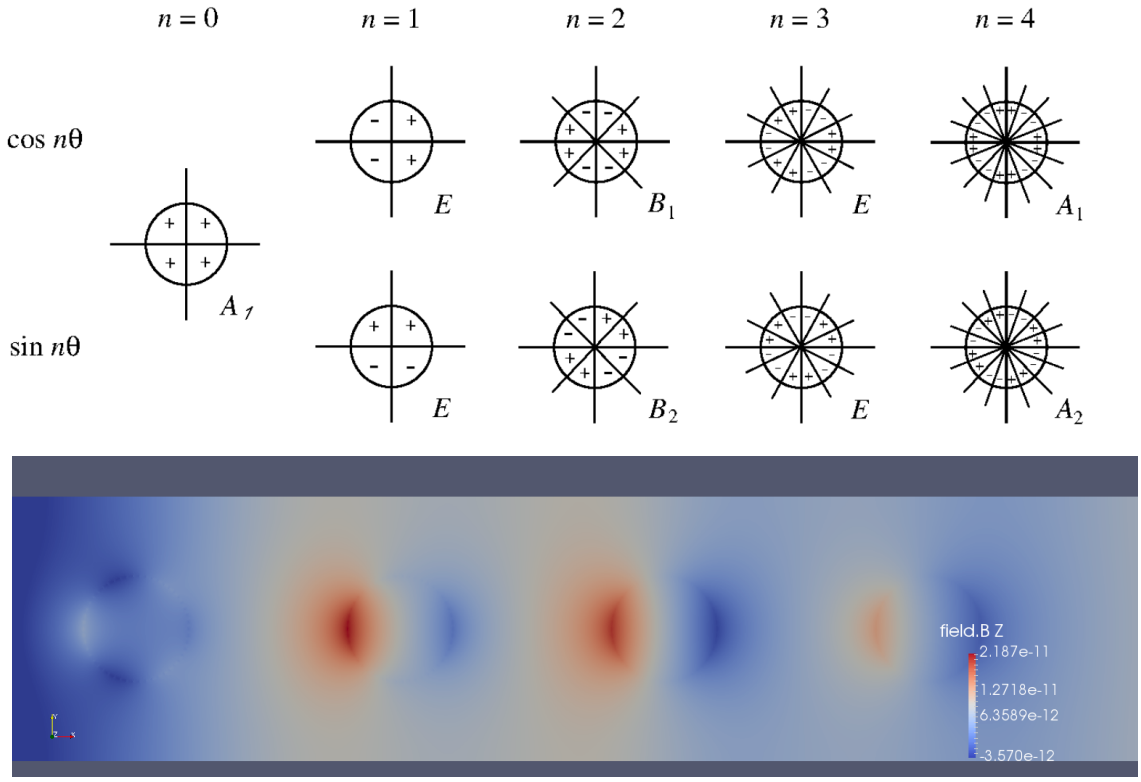

Figure 5.19: (Top) Surface plasmon polariton mode configuration for modes $n = 0$ through 4[32]. (Bottom) A snapshot of four plasma columns in a WARPXM simulation showing surface plasmons with mode numbers 1 and 3. Contours in B_z.

In order to understand how the plasma may deform in the presence of these strong fields and plasma oscillations, a high resolution simulation was run for a single column subject to a large amplitude electric field in y. In Fig. 5.21, contours in normalized mass density (relative to the proton mass) after four plasma oscillation periods, showing density deformation on the top and bottom, and density waves propegating into the interior of the column.

While the deformation amplitude may be large in strong fields, barring non-linear effects,

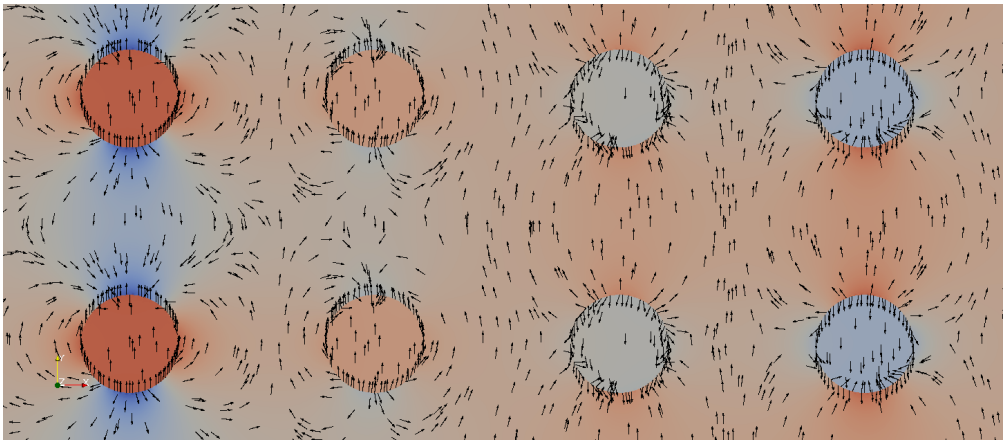

Figure 5.20: Close up of WARPXM simulation domain showing electric field magnitude (contours) and orientation (arrows) after a broad band THz pulse has passed through. The plasma columns continue to oscillate, and the fields in neighboring columns interact.

the length scale of the deformations is expected to be on the order of the Debye length

$$\lambda_D = \sqrt{\frac{\epsilon_o n e^2}{kT}}. \tag{5.9}$$

At 100 eV for a $n = 10^{21}$ m^{-3} plasma ($f_{pe} \approx 300$ GHz) the Debye length is less than a micron, barring non-linear effects fluid deformation is not likely to have a large impact on transmission spectra. What is more plausable is that the plasma is not fully ionized, and high amplitude EM THz waves will drive ionization. In the next chapter, plasma formation and interaction with THz waves in the context of PPC devices is explored.

5.6 Conclusions

In this chapter, GHz and THz 2D plasma photonic crystals are explored with a two-fluid 5-moment plasma model. Plasma models allow for intrinsic dynamics, like plasma heating and plasma deformation in response to strong fields. Once validated, these plasma models can push into regimes hard to access with current experiments. Plasma models can also

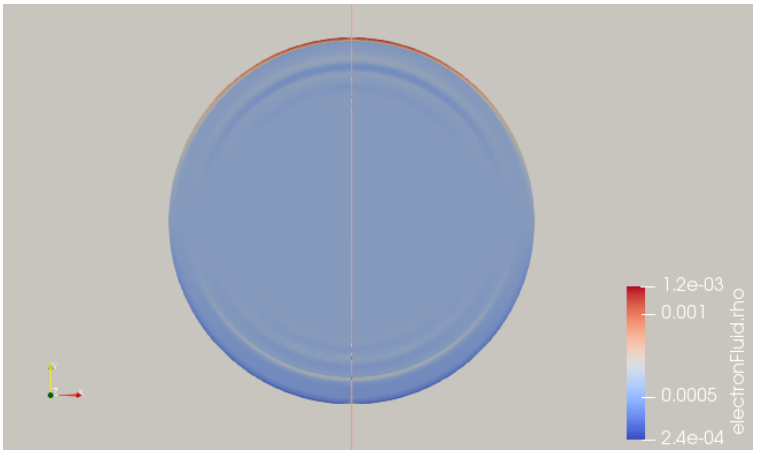

Figure 5.21: Contours in normalized mass density (relative to the proton mass) of a single plasma column subject to an oscillating electric field close to the plasmon frequency. Image is taken after four plasma oscillation periods. Density deformation scale length is on the order of the Debye length.

approximate some of the complexities of physical embodiments, like finite size, or diagnostic configurations, versus ideal analytical or theoretical models that look at the ideal case. Furthermore, models can explore real time plasma and field dynamics allowing for a greater intuitive understanding of plasma-field interactions.

First, the spectra generated by WARPXM simulations of a GHz plasma discharge tube PPC were compared to experimental results and were found to agree within expectations, with differences explainable by non-uniform density profiles in the real PPC and the existance of the quartz tube. Previous work in this dissertation had suggested that more intersting band gap behaviour would be exhibited when plasma frequencies were large compared to the lattice frequency, while the experiment was confined to $f_{pe} \leq f_a$. A series of simulations was undertaken to explore the regime of high f_{pe}/f_a ratios (up to $f_{pe}/f_a = 4$). Array configuration was also varied by 25% in array horrizontal spacing, number of columns, and column radius

in order to understand the effects of physical configuration on high f_{pe}/f_a PPCs. Band gaps associated with flat-bands and surface plasmon resonances were found to be least effected by changes in array configuration, while photonic band gaps were the most effected.

Once the transmission characterstics of the GHz PPC were well characterized, the findings were extended to a 2D THz plasma photonic crystal using a cesium vapor laser plasma PPC as reference case. Various non-ideal and non-linear phenomenon were explored.

Transmission spectra of non-uniform semi-finite PPC simulations support the findings with the infinite model in the previous chapter, as well as further support the analysis of the experimental versus simulation spectra. Density gradients cause band gaps to both become more broad, and more shallow, as well as soften the effect of sharp Fano-type resonant features. Sharp gradients enforced by quartz tubes could sharpen the Fano resonance type features (of which there is some evidence in the experimental GHz spectra). On the other hand, the THz PPC should see little or no Fano-type resonance activity.

Finite array extent resulted in diffraction around crystal edges causing constructive interference for wavelengths on the order of the total crystal size ($\lambda = 1 - 3$ mm, or $f = 100 - 300$ GHz), though otherwise the finite extent did not significantly impact the location and shape of the transmission spectra. Temperature and strong fields are found to have almost no impact on the transmission spectra in a dissipationless, fully ionized plasma.

Overall, this study confirms the conclusions of Chaps. 3 and 4 that some of the most interesting band gap behavior occurs when $f_{pe} \gtrsim f_a$, and that these band gaps are heavily dependent on the presence (or absence) of gradients in the density profile. On the other hand, fluid effects like temperature and deformation in the presence in strong fields are not found to have significant impact when plasmas are fully ionized. This is likely not true when the plasma is not fully ionized. In the next chapter (Chap. 6), plasma formation and interaction with THz waves in the context of partially or non-ionized PPC devices are explored.

Chapter 6

MODELING PLASMA FORMATION IN A THZ PLASMA PHOTONIC CRYSTAL PASSIVE POWER MODULATION DEVICE

The previous chapter looked out how fully ionized PPCs respond to the strong fields present in high power THz systems. Many of the proposed PPC devices involve partially ionized plasmas. At sufficiently high power, further ionization of the surrounding gas is inevitable, resulting in a non-linear PPC response. This effect can be harnessed intentionally. Solid state photonic crystals can be functionalized with self-initiated plasmas in resonant defects to provide passive power modulation. Understanding the plasma's formation, as well its interaction with the EM fields, is necessary to the design of high power THz devices.

Self-consistent modeling of THz breakdown is challenging as it covers many orders of magnitude in speed (light speed to the neutral thermal speed) and ionization fraction (neutral gas to near full ionization). Models typically used in low temperature and process plasma simulations rely on reaction rate and transport coefficients calculated by third-party Boltzmann solvers. Self-consistent solution of the Boltzmann equation is often necessary in low temperature plasmas as the electron velocity distribution function (EVDF) departs from a Maxwellian, with significant impact on reactions and transport. The EVDF is a function of interaction cross sections, electric field strength, electric field oscillation frequency, gas temperature, ionization fraction, and temporal and spatial gradients. In order to simplify calculations, all but one variable is held constant, in both time and space. In contrast, in fully ionized plasmas at atmospheric densities and low temperatures, the Coulomb collision frequency becomes dominant, driving the EVDF towards a Maxwellian. The plasma can

then be reliably modeled by fluid moment models with well established closures (isotropic pressure or Braginskii). Maxwellian EVDFs also allow for reaction rates to become functions of only electron temperature and relative velocity.

This chapter explores the validity of using a three-species (electron-ion-neutral atom) 5-moment model developed by Meier and Shumlak[15] for modeling THz plasma formation. Correction terms to collision and reaction frequencies are proposed to extend the region of validity. A PPC passive power modulation device[16] is used as a benchmark, as it has been well explored experimentally and theoretically for the low- to mid-GHz range.

6.1 Passive PPC power limiting device as test case

High power PPC THz devices that will experience ionization can take many forms. In order to focus modeling efforts, a device is chosen where plasma formation is due to incident THz radiation only (in contrast to devices where plasmas are preexisting and created through external means). It is also desirable to have a plasma with simple geometry. To this end, a PPC passive power limiting device by Parsons *et al.*[16] for the low-GHz regime is selected as a test case.

The passive power modulation device consists of a two-dimensional dielectric photonic crystal in a copper wave guide. The PC has a band-gap, or stop-band, from 35-50 GHz (see Fig. 6.1). A single rod is removed from the center of the crystal, creating a pass-band within the stop-band at $\sim$43 GHz. The defect functions as a resonant cavity with electric field amplitudes reaching $>$ 200 kV/m for an input power of 1.5 W. Under these conditions, breakdown occurs. As the plasma forms within the defect, the narrow pass-band is attenuated (see Fig. 6.2).

A similar device with a pass band frequency of 9.5 GHz has been modeled with qualitative success by Gregório *et al.*[79]. The study specifically examines resonant cavity breakdown at 9.5 GHz in argon. A drift-diffusion model is used to evolve the density and momentum

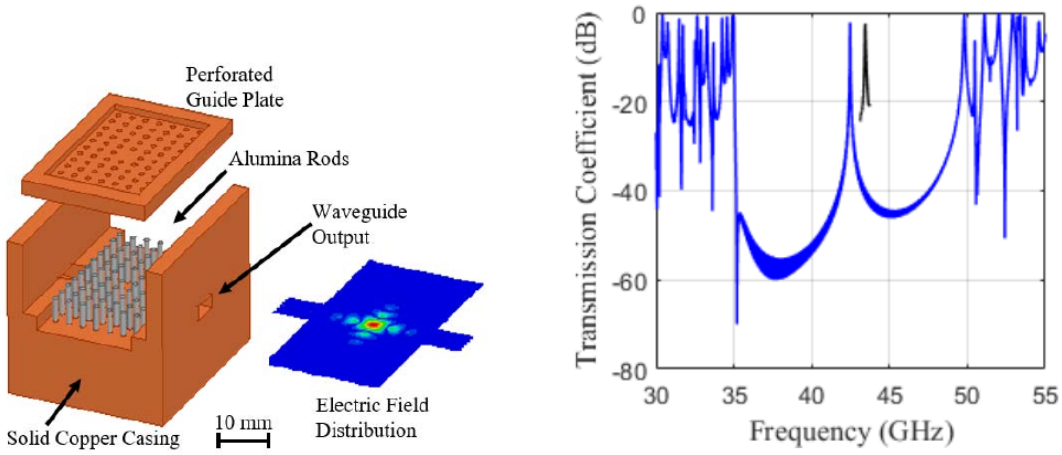

Figure 6.1: A passive power modulation device by Parsons *et al.*[16] that consists of dielectric photonic crystal in a copper waveguide (left). A rod is removed to create a defect, resulting in a narrow pass-band within the band gap. The right panel shows simulated (blue) and measured (black) transmission spectra.

equations for all charged species (electrons, ions Ar^+ and Ar_2^+, and several grouped excited states), as well as an energy equation for electrons. The interaction of species is mediated through 26 reactions. Reaction rates and transport coefficients are calculated through a combination of analytical models[80] and the Boltzmann solver Bolsig+[17] using the local mean energy approximation[81].

Peak densities and formation rates were found to generally agree with experiment, barring experimental imperfections and the difference between a 3D device and a 2D simulation. Power modulation was also successfully demonstrated.

The device described above has been demonstrated for low-GHz range, with electron densities not exceeding 10^{19} m^{-3}. A similar device for THz frequencies would require electron densities as high as 10^{25} m^{-3}, and PC rod spacing on the order of 10s of microns (see Table 6.1). Current microplasma capabilities are limited in this space, as well as availability of

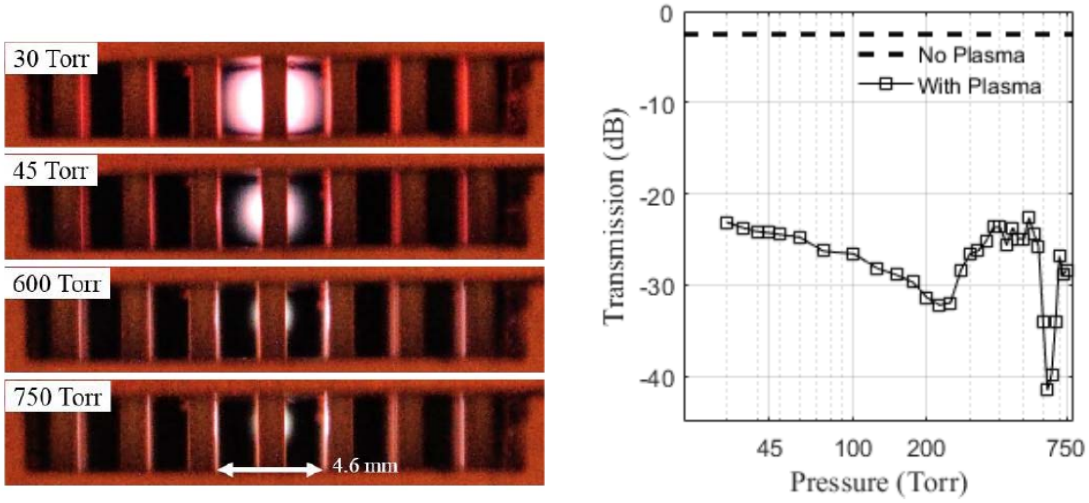

Figure 6.2: (Left) visible light images of steady state plasma in PPC defect at 30, 45, 600 and 750 Torr. (Right) transmitted power (S_{12}) at various pressures for PPC with and without plasma. Power input is 1.5 W at 43.4 GHz

high power THz sources[82]. Therefore simulation can be a useful tool in exploring theoretical THz devices.

In order to capture the relevant physics the model will need to capture: 1) electrodynamics and self-consistent THz wave propagation and interaction with electron and ion species, 2) plasma and neutral gas dynamics, including density, momentum, and energy transport for each species, as well as charged particle interaction with fields through the Lorentz force, and 3) inter-species collisions and reactions (elastic charged particle and neutral particle scattering, ionization, recombination, and other inelastic processes). In the following section, the parameter space of the proposed device is characterized by degree to which statistical models are needed to capture transport and reaction physics. Common modeling approaches for partially ionized plasmas that apply to this regime are reviewed.

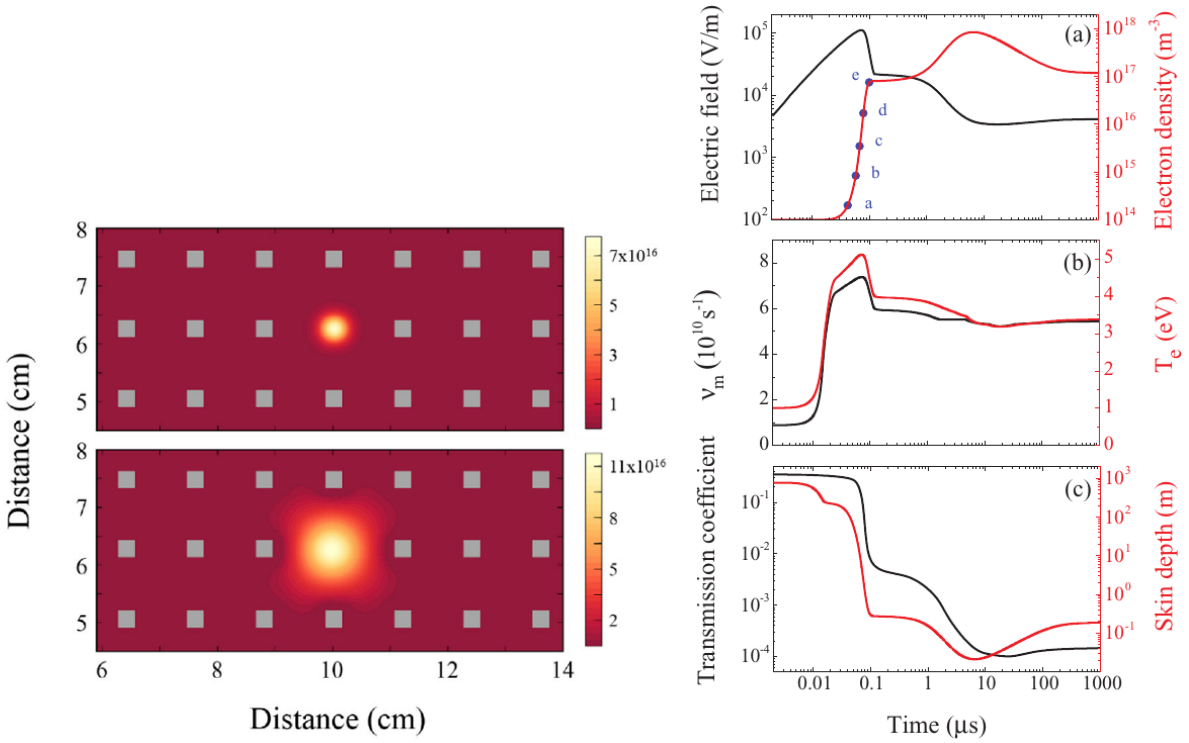

Figure 6.3: Simulation results of 9.5 GHz passive PPC power modulation device[79]. Color contours of electron density (m^{-3}) at times $t = 0.1$ μs (top left) and $t = 1$ ms (bottom left). Various plasma and field parameters in time (right).

6.2 Selection of modeling approaches for THz plasmas in PPCs

Self-consistent modeling of THz breakdown is challenging as it can involve hundreds of species and thousands of reactions for even simple molecular gases. Complexity can be greatly reduced when the gas is in global or local thermal equilibrium. The degree to which a plasma is in thermal equilibrium is a function of the ratio of diffusive processes that drive a species towards equilibrium (i.e. particle scattering) and processes that drive the species away from equilibrium (i.e. spatial gradients and reactions). The ratio of collisional processes

Table 6.1: Parameter regime of a theoretical THz PPC device as compared to a low GHz device.

	GHz device	THz device
Mid-gap frequency	10-40 GHz	1-10 THz
Rod spacing, a	2.8 mm	10-100 microns
Electron density, n_e	$10^{18} - 10^{19}$ m^{-3}	$10^{22} - 10^{24}$ m^{-3}
Neutral gas pressure, p_n	$30 - 750$ Torr	same
Neutral gas density, n_n at 300 K	$10^{24} - 2.5 \times 10^{25}$	same
Peak ionization fraction, $n_e/(n_e + n_n)$	10^{-4}	~ 1
Electron-neutral collision frequency[1], ν_{en}	10^{12} s^{-1}	~ 0
Electron-ion collision frequency[1], ν_{ei}	10^{9} s^{-1}	10^{13} s^{-1}
Peak electric field strength[2], E_{max}	10^{5} V / m	same

[1] Collision frequency in peak ionization region.

[2] From effective breakdown field assumption $E_{eff} = 2^{-1/2}(1 + \omega^2/\nu^2)^{-1/2} E_{max}$[17].

to spatial gradient scale lengths is represented by the Knudsen number, Kn $= \lambda_{mfp}/L$, where λ_{mfp} is the mean free path and L is the length scale of the plasma. A value of Kn greater than one indicates that a statistical model for transport is required, whereas values less than one are sufficiently captured by fluid models that assume normal particle distributions.

The degree to which reaction and excitation processes dominate over scattering collisions will be approximated here by Gr $= n_{Gr}/n_e$ where n_{Gr} is the Griem[83] electron number density criterion for complete local thermal equilibrium (LTE)

$$n_{Gr} = 10^{23} Z^7 (T_e/E_{ion,Z})^{1/2} \quad \text{m}^{-3} \tag{6.1}$$

where Z is the degree of ionization, $E_{ion,z}$ is the Z^{th} ionization energy, and T_e is in eV.

Similarly to the Knudsen number, values of Gr greater than one indicate that exited state populations are not in thermal equilibrium and must be modeled statistically, and values less than one indicate LTE and equal energy partition between states. Plasma with electron densities slightly above this criterion may still be in partial LTE, where some states above a certain energy level are in LTE, and those below are not[83].

The requirements for LTE are in most cases more strict than those for fluid transport modeling. For example, a 10 micron plasma surrounded by neutral gas with a peak electron density of 10^{25} m^{-3} will have a Kn $\lesssim 10^{-2}$ everywhere. The same plasma, assuming electron temperatures of $0.025 - 15$ eV, typical of THz plasmas, Gr is less than one only the region where electron densities exceed $\gtrsim 10^{22} - 10^{23}$ m^{-3} depending on the temperature. A fluid model is therefore appropriate for electron transport everywhere, but LTE can only be assumed for a small region where the plasma is most dense.

6.2.1 The Boltzmann system for non-LTE plasmas-neutral mixtures

Modeling non-LTE plasmas requires the solution of the Boltzmann equation for each particle species, coupled through particle collisions and interactions with collective fields governed by Maxwell's equations. Each Boltzmann equation evolves the velocity distribution function $f_\alpha = f_\alpha(\boldsymbol{r}, \boldsymbol{v}, t)$ for species α (in a reacting plasmas this includes electrons and excited states of neutral atoms, ions, and molecules):

$$\frac{\partial f_\alpha}{\partial_t} + \boldsymbol{v} \cdot \nabla_x f_\alpha + \frac{q_\alpha}{m_\alpha}(\boldsymbol{E} + \boldsymbol{v} \times \boldsymbol{B}) \cdot \nabla_v f_\alpha = \left.\frac{\partial f_\alpha}{\partial t}\right|_{collisions} \tag{6.2}$$

where $\boldsymbol{E}$ and $\boldsymbol{B}$ are evolved through Maxwell's equations

$$\nabla \times \boldsymbol{E} = -\frac{\partial \boldsymbol{B}}{\partial t}, \quad \nabla \times \boldsymbol{B} = \mu_0 \boldsymbol{j} + \varepsilon_0 \mu_0 \frac{\partial \boldsymbol{E}}{\partial t}$$

$$\nabla \cdot \boldsymbol{E} = \frac{\rho_c}{\varepsilon_0}, \quad \nabla \cdot \boldsymbol{B} = 0, \tag{6.3}$$

where $\boldsymbol{j}$ is the current density, ρ_c is the charge density, and μ_0 and ε_0 are the vacuum permeability and permittivity, respectively. The RHS of Eq. (6.2) represents the sum of all elastic and inelastic collisions.

$$\left.\frac{\partial f_\alpha}{\partial t}\right|_{collisions} = \sum_\beta C^{scat}_{\alpha\beta}(f_\alpha, f_\beta) + C^{react}_{\alpha\beta}(f_\alpha, f_\beta) + \sum_\gamma C^{scat}_{\alpha\beta\gamma}(f_\alpha, f_\beta, f_\gamma) + C^{react}_{\alpha\beta\gamma}(f_\alpha, f_\beta, f_\gamma) + \ldots, \tag{6.4}$$

where $C^{scat}_{\alpha\beta}$ is the binary elastic collision operator and $C^{react}_{\alpha\beta}$ is the binary inelastic, or reacting collision operator, between species α and β. Ternary and higher collision operators are indicated by additional subscripts. Each collision operator is dependent on the distribution functions of all colliding species, before and after the collision. Binary collisions are by far the most common, and are described by the classic Boltzmann collision operator for elastic 2-body collisions

$$\left.\frac{df}{dt}\right|_{coll} = \int\int [f'(v_\alpha)f'(v_\beta) - f(v_\alpha)f(v_\beta)] g \sigma_{\alpha\beta}(g,\chi) d\Omega d^2\boldsymbol{v}_\beta \tag{6.5}$$

where primes denote distribution functions after the collisions, $g = |\boldsymbol{v}_\alpha - \boldsymbol{V}_\beta|$ is the relative speed between species, $\sigma_{\alpha\beta}(g,\chi)$ is the differential cross section at relative speed g and scattering angle χ, and Ω is the differential solid angle. Similar expressions can be derived for multi-body, inelastic, and reacting collisions.

Solving the 6D (3D3V) Boltzmann equation for each species, along with calculating the collision operators, constitutes a truly formidable problem. Two major classes of approaches exist for solving this problem. Particle-in-cell (PIC) represent the distribution function with a reduced number of "super-particles" that are advected through a physical space grid, interacting both with electromagnetic fields and with each other. The collective electromagnetic fields are evolved through Poisson or Maxwell's equations, with charge density and current density sources calculated through intelligent integration over the super-particle distributions. Particle collisions and reactions are simplified through the application of Monte Carlo

methods. See the review by Alves *et al.*[84] for further reading on PIC methods in partially ionized non-LTE plasmas.

The Boltzmann system can also be solved in it's continuous form by applying certain assumptions about the form of the distribution function. In the next section, several common methods are reviewed.

6.2.2 Fluid moment models for non-LTE plasmas

The complexity of the 6D Boltzmann system can be reduced by taking velocity moments of the Boltzmann equation,

$$\int Q_\alpha^i \left(\frac{\partial f_\alpha}{\partial_t} + \boldsymbol{v} \cdot \nabla_x f_\alpha + \frac{q_\alpha}{m_\alpha} (\boldsymbol{E} + \boldsymbol{v} \times \boldsymbol{B}) \cdot \nabla_v f_\alpha \right) d\boldsymbol{v} = \int Q_\alpha^i \left. \frac{\partial f_\alpha}{\partial t} \right|_c d\boldsymbol{v} \tag{6.6}$$

producing an infinite set of equations for the evolution of moment variables. When $Q^i \propto \boldsymbol{v}^i$, the moment variables take on familiar macroscopic quantities

$$0^{th} \text{ moment:} \quad n_\alpha = \int_v f_\alpha d\boldsymbol{v}, \tag{6.7}$$

$$1^{st} \text{ moment:} \quad \boldsymbol{u}_\alpha = \frac{1}{n_\alpha} \int_v \boldsymbol{v} f_\alpha d\boldsymbol{v}, \tag{6.8}$$

$$2^{nd} \text{moment:} \quad \Pi_\alpha = \frac{m_\alpha}{2} \int_v \boldsymbol{w}\boldsymbol{w} f_\alpha d\boldsymbol{v}, \text{ where } \boldsymbol{w} = \boldsymbol{v} - \boldsymbol{u}_\alpha \tag{6.9}$$

$$3^{rd} \text{moment:} \quad \boldsymbol{h}_\alpha = \int_v \boldsymbol{w} w^2 f_\alpha d\boldsymbol{v}, \quad \ldots \tag{6.10}$$

Each moment equation is dependent on the next highest moment variable, and collision operators are still dependent on the full distribution function.

Various assumptions can be made about the distribution function to truncate the moments and simplify the collision operators. A common approach in non-LTE low temperature plasmas takes the first two or three moments and closes the electron moment equations with values calculated by solving a simplified version of the Boltzmann equation (discussed in more detail later in this section). Heavy species moment equations are closed using common

fluid assumptions. The equation set in its most general form evolves continuity, momentum, and energy for each species α, summarized from Alves *et al.*[84] below

$$\frac{\partial n_\alpha}{\partial t} + \nabla \cdot n_\alpha \boldsymbol{v}_\alpha = S_\alpha, \tag{6.11}$$

$$\frac{n_\alpha}{\nu_\alpha}\frac{\partial \boldsymbol{v}_\alpha}{\partial t} + \frac{n_\alpha}{\nu_\alpha}(\boldsymbol{v}_\alpha \cdot \nabla)\boldsymbol{v}_\alpha \mp n_\alpha \mu_\alpha \boldsymbol{E} + D_\alpha \nabla n_\alpha = -\left(n_\alpha + \frac{S_\alpha}{\nu_\alpha}\right)\boldsymbol{v}_\alpha, \tag{6.12}$$

$$\frac{\partial}{\partial t}(n_\alpha \varepsilon_\alpha) + \nabla \cdot [\pm n_\alpha \varepsilon_\alpha \mu_{\varepsilon\alpha} \boldsymbol{E} - D_{\varepsilon\alpha}\nabla(\varepsilon_\alpha n_\alpha)] \mp e\boldsymbol{E} \cdot n_\alpha \boldsymbol{v}_\alpha + \Theta_\alpha = 0, \tag{6.13}$$

where $\mp$ and $\pm$ signs depend on particle charge. The following parameters are calculated by an external Boltzmann solver: the total partical source S_α, the effective momentum transfer frequency ν_α, the particle mobility μ_α and energy mobility $\mu_{\varepsilon\alpha}$, the particle diffusion D_α and energy diffusion $D_{\varepsilon\alpha}$, and the collisional power loss Θ_α. The system is coupled with Poisson or Maxwell's equations to evolve $\boldsymbol{E}$.

Electron Boltzmann equation (EBE) solvers

Electron Boltzmann equation (EBE) solvers are 0D models that reduce the complexity of solving the complete Boltzmann equation by expanding the electron energy distribution on some set of functions, and then assuming Maxwellian velocity distribution functions for all heavy species. The two most common expansions are Legendre polynomials and powers of spatial gradients of the electron density. In this section the Legendre polynomial expansion method will be explored, as it is the method employed by several popular open-source EBE solver projects. The reader is referred to the following references for more detail on density gradient expansion methods[85, 86].

Legendre polynomial $P_l(\cos\theta)$ expansions approximate the electron distribution function (EDF) as

$$f(\boldsymbol{v}, z, t) = \sum_{l=0}^{\infty} f_l(z, v, t) P_l(\cos\theta), \tag{6.14}$$

where θ denotes either the angle to the dominant drift velocity or the background electric field. In the presence of alternating fields, the temporal component of the EDF may also be expanded in a Fourier series in time[87]

$$f(\boldsymbol{v}, z, t) = \sum_{l=0}^{\infty} \sum_{k=\infty}^{\infty} f_{lk}(z, v, t) P_l(\cos\theta) e^{ik\omega t}. \tag{6.15}$$

Bolsig+[17] is a popular open-source EBE solver that uses a two-term expansion in Legendre polynomials of the distribution function for DC fields

$$f(v, \cos\theta, z, t) = f_0(v, z, t) + f_1(v, z, t) cos\theta, \tag{6.16}$$

where f_0 is isotropic, and f_1 is an anisotropic perturbation. Substituting the expansion for f into the Boltzmann equation, and integrating over $\cos\theta$ results in equations for the evolution of f_0 and f_1

$$\frac{\partial f_0}{\partial t} + \frac{\gamma}{3}\varepsilon^{1/2}\frac{\partial f_1}{\partial z} - \frac{\gamma}{3}\varepsilon^{1/2}\frac{\partial}{\partial \varepsilon}(\varepsilon E f_1) = C_0 \tag{6.17}$$

$$\frac{\partial f_1}{\partial t} + \gamma\varepsilon^{1/2}\frac{\partial f_0}{\partial z} - E\gamma\varepsilon^{1/2}\frac{\partial f_0}{\partial \varepsilon} = C_1 - N\sigma_m\gamma\varepsilon^{1/2} f_1 \tag{6.18}$$

where $\gamma = (2e/m)^{1/2}$ is a constant and $\varepsilon = (v/\gamma)^2$ is the electron energy in electron volts, C_0 is the collection of collision and reaction source terms for the isotropic part, C_1 is the same for the anisotropic part, and $\sigma_m = \sum_\alpha x_\alpha \sigma_\alpha$ is the total momentum-transfer cross section. A further assumption is made in order to separate the dependence on time and space from the dependence on energy,

$$f_{0,1}(\varepsilon, z, t) = \frac{1}{2\pi\gamma^3} F_{0,1}(\varepsilon) n(z, t), \tag{6.19}$$

and $F_{0,1}$ is normalized by

$$\int_0^\infty \varepsilon^{1/2} F_0 d\varepsilon = 1. \tag{6.20}$$

The anisotropic part carries the drift velocity such that

$$w = \frac{\gamma}{3}\int_0^\infty \varepsilon F_1 d\varepsilon. \tag{6.21}$$

In the case of constant in space, exponential growth in time, with non-zero Coulomb collisions, the combined system is nonlinear with respect to integrals over the distribution functions $F_{0,1}$ and must be solved iteratively[88]

$$-\frac{\gamma}{3}\frac{\partial}{\partial\varepsilon}\left(\left(\frac{eE}{N}\right)^2\frac{\chi\varepsilon}{\tilde{\sigma}_m}\frac{\partial F_0^{j+1}}{\partial\varepsilon}\right)=\frac{1}{N}\varepsilon^{1/2}\left(C_0^{ee}[F_0^j,F_0^{j+1}]+\tilde{C}_0[F_0^{j+1}]\right)+\tilde{R}, \tag{6.22}$$

where

$$\chi=\frac{N\sigma_m F_1^{j+1}}{E(\partial F_0^j/\partial\varepsilon)} \tag{6.23}$$

is a correction factor to account for the effect of electron-electron Coulomb collisions on F_1 and

$$\tilde{R}=-\frac{\bar{\nu}_i}{N}\varepsilon^{1/2}F_0 \tag{6.24}$$

is a function of the production frequency $\bar{\nu}_i$ and is used to maintain normalization of F_0 despite a changing n_e . All other elastic and inelastic collisions are incorporated into $\tilde{C}_0$

$$\tilde{C}_0=2\pi\gamma^3\varepsilon^{1/2}\frac{C_0}{Nn_e}. \tag{6.25}$$

Due to the fact that the collision term C_0 has been divided by the gas and electron densities, N and n respectively, makes the term relatively independent of density. Expressions for all collisions are summarized in Appendix C, and are all functions of experimentally derived collision cross sections σ_k. Databases of cross sections have been compiled for use with EBEs for a wide variety of atomic and molecular species in the LXCat database[89, 90].

Transport coefficients and reaction rates are calculated from moments of the EEDF solutions of the EBE solver. Transport coefficients for mobility

$$\mu N=-\frac{\gamma}{3}\int_0^\infty\frac{\varepsilon}{\tilde{\sigma}_m}\frac{\partial F_0}{\partial\varepsilon}d\varepsilon, \tag{6.26}$$

and diffusion

$$DN=\frac{\gamma}{3}\int_0^\infty\frac{\varepsilon}{\tilde{\sigma}_m}F_0 d\varepsilon, \tag{6.27}$$

where $\tilde{\sigma}_m$ is an effective momentum-transfer cross section that includes momentum effects due to temporal electron growth. The mean energy is

$$\tilde{\varepsilon} = \int_0^\infty \varepsilon^{3/2} F_0 d\varepsilon. \tag{6.28}$$

Reaction rates for a given process k are defined as

$$R_k = k_k x_k N n, \quad \text{where} \quad k_k = \gamma \int_0^\infty \varepsilon \sigma_k F_0 d\varepsilon \tag{6.29}$$

is the reaction coefficient and x_k is the mole fraction of the target species.

While EBE solvers are an efficient way to solve the Boltzmann equation, using an EBE solver to calculate transport and reaction rates for a fluid model has drawbacks. First, the EBE solver is typically run in advance to generate look-up tables, therefore values can only be a function of, at most, two variables. If ionization fraction or spatial gradients change over the duration of the fluid simulation, the EBE solver would need to be rerun. Second, common EBE solvers like Bolsig+, are targeted to low ionization fraction plasmas and are slow to converge, or fail to converge completely, at high ionization fractions.

If further simplifying assumptions can be made about the electron distribution function, both transport and reaction calculations become functions of macroscopic quantities and the system becomes self contained.

6.2.3 5N-Moment models for reacting plasma-neutral mixtures

The moment model truncation problem presented in Sec. 6.2.2 can be solved in certain cases by assuming that the particle distribution functions are Maxwellian, or nearly Maxwellian. The Meier and Shumlak reacting three-fluid 5-moment model[15] separates the truncation problem into two parts.

As the left hand side of the Boltzmann equation involves transport, closures for pressure Π, heat flux $\boldsymbol{h}$ tensors, and momentum exchange can be chosen based on the Knudsen

number of the problem. Closures for magnetized and un-magnetized plasmas are already well established (i.e. Braginskii).

The reactions on the RHS, especially ionization, are dependent on the presence or absence of LTE, which is established through the Griem criteria established earlier. The Meier and Shumlak model as initially proposed assumes LTE and a stationary Maxwellian distribution function, which allows for analytical calculation of collision integrals, or allows for the use of established fit functions reaction rates as a function of T_e alone.

The full system becomes a set of five equations for each of three species (electrons, ions, and neutral atoms), transcribed below for reference.

Continuity:

$$\frac{\partial n_e}{\partial t} + \nabla \cdot (n_e \boldsymbol{v}_e) = \Gamma_i^{ion} - \Gamma_n^{rec} \tag{6.30}$$

$$\frac{\partial n_i}{\partial t} + \nabla \cdot (n_i \boldsymbol{v}_i) = \Gamma_i^{ion} - \Gamma_n^{rec} \tag{6.31}$$

$$\frac{\partial n_n}{\partial t} + \nabla \cdot (n_n \boldsymbol{v}_n) = \Gamma_n^{rec} - \Gamma_i^{ion} \tag{6.32}$$

where $\Gamma_i^{ion} = n_e n_n \langle \sigma v \rangle_{ion}$ and $\Gamma_n^{rec} = n_e n_e \langle \sigma v \rangle_{rec}$ are the ionization and recombination sources.

Momentum:

$$\frac{\partial}{\partial t}(m_e n_e \boldsymbol{v}_e) + \nabla \cdot (m_e n_e \boldsymbol{v}_e \boldsymbol{v}_e + \mathbb{P}_e) = \tag{6.33}$$
$$q_e n_e (\boldsymbol{E} + \boldsymbol{v}_e \times \boldsymbol{B}) + \boldsymbol{R}_i^{ie} - \boldsymbol{R}_e^{en} + \Gamma_i^{ion} m_e \boldsymbol{v}_n - \Gamma_n^{rec} m_e \boldsymbol{v}_e$$

$$\frac{\partial}{\partial t}(m_i n_i \boldsymbol{v}_i) + \nabla \cdot (m_i n_i \boldsymbol{v}_i \boldsymbol{v}_i + \mathbb{P}_i) = \tag{6.34}$$
$$q_i n_i (\boldsymbol{E} + \boldsymbol{v}_i \times \boldsymbol{B}) + \boldsymbol{R}_i^{ie} + \boldsymbol{R}_i^{in} + \Gamma_i^{ion} m_i \boldsymbol{v}_n - \Gamma_n^{rec} m_i \boldsymbol{v}_i + \Gamma^{cx} m_i (\boldsymbol{v}_n - \boldsymbol{v}_i) + \boldsymbol{R}_{in}^{cx} - \boldsymbol{R}_{ni}^{cx}$$

$$\frac{\partial}{\partial t}(m_n n_n \boldsymbol{v}_n) + \nabla \cdot (m_n n_n \boldsymbol{v}_n \boldsymbol{v}_n + \mathbb{P}_n) = \tag{6.35}$$
$$- \boldsymbol{R}_i^{in} - \boldsymbol{R}_e^{en} + \Gamma_n^{rec} (m_e \boldsymbol{v}_e + m_i \boldsymbol{v}_i) - \Gamma_i^{ion} m_n \boldsymbol{v}_n + \Gamma^{cx} m_i (\boldsymbol{v}_n - \boldsymbol{v}_i) + \boldsymbol{R}_{in}^{cx} - \boldsymbol{R}_{ni}^{cx}$$

where $\mathbb{P}_\alpha = P_\alpha \boldsymbol{I} + \boldsymbol{\Pi}_\alpha$ is the pressure tensor, $\boldsymbol{\Pi}_\alpha = -\xi(\nabla \boldsymbol{v} + (\nabla \boldsymbol{v})^T)$ is the stress tensor,

and $\boldsymbol{R}_\alpha^{\alpha\beta} = m_\alpha n_\alpha \nu_{\alpha\beta}(\boldsymbol{v}_\alpha - \boldsymbol{v}_\beta)$ are the elastic scattering collision friction terms.

Energy:

$$\frac{\partial \varepsilon_e}{\partial t} + \nabla \cdot (\varepsilon_e \boldsymbol{v}_e + \boldsymbol{v}_e \cdot \mathbb{P}_e + \boldsymbol{h}_e) = \tag{6.36}$$
$$\boldsymbol{v}_e \cdot \left(-q_e n_e \boldsymbol{E} - \boldsymbol{R}_i^{ie} + \boldsymbol{R}_e^{en}\right) + Q_e^{ie} + Q_e^{en} + \frac{m_e}{m_n}\left(\Gamma_i^{ion}\frac{1}{2}m_n v_n^2 + Q_n^{ion}\right)$$
$$- \Gamma_i^{ion}\phi_{ion} - \Gamma_n^{rec}\frac{1}{2}m_e v_e^2 - Q_e^{rec}$$

$$\frac{\partial \varepsilon_i}{\partial t} + \nabla \cdot (\varepsilon_i \boldsymbol{v}_i + \boldsymbol{v}_i \cdot \mathbb{P}_i + \boldsymbol{h}_i) = \tag{6.37}$$
$$\boldsymbol{v}_i \cdot \left(q_i n_i \boldsymbol{E} + \boldsymbol{R}_i^{ie} + \boldsymbol{R}_i^{in}\right) + Q_i^{ie} + Q_i^{in} + \frac{m_i}{m_n}\left(\Gamma_i^{ion}\frac{1}{2}m_n v_n^2 + Q_n^{ion}\right)$$
$$- \Gamma_n^{rec}\frac{1}{2}m_i v_i^2 - Q_i^{rec} + \Gamma^{cx}\frac{1}{2}m_i\left(v_n^2 - v_i^2\right) + \boldsymbol{v}_n \cdot \boldsymbol{R}_{in}^{cx} - \boldsymbol{v}_i \cdot \boldsymbol{R}_{ni}^{cx} + Q_{in}^{cx} - Q_{ni}^{cx}$$

$$\frac{\partial \varepsilon_n}{\partial t} + \nabla \cdot (\varepsilon_n \boldsymbol{v}_n + \boldsymbol{v}_n \cdot \mathbb{P}_n + \boldsymbol{h}_n) = \tag{6.38}$$
$$- \boldsymbol{v}_n \cdot \left(\boldsymbol{R}_e^{en} + \boldsymbol{R}_i^{in}\right) + Q_n^{in} + Q_n^{en} - \left(\Gamma_i^{ion}\frac{1}{2}m_n v_n^2 + Q_n^{ion}\right)$$
$$+ \Gamma_n^{rec}\left(\frac{1}{2}m_i v_i^2 + \frac{1}{2}m_e v_e^2\right) + Q_i^{rec} + Q_e^{rec} + \Gamma^{cx}\frac{1}{2}m_i\left(v_i^2 - v_n^2\right) + \boldsymbol{v}_i \cdot \boldsymbol{R}_{ni}^{cx} - \boldsymbol{v}_n \cdot \boldsymbol{R}_{in}^{cx} + Q_{ni}^{cx} - Q_{in}^{cx}$$

where

$$\varepsilon_\alpha = \frac{1}{\gamma - 1}P_\alpha + \frac{1}{2}m_\alpha n_\alpha u_\alpha^2 \tag{6.39}$$

and $\boldsymbol{h}_\alpha$ is the heat flux, $Q_\alpha^{\alpha\beta} = -\frac{2}{3}n_\alpha \nu_{\alpha\beta}\frac{m_\alpha}{m_\alpha + m_\beta}\left(3(T_\alpha - T_\beta) - m_\beta(\boldsymbol{v}_\alpha - \boldsymbol{v}_\beta)^2\right)$ capture collisional heat exchange, $Q_n^{ion} \equiv \Gamma_i^{ion}\frac{3}{2}kT_n$, $Q_i^{rec} \equiv \Gamma_n^{rec}\frac{3}{2}kT_i$, and $Q_e^{rec} \approx \Gamma_n^{rec}\frac{3}{2}kT_e$ are the heating terms associated with ionization and recombination, and ϕ_{ion} is the average energy loss per ionization.

A gap currently exists in the modeling of high density partially ionized plasmas between fluid models relying on assuming LTE and Maxwellian distribution functions, and models with EBE solvers that involve model overhead and assume low ionization fractions. In the next section, a model is proposed that extends the Meier and Shumlak reacting 5-moment model into the partial-LTE region for modeling THz and other high density, partially ionized plasmas.

6.3 Proposed modeling approach: high-fidelity reacting multi-fluid 5-moment model with correction factors for non-LTE plasmas

Finding appropriate correction factors for non-LTE requires understanding the impact of non-LTE electron distribution functions on electron-neutral and electron-ion interactions. In this section, approximations for various interaction frequencies are proposed based on observed effects of degree of ionization and Coulomb collisions on partially ionized argon plasmas by Hagelaar[91]. These approximations will then be compared to Bolsig+ EBE solver results for a range of ionization fractions.

6.3.1 Electron-electron Coulomb collisions

Electron-electron Coulomb collisions are the major driver of LTE by repopulating electron energies where electrons are lost to exciting or ionizing collisions. In Figure 6.6 electron distribution functions in a marginally LTE plasma are compared for cases with and without electron-electron collisions. The electron distribution without e-e collisions is highly non-Maxwellian (a Maxwellian distribution will have constant slope on a logarithmic axis), with a non-existent high-energy tail. As expected, e-e collisions thermalize the distribution and repopulate the tail.

Interaction rates needed for fluid models are found by integrating over the cross section multiplied by the electron distribution function. Assuming thermal heavy particle β with $T_\beta \leq T_e$

$$\Gamma_{e\beta} \approx n_e n_\beta \left\langle \sigma_{e\beta} \varepsilon \right\rangle = n_e n_\beta \int_0^\infty \sigma_{e\beta}(\varepsilon) F_e(\varepsilon) d\varepsilon \tag{6.40}$$

where $\sigma_{\alpha\beta}$ is the interaction cross section as a function of the difference in energy between electron and particle populations, and F_e is the normalized distribution function such that $\int F d\varepsilon = 1$. As can be seen in Fig. 6.6, the overlap of the electron distribution function and all cross sections changes significantly without and with e-e collisions, resulting in different macroscopic rates. In the case of excitation and ionization rates, without e-e collisions both

are zero, and with e-e collisions both will have finite values. Reaction rate estimations that assume Maxwellian distributions for electrons, like those used in the original Meier and Shumlak reacting 5-moment model, would significantly over predict ionization rates. In the following sections the severity of this impact is evaluated and corrections proposed for some reactions.

6.3.2 Electron-neutral momentum transfer frequency

The electron-neutral momentum transfer cross section is a complex function of electron energy. Fit functions have been formulated by McEachran and Strauffer[92] to facilitate the calculation of collision integrals (plotted in Fig. 6.5 against cross sections calculated with Fortran program, MAGBOLTZ v8.97, S.F. Biagi database, www.lxcat.net, retrieved on December 26, 2022[89, 90]).

Conveniently, the electron-neutral collision frequency ν_{en} can be well approximated by assuming a constant cross section, as will be shown in Sec. 6.4. Therefore in calculations used in this work the following approximation will be used

$$\nu_{en} = \Gamma_{en}/n_e = n_n \langle \sigma_{en} v \rangle \approx n_e \sigma_{en} v_{Te}, \quad \mathrm{s}^{-1} \tag{6.41}$$

where $\sigma_{ne} \approx 10^{-19}$ m^2.

6.3.3 Electron-ion momentum transfer frequency

For low ionization fraction plasmas, electron-neutral interactions dominate momentum exchange. As the ionization fraction increases and electron-ion interactions become dominant, the Hagelaar study of Coulomb collisions found that momentum transfer frequency agrees well with the Spitzer-Härm plasma resistivity model for completely ionized gases[93]. Due to the nature of Coulomb collisions, the resistivity decreases with increasing temperature, and the high energy tail of the distribution has a reduced impact.

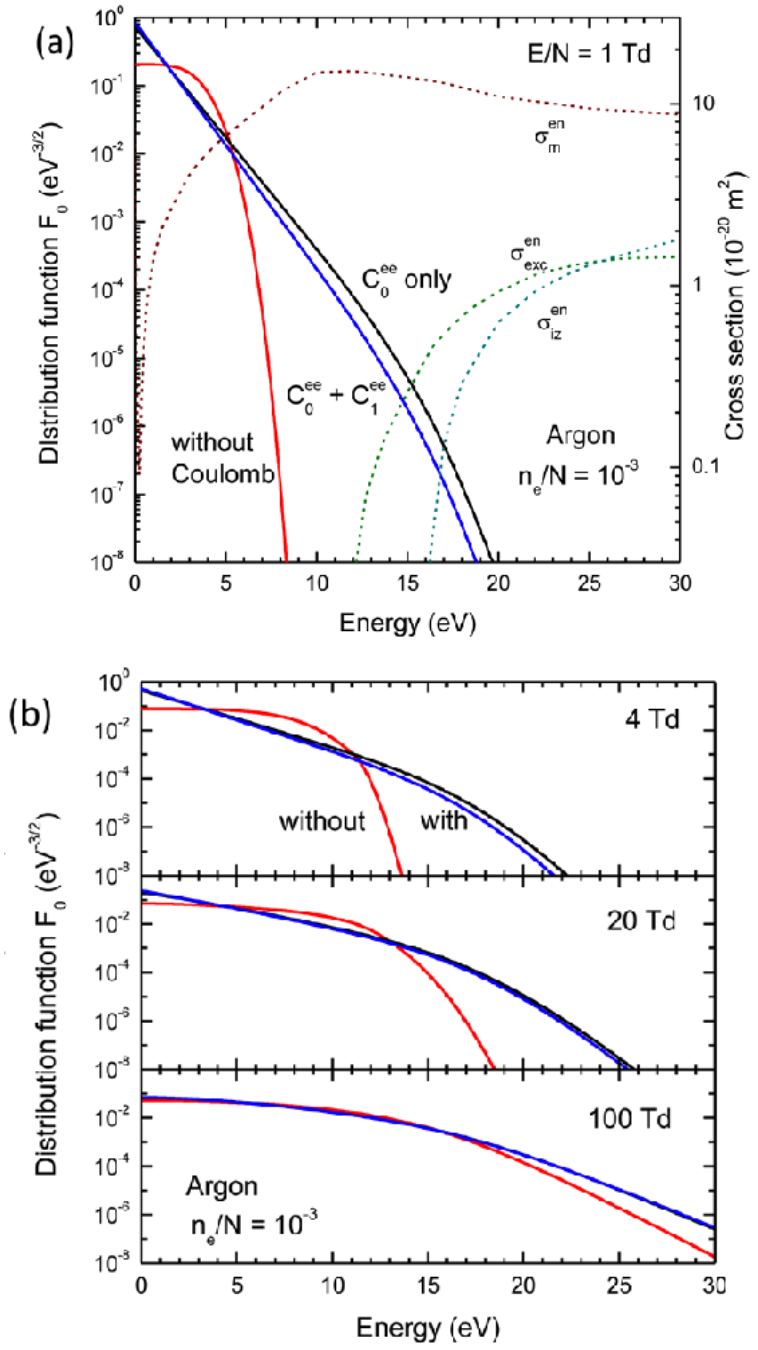

Figure 6.4: Electron-electron collision frequency drives electron distribution functions towards a Maxwellian. In the figure above, electron distribution functions with and without electron-electron Coulomb collisions for reduced electric fields $E/N = 1$ Td (a) and $E/N =$ 4, 20, and 100 Td (b). Electron-neutral cross sections are plotted against the distribution in panel (a) (dashed lines, right axis) for reference[91].

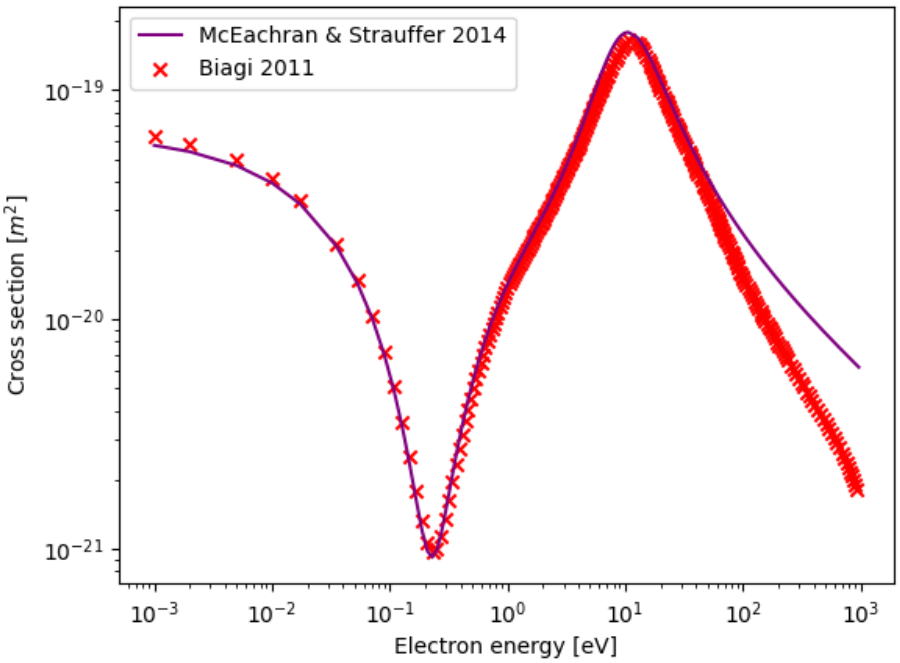

Figure 6.5: Despite the fact that electron-neutral momentum transfer cross sections in argon are a complex function of electron energy, reasonable collision frequency can be calculated assuming a constant cross section $\sigma_{ion} \approx 10^{-19}$. Cross sections generated by the Fortran program, MAGBOLTZ v8.97, S.F. Biagi database, www.lxcat.net, retrieved on December 26, 2022[89, 90] (red Xs), and a fit function formulated by McEachran and Strauffer[92].

For this study, in the absence of temperature or density gradients, e-i collision frequency is assumed to be reasonably approximated by the interaction of Maxwellian distributions[94]

$$\nu_{ei} \approx 6.09 \times 10^{19} \frac{n_i Z_i^2 e^4 \ln(\Lambda_e)(1 + m_e/m_i)}{\left(2T_e/m_e + 2T_i/m_i\right)^{3/2}}, \quad \mathrm{s}^{-1} \tag{6.42}$$

where Z_i is the degree of ionization.

6.3.4 Attachment frequency

The attachment cross section of argon is small for all electron energies. As there is little documentation of experimental attachment cross sections for argon in the literature, this work borrows the assumption of only radiative recombination from Meier *et al.* and uses the relation proposed by Annaloro *et al.*[95] that has reasonable agreement with experimental and calculated data

$$\Gamma^{rec} = n_e n_i \left\langle \sigma v \right\rangle_{rec} = n_e n_i A_r (T_e')^{\alpha_r} e^{-T_r/T_e'}, \quad \mathrm{m}^{-3}\mathrm{s}^{-1} \tag{6.43}$$

with T_e in degrees Kelvin, and values of $A_r = 9.41 \times 10^{-44}$, $\alpha_r = 0.368$, and $T_r = -45430$ for argon.

6.3.5 Ionization frequency

As was shown in Fig. 6.6, the degree of LTE has a strong impact on ionization rates, due to the fact that ionization cross sections are zero below the ionization threshold energy (for argon $E_{ion} = 15.6$ eV). For cool plasmas with mean energies below the threshold energy, the ionization rate is entirely dependent on the population of the high energy tail above the threshold energy. In non-LTE plasmas, this tail is severely depleted, and much higher mean temperatures are required to achieve a finite ionization rate. In Figure 6.6, the ionization frequency for plasmas with different ionization fractions (and therefore different Gr numbers) are compared, as calculated by Bolsig+.

As the mean energy of the plasma approaches the threshold energy, the ionization rate of both LTE and non-LTE plasmas converge. This indicates that any proposed correction must approach the LTE solution at both high temperature and low Gr number.

In this section, four approximations for the ionization rate are proposed. The first assumes a stationary Maxwellian distribution function and is the current model used in the Meier and Shumlak reacting 5-moment model. Each subsequent model includes additional physics, in order to better approximate the true solution.

Stationary Maxwellian electron distribution approximation (SMA)

The first model is a fit function for ionization rates assuming a stationary Maxwellian distribution distribution

$$\Gamma^{ion} = n_i n_e \langle \sigma v \rangle_{ion}, \quad \text{where} \quad \langle \sigma v \rangle_{ion} \approx A \frac{1 + PU^{1/2}}{X + U} U^K e^{-U}, \quad \text{m}^{-3}\text{s}^{-1} \tag{6.44}$$

where A, P, X, and K are coefficients are tabulated in [96] for the first 28 elements, $U = E_{ion}/kT_e$, and E_{ion} is the ionization energy

Effective temperature approximation (ETA)

In both DC and AC discharges, electron drift velocities are finite. When the gas is cold, the ratio of the kinetic to thermal energy may be large, and the mean energy and temperature of the distribution will no longer be similar. This second approximation incorporate a non-finite kinetic energy by using a modified effective temperature T_e', where $kT_e' = kT_e + \frac{1}{2} m_e v_e^2$. The effective temperature can then be used in the analytical reaction rate fit function used in the SMA.

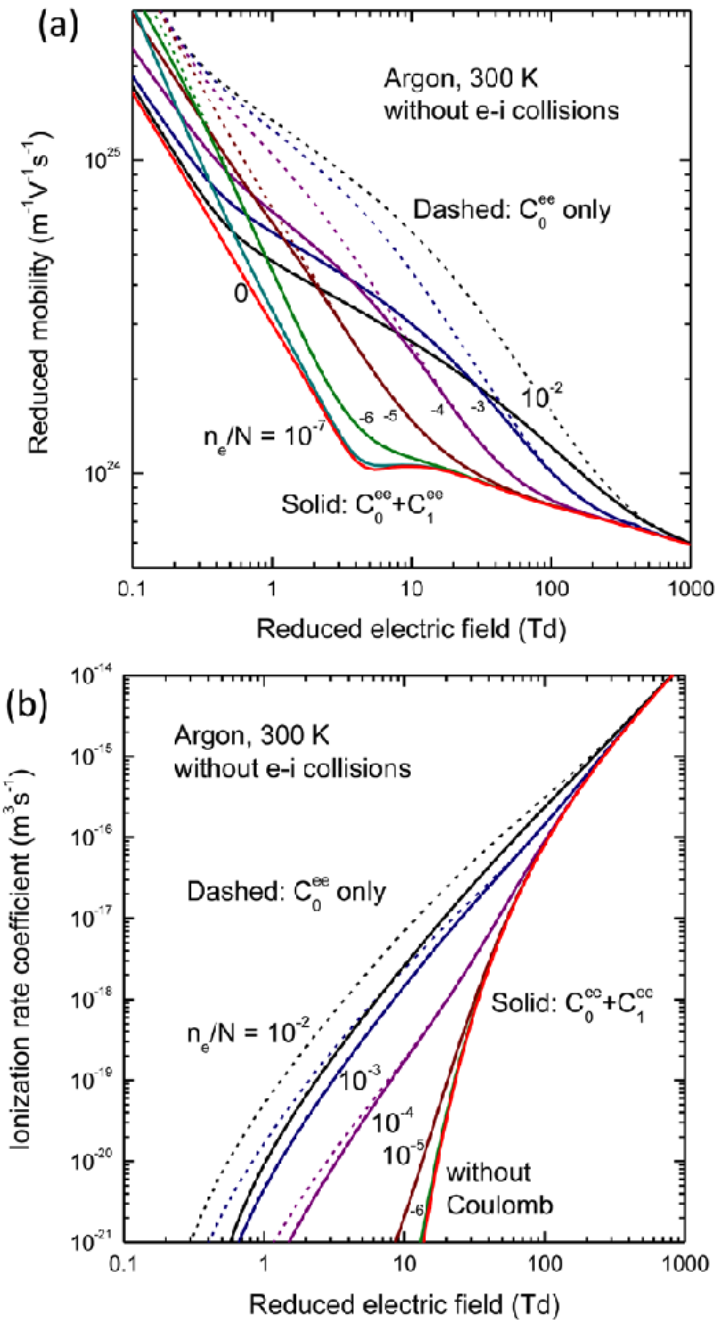

Figure 6.6: Ionization fraction (a proxy for electron density) has significant impact on electron mobility and ionization rates. In this figure, electron distribution functions with and without electron-electron Coulomb collisions for reduced electric fields $E/N = 1$ Td (a) and $E/N = 4$, 20, and 100 Td (b). Electron-neutral cross sections are plot against the distribution in panel (a) (dashed lines, right axis)[91]

Drifting finite temperature approximation (DFTA)

The drifting finite temperature approximation (DFTA) evaluates the collision integral assuming a drifting Maxwellian electron distribution

$$\Gamma^{ion} = \int f_n(\boldsymbol{v}') \int f_e(\boldsymbol{v}) \sigma_{ion}(v_{rel}) v_{rel} d\boldsymbol{v} d\boldsymbol{v}'. \tag{6.45}$$

Given that electron drift velocity $v_e \gg v_{Tn} \gg v_n$, the integral reduces to

$$\Gamma^{ion} \approx n_n n_e \int_0^\infty \sigma_{ion}(v) \frac{v^2}{\sqrt{\pi} u_e v_{Te}} \left(\exp\left[-\frac{(v-u_e)^2}{v_{Te}^2} \right] - \exp\left[-\frac{(v+u_e)^2}{v_{Te}^2} \right] \right) dv \tag{6.46}$$

where $\sigma_{ion}(v)$ is the total ionization cross section. In this work an empirical fit function adapted from work by Hombourger[97] for K-shell ionization cross section

$$\sigma_k = n_k \pi a_0^2 G_r \left(\frac{Ry}{E_k} \right)^{C_U} D_U \tag{6.47}$$

where n_k is the number of electrons in the K shell, a_0 is the first Bohr radius, Ry is the Rydberg constant, G_r is the Gryziński relativistic factor[98, 99] (not to be confused with Griem number Gr), E_k is the ionization threshold energy, D_U is the reduced cross section and C_U is an exponent that is a function of U, the excess energy electron (ε_e / E_k).

The reduced cross section is fit to the following expression

$$D_U = \left(a + \frac{b}{U} + \frac{c}{U^2} \right) \frac{\ln U}{U}, \tag{6.48}$$

and the exponent C_U

$$C_U = \left(d + \frac{e}{U} + \frac{f}{U^2} \right). \tag{6.49}$$

Neglecting the relativistic factor G_r, and fitting the Hombourger expression to argon cross section data obtained through LXCat[89] from the S. F. Biagi Fortran program, MAGBOLTZ, the following values were found for the fit parameters using a Python Scipy curve fitting algorithm,

$$\begin{aligned} a = 1.1197, \quad b = -2.1964, \quad c = 1.0970 \\ d = -6.086, \quad e = 6.4349, \quad f = -22.1150 \end{aligned} \tag{6.50}$$

resulting in a total error of $< 2\%$ between 15.8 eV and 1 keV. The curve fit found above is plotted against one provided by Hombourger, and the Biagi LXCat data in Fig. 6.7.

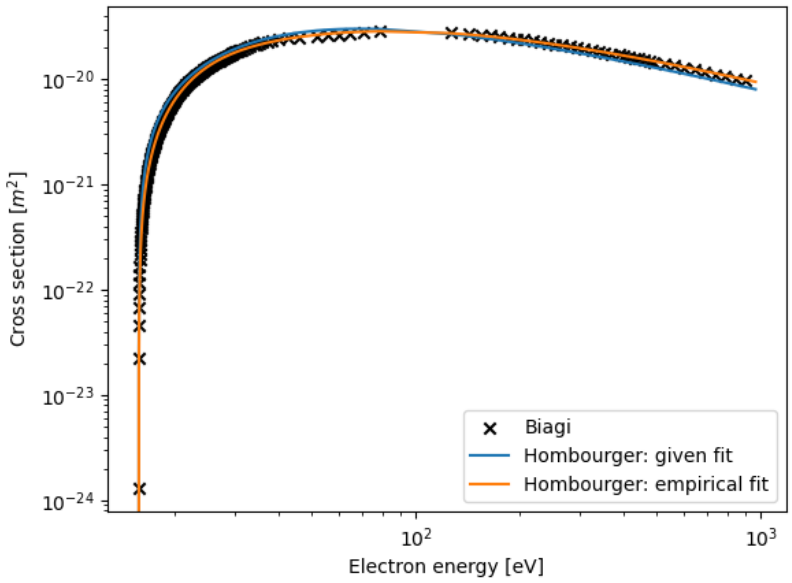

Figure 6.7: Electron impact total ionization cross sections calculated with Biagi Fortran code MAGBOLTZ via LXCat[89] (black x's), the Hombourger K-shell ionization fit function using coefficients calculated by Hombourger[97] (blue line), and the same fit function using empirically found coefficients listed in Eq. (6.50) (orange line).

DFTA with Gr and T_e dependent correction factor (DFTA+K_{Gr})

All previous models assume Maxwellian distribution functions, drifting or stationary. As was shown earlier in this section, in non-LTE plasmas this assumption can greatly over predict the ionization rate at temperatures below the ionization threshold energy. The DFTA+Gr model will start with the DFTA model, but multiply it by a correction factor K_{Gr} that is

function of both the Gr number and the ratio of the electron temperature to the lowest excitation energy $T_e/E_{exc,0}$. For this comparison, the function is simple and fit by eye

$$K_{Gr} = \min\left(A\mathrm{Gr}^{-B} + \exp\left(1 - [CE_{ext,0}/T_e]^D\right), 1\right) \tag{6.51}$$

where coefficients A, B, C, and D are determined by fitting to Bolsig+ data. In Figs. 6.8, 6.10, and 6.11 the coefficients for the K_{Gr} correction are $A = 2$, $B = 3/2$, $C = 2/5$, and $D = 4$. More complex functions and coefficients calculated through standardized means is the area of future work.

The four approximations are compared in Fig. 6.8 for several values of Gr. At low density $n_e = 10^{19}$ the DFTA+K_{Gr} ionization rate is significantly lower than the other three for $T_e < 5$ eV, even at zero drift velocity (top right). With increasing drift velocity, the ETA ionization rate becomes increasingly large. Surprisingly, despite the considerable difference in complexity of the SMA and DFTA methods, they remain relatively close for all velocities. This implies that for high density, LTE plasmas, the SMA method is a reasonable approximation. For non-LTE plasmas, the correction to the ionization rate of the DFTA+K_{Gr} is non-negligible and cannot be approximated by an LTE method like SMA or ETA. Furthermore, the complexity of the DFTA+K_{Gr} could be reduced by applying the correction factor to the SMA method instead.

In the next section, the collision and ionization rate approximation described in this section will be compared with those calculated by Bolsig+.

6.4 Validation of collision and reaction rate approximations for a 0D equilibrium in DC fields

In order to establish the validity of the approximations for collision and reaction rates proposed in the previous section, collision and power loss rates are compared with those calculated by Bolsig+ (see Sec. 6.2.2 for a discussion of the Bolsig+ model) for an atmospheric density argon gas ($n_t = n_i + n_n = 2.5 \times 10^{25}$) and $T_n = 0.025$ eV in a DC electric field.

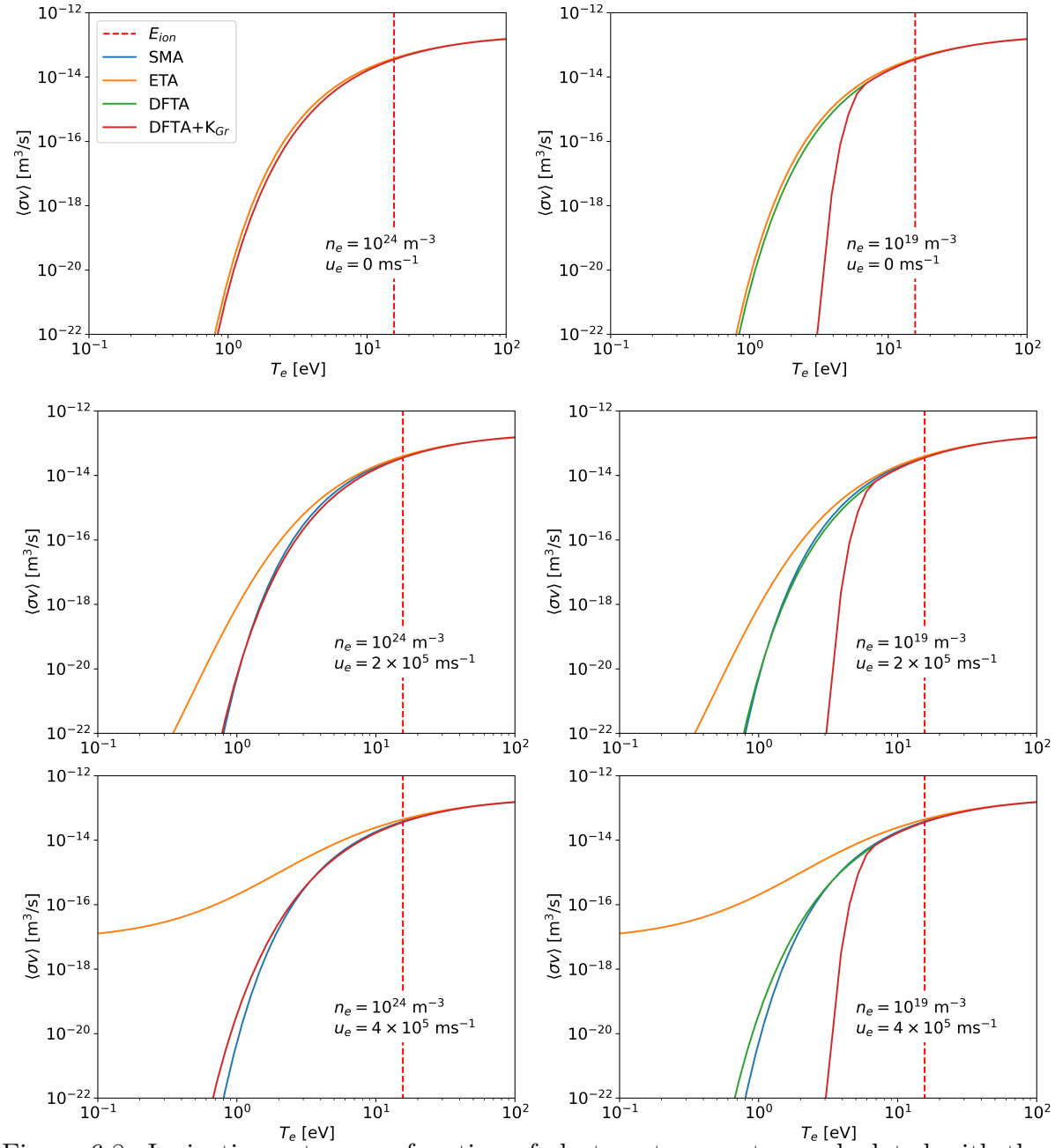

Figure 6.8: Ionization rates as a function of electron temperature calculated with the four approximations outlined in Sec. 6.3.5. Electron densities and drift velocities are indicated on each panel. At high electron density and zero drift velocity (top left) all methods give similar ionization rates. The ETA method (orange) is unreliable at even moderate drift velocities (middle panels $\epsilon_e = 0.5 m_e u_e \approx E_{ion}/100$, lower panels $\epsilon_e = 0.5 m_e u_e \approx E_{ion}/50$). Surprisingly, the SMA method (blue) proves to be a reasonable approximation, despite it's simplicity, until $\epsilon_e = 0.5 m_e u_e \approx E_{ion}/10$ (not shown). At low density $n_e = 10^{19}$ (right panels), Gr > 1 and the plasma is no longer in LTE, and the DFTA+K_{Gr} ionization rate departs significantly from the other three for $T_e < 5$ eV, even at zero drift velocity (top right). For non-LTE plasmas, the correction to the ionization rate of the DFTA+K_{Gr} is non-negligible and cannot be approximated by an LTE method.

Mean energies and drift velocities used to calculate rates use the Bolsig+ values in order to provide a direct comparison.

6.4.1 Momentum transfer frequency

In Fig. 6.9 drift velocity, collision frequencies, and power transfer rates are calculated for the proposed model and compared with Bolsig+ calculated values for an argon gas with $n_g = 10^{19}$ m^{-3} and a low ionization fraction 10^{-6} such that electron-neutral collisions dominate and LTE cannot be assumed. The same equilibrium temperatures and drift velocities are used in both cases.

Despite the fact that the e-n collision cross section is such a strong function of energy, assuming a constant cross section follows the Bolsig+ calculated collision frequency reasonably well, and only the low temperature end seems to dependent on the ionization fraction. Considering the minimum in the cross section that occurs around 0.2 eV, a collision frequency sensitive to the density of high energy tail makes sense. Improved fits that take this into account would improve the accuracy at low and high temperatures.

The estimated e-i collision frequency approximates the Bolsig+ calculated values to within much less than an order of magnitude for all ionization fractions. For both types of elastic collisions, the agreement is largely satisfactory considering the reduction in complexity afforded by the approximations over using an EBE solver.

6.4.2 Ionization frequency

The ionization frequency is the strongest function of LTE, and where the approximate models and the EBE solver are expected to deviate the most. In Fig. 6.10 the ionization rates predicted by the DFTA+K_{Gr} approximation are compared to those calculated by Bolsig+. Again, the same equilibrium mean energy and drift velocities are used in both cases.

The selection of correction factor coefficients was not rigorous, but chosen so that the ap-

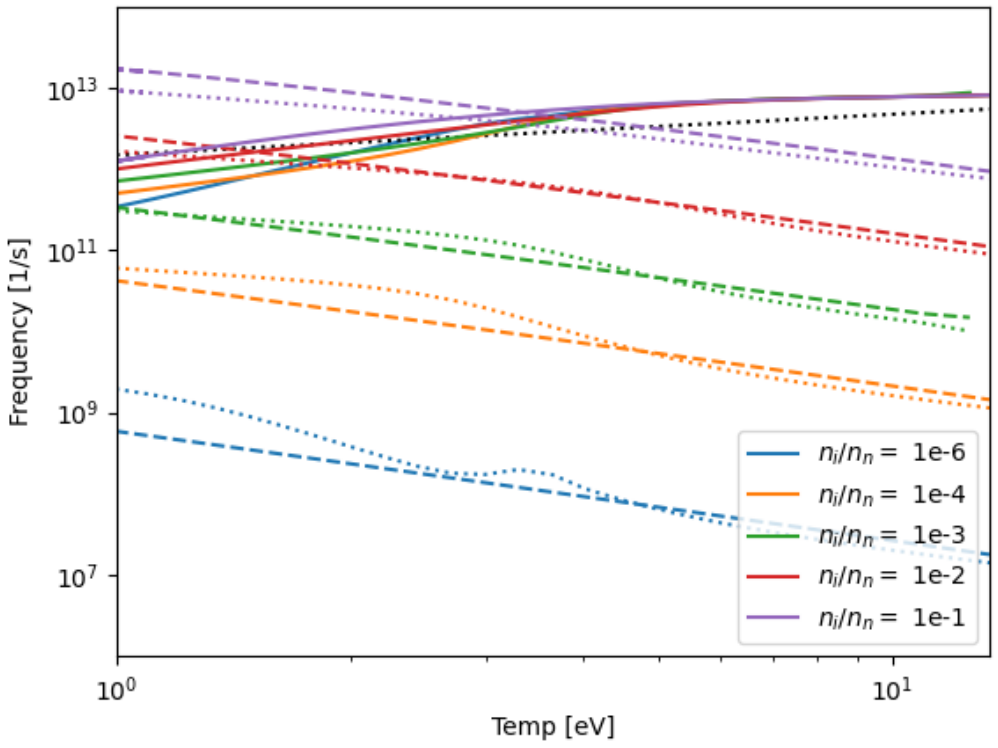

Figure 6.9: Electron-neutral momentum transfer frequency calculated with Bolsig+ (colors solid) and with a constant cross section (black dotted), and electron-ion collision frequencies calculated with Bolsig+ (dashed) and the Hinton (colors dotted). All calculations use Bolsig+ calculated drift velocities and temperatures. For both types of elastic collisions, the agreement is largely satisfactory considering the reduction in complexity afforded by the approximations over using an EBE solver.

proximated values reflected major characteristics. Considering the simplicity of the function, the general trends in both ionization fraction and temperature are consistent, and reduce the absolute difference in frequencies by up to six orders of magnitude in some cases. For reference, the DFTA without the correction factor would follow the purple dash dotted line.

6.4.3 Power loss rates

The accuracy of power gain and loss rates will determine the accuracy of calculated equilibrium temperatures. Equilibrium temperatures that depart significantly from expected temperatures will in turn impact collision and reaction rates, which will effect power loss rates, etc. It is therefore important that deviations in collision frequencies are small enough so as to not impact power loss significantly. In Fig. 6.11, the inelastic and elastic power loss rates are compared for both methods, at several ionization fractions. While there is general agreement, the low temperatures see power loss rate deviations of up to an order of magnitude, consistent with the deviation in the e-n momentum transfer frequency. If deviations are sufficient to produce incorrect temperatures, corrections to the e-n collision frequency, like those suggested in Sec. 6.4.1 may be warranted.

6.5 Conclusions

Modeling partially ionized plasmas is complex due to the number of species and reactions, as well as the fact that many partially ionized plasmas are not in thermal equilibrium. The assumption of global or local thermal equilibrium greatly simplifies the problem. The high densities in THz plasmas suggest that simplifications might be made due to near-LTE conditions. The reacting 5-moment model by Meier and Shumlak was modified to include non-LTE corrections in Sec. 6.3. The approximations were validated against results from Bolsig+, a popular open-source electron Boltzmann equation solver Sec. 6.4. The approximations were found to agree reasonably well considering their simplicity. The electron-neutral collision

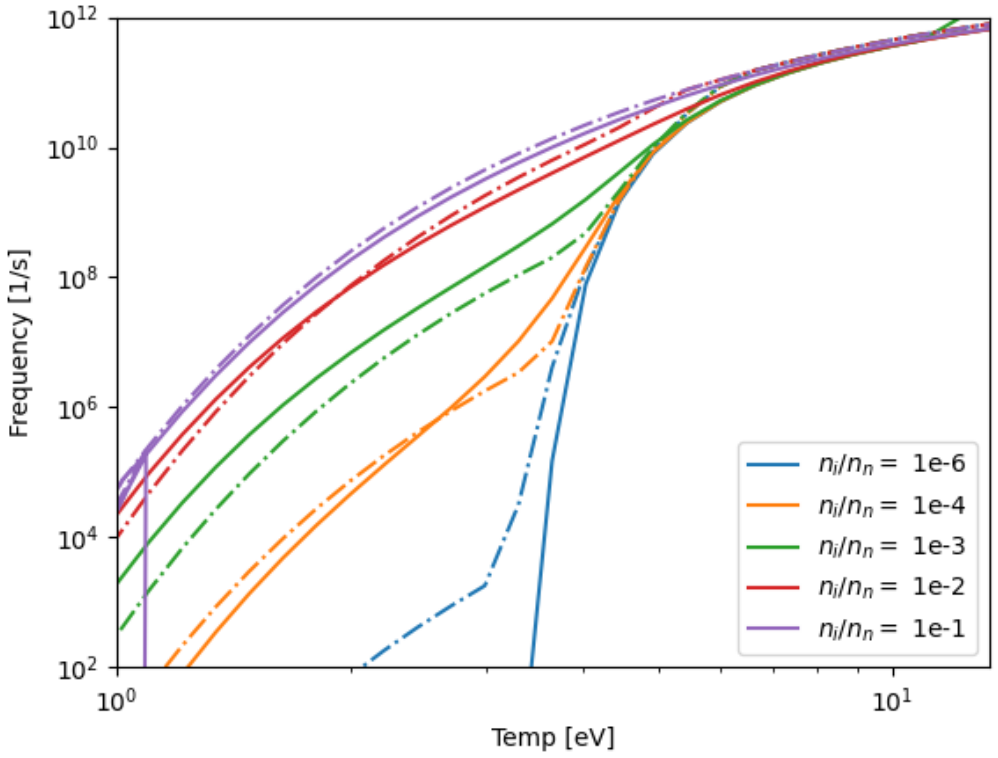

Figure 6.10: Argon total ionization frequency calculated with Bolsig+ (solid) and the DFTA+K_{Gr} method (dash dotted). The DFTA method (not shown) coincides with the dash dotted purple line. Coefficients for the K_{Gr} correction are $A = 2$, $B = 3/2$, $C = 2/5$, and $D = 4$. All calculations use Bolsig+ calculated drift velocities and temperatures. Anomalies in the Bolsig+ data are left for transparency. The DFTA+K_{Gr} ionization approximation method follows the general trends in the Bolsig+ results, and reduces error relative the DFTA method by six orders of magnitude in some cases.

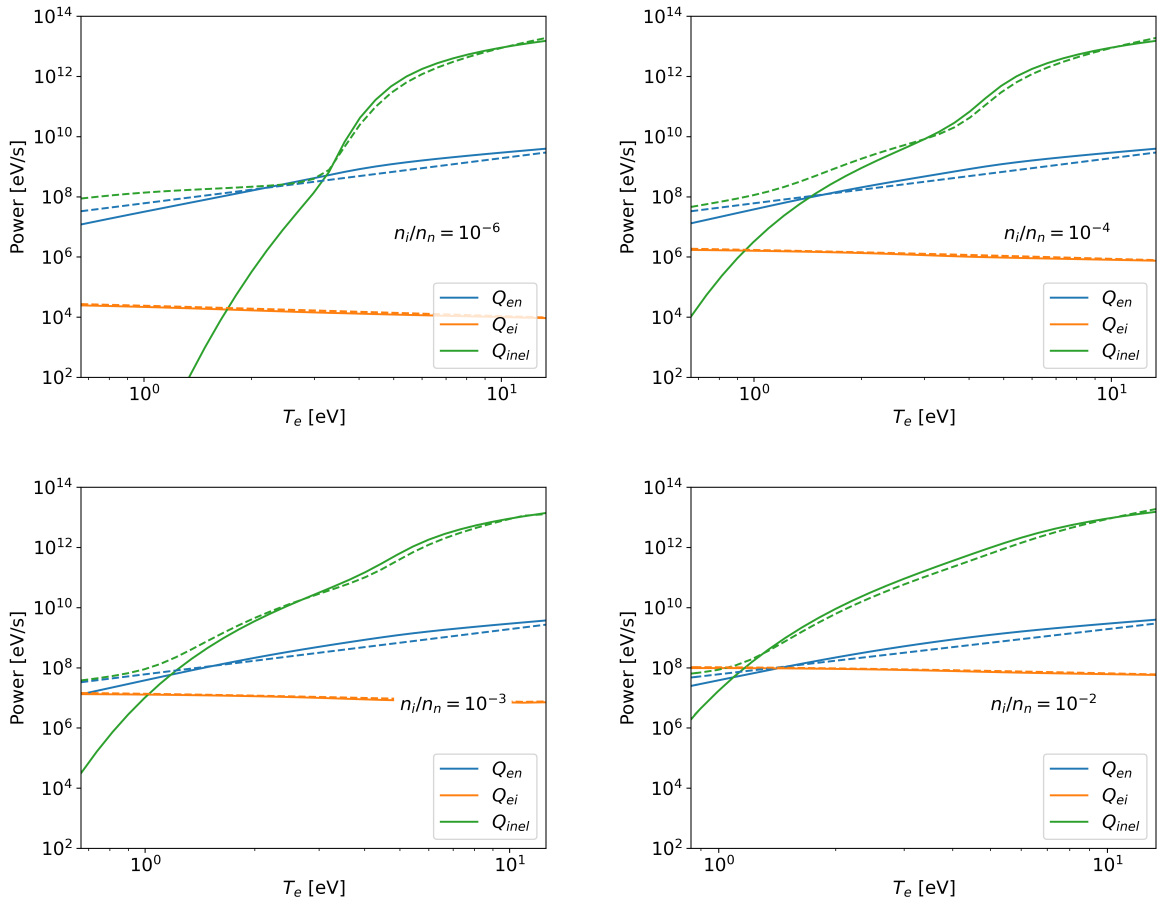

Figure 6.11: Power loss rates calculated with Bolsig+ (solid) and analytical method (dashed), compared for elastic e-n and e-i collisions as well as inelastic collisions (ionization and excitation) for $n_t = n_i + n_n = 2.5 \times 10^{25}$ m^{-3}. Ionization fractions are indicated on each panel. All calculations use Bolsig+ calculated drift velocities and temperatures. Power loss rates agree fairly well, with some departure at low ionization fraction and low temperature.

frequency with constant cross section approximates a "best fit" linear approximation of the Bolsig+ calculated frequencies for all cases, as does the election-ion collision frequency (see Fig. 6.9). The DFTA+K_{Gr} ionization approximation method also follows the general trends in the Bolsig+ results, and reduces error relative the DFTA method by six orders of magnitude in some cases (see Fig. 6.10). Finally power loss rates due to elastic and inelastic collisions are similar enough to suggest that reasonable equilibrium temperatures should be achievable with proposed model (see Fig. 6.11). Together, these findings imply that near-LTE modeling may be accessible without electron Boltzmann solvers. Next steps required to validate the model for AC fields in zero-, one-, and two-dimensions is discussed in Chap. 8.

Chapter 7

CONCLUSIONS

Plasma photonic crystals are a promising technology for high power THz applications. The ability to control transmission characteristic on microsecond times scales, the presence of natural plasma resonances in the high GHz and THz ranges, and resilience in the presence of high temperatures and high amplitude fields makes plasmas particularly well suited.

The study of plasma photonic crystals is a relatively new field. The investigation of plasma photonic crystals specifically for high power or THz applications is a narrow subset of an already small field. Furthermore, the construction of THz PPC experimental devices requires lattice sizes on the order of microns, plasma densities exceeding 10^{22} m^{-3}, and high power THz sources, all of which sit at the limit of, or outside, the capabilities of current technology. Analytical and numerical exploration of the THz PPCs is therefore strongly motivated. In this work, three complementary lines of research amenable to analytical or numerical treatment were developed to address gaps in the current literature.

Due to plasma's diffuse nature, PPCs cannot support short density-gradient scale lengths. A systematic understanding of the effect of smooth and discontinuous density profiles on transmission properties of PPCs is important to understanding and designing future PPC devices. In the first line of investigation pursued in Chaps. 3 and 4 the effect of smooth versus discontinuous density profiles in one- and two-dimensional PPCs on transmission characteristics was explored using a linear, infinitely periodic analytical model, band diagrams, and group velocity band gap maps.

In both the one- and two-dimensional cases, the shape of the density profile was found to have a large impact on certain aspects of the PPC transmission characteristics when the

plasma frequency of the average density exceeded half the lattice frequency. Discontinuities, associated with higher order density profile Fourier content, were found to be strongly correlated with the width of higher-order band gaps, and an analytical expression was derived for estimating these widths in the 1D case. High-order interactions of band gaps were also observed to lead to complex effects like forbidden islands, where band gaps open and close with increasing plasma frequency. Smooth density gradients in a two-dimensional PPC in TE polarized waves leads to large flat-band regions associated with surface plasmon resonances. The width of the flat-band region can be controlled through enforcing discontinuities with dielectric barriers or components. In all cases, when the plasma frequency is comparable or large than the lattice frequency, density profile shape becomes yet another parameter that can be used to design PPC transmission characteristics.

Analytical models of ideal, infinite PPCs are helpful in understanding the theoretical basis of device response and performance. Numerical models can extend theory to closer approximate the imperfections and complexity inherent in the physical world, but in a controlled environment. Real THz PPC devices will not only have gradients in plasma density, but they will be finite in size, they will absorb energy, and they will deform in the presence of strong fields.

In the second line of research described in Chap. 5, a two-fluid (electron-ion) 5-moment model is used to explore the impacts of non-ideal and non-linear effects like density profile shape, finite crystal size, plasma column radius, temperature, and high amplitude fields on a two-dimensional fully ionized plasma photonic crystal. The non-discontinuous density profiles in the finite crystals were found to reflect the findings in the ideal analytical study, and support interpretation of experimental results. The effects of finite photonic crystal size further clarified experimental transmission spectra interpretation. Non-linear effects due to plasma heating and plasma deformation in the presence of strong fields indicate that PPCs are robust in the presence of high power THz EM waves when the plasma is fully ionized.

Not all of the proposed PPC devices will involve fully ionized plasmas. At sufficiently high power, further ionization of the surrounding gas is inevitable, resulting in a non-linear PPC response. This effect can be an unintended side effect, or it can be harnessed intentionally. Solid state photonic crystals can be functionalized with self-initiated plasmas in resonant defects to provide passive power modulation. Understanding the plasma's formation, as well its interaction with the EM fields, is necessary to the design of high power THz devices.

Modeling of partially ionized plasmas is a complex problem. Thermal equilibrium often cannot be assumed, requiring the solution of the kinetic Boltzmann equation for each species and excited state and evaluating collision integrals for tens or hundreds of reactions. Electron Boltzmann equation solvers simplify this by calculating transport and reaction rates as a function of electric field strength or electron mean energy for use in fluid models. THz plasmas are dense, cool, and highly collisional, but still sit just on the edge of local thermal equilibrium.

In the final line of research (Chap. 6), a reacting three-fluid (electron-ion-atom) 5-moment model is extended to address collisions and reactions relevant to THz plasmas in near local thermal equilibrium. The approximations were validated against results from a Bolsig+, a popular open-source electron Boltzmann equation solver. The approximations were found to agree reasonably well, considering their simplicity, and imply that near-LTE modeling may be accessible without electron Boltzmann solvers.

In summary, the transmission characteristics of high power THz PPCs are complex. Not only do they encompass the photonic band gap behavior of dielectric PCs, the surface plasmon resonance characteristic of metallic PCs, and non-ideal effects due to finite sized PPC arrays, but plasma profile shape must also be considered. High power THz waves can also cause ionization, intentionally or unintentionally, eliciting a whole variety of non-linear PPC response. Fortunately, simple corrections to plasma reaction rates used in reacting fluid models, previously constrained to partially ionized plasmas in local thermal equilibrium, have

promise to extend modeling capabilities into the THz plasma regime.

This work was successful in elucidating several important characteristics of high power THz PPC devices. Furthermore, the research presented in this dissertation lays the groundwork for continued investigation in several areas. The next chapter (Chap. 8) outlines these areas of research in more detail.

Chapter 8

FUTURE WORK

While this work outlined in this thesis was successful in elucidating several important characteristics of potential high power THz PPC devices, groundwork was laid for continued investigation in several areas. Two topics are particularly complementary to the work already completed: an exploration of partial and complete band gap characteristics of two-dimensional smooth and discontinuous PPCs using band gap maps, and the investigation of a theoretical passive plasma enhanced PPC device using the extended reacting three-fluid model.

8.1 Band gap maps for smooth and discontinuous density profiles in two-dimensional PPCs

Group velocity band gap maps proved to be a powerful tool in comparing and contrasting the band gap behavior of smooth and discontinuous 1D PPCs. Two-dimensional PPCs can likely benefit from the same treatment, but the complex band structure, and two-dimensional wavenumber space provides challenges visualizing band gap maps in the same way a 1D PPCs. One approach is to examine the band gap maps for each principal propagation axis separately. This highlights the existence of partial as well as complete band gaps. Partial band gaps can be important to preferential wave guiding and can provide a deeper understanding of dispersion behavior. Future work might involve designing band gap maps for smooth and discontinuous two-dimensional PPCs that facilitate a deeper understanding of density profile shape in band gap behavior.

8.2 THz breakdown in PPC device

A next step in this work would to validate the model in a time-varying simulation with AC fields. A multi-term, multi-harmonic Boltzmann solver[87] that has been validated for high GHz and low THz plasmas may be used as a benchmark. Finally, space-varying fields may be tested in a two-dimensional simulation and validated against the experimental and simulation work of Parsons and Gregório for the low GHz frequencies, before being applied to theoretical THz devices.

BIBLIOGRAPHY

[1] JB Chown, WE Scharfman, and T Morita. Voltage breakdown characteristics of microwave antennas. *Proceedings of the IRE*, 47(8):1331–1337, 1959.

[2] WC Taylor, W Scharfman, and T Morita. Voltage breakdown of microwave antennas. *Advances in Microwaves*, 7:59–130, 1971.

[3] J. Lawson. Micro plasma limiter for rf and microwave circuit protection, 1933.

[4] Suman D Patel, Leonard Dubrowsky, SE Saddow, R Kaul, and RV Garver. Microstrip plasma limiter. In *IEEE MTT-S International Microwave Symposium Digest*, pages 879–882. IEEE, 1989.

[5] Antoine Simon, Romain Pascaud, Thierry Callegari, Laurent Liard, Olivier Pascal, and Olivier Pigaglio. Static and dynamic control of limiting threshold in plasma-based microstrip microwave power limiter. In *2017 IEEE MTT-S International Microwave Symposium (IMS)*, pages 1987–1990. IEEE, 2017.

[6] Abbas Semnani, Sergey O Macheret, and Dimitrios Peroulis. A high-power widely tunable limiter utilizing an evanescent-mode cavity resonator loaded with a gas discharge tube. *IEEE Transactions on Plasma Science*, 44(12):3271–3280, 2016.

[7] Zach Vander Missen, Abbas Semnani, and Dimitrios Peroulis. Toward a high-power high-isolation wideband plasma limiter. In *2019 IEEE 20th Wireless and Microwave Technology Conference (WAMICON)*, pages 1–4. IEEE, 2019.

[8] Daniel M Mittleman. Perspective: Terahertz science and technology. *Journal of Applied Physics*, 122(23):230901, 2017.

[9] Zhi Chen, Xinying Ma, Bo Zhang, Yaxin Zhang, Zhongqian Niu, Ningyuan Kuang, Wenjie Chen, Lingxiang Li, and Shaoqian Li. A survey on terahertz communications. *China Communications*, 16(2):1–35, 2019.

[10] John H Booske. Plasma physics and related challenges of millimeter-wave-to-terahertz and high power microwave generation. *Physics of plasmas*, 15(5):055502, 2008.

[11] Jianming Dai, Jingle Liu, and Xi-Cheng Zhang. Terahertz wave air photonics: terahertz wave generation and detection with laser-induced gas plasma. *IEEE Journal of selected topics in Quantum Electronics*, 17(1):183–190, 2010.

[12] I. Adamovich, S. D. Baalrud, A. Bogaerts, P. J. Bruggeman, M. Cappelli, V. Colombo, U. Czarnetzki, U. Ebert, J. G. Eden, P. Favia, D. B. Graves, S. Hamaguchi, G. Hieftje, M. Hori, I. D. Kaganovich, U. Kortshagen, M. J. Kushner, N. J. Mason, S. Mazouffre, S. Mededovic Thagard, H. R. Metelmann, A. Mizuno, E. Moreau, A. B. Murphy, B. A. Niemira, G. S. Oehrlein, Z. Lj Petrovic, L. C. Pitchford, Y. K. Pu, S. Rauf, O. Sakai, S. Samukawa, S. Starikovskaia, J. Tennyson, K. Terashima, M. M. Turner, M. C.M. Van De Sanden, and A. Vardelle. The 2017 Plasma Roadmap: Low temperature plasma science and technology. *Journal of Physics D: Applied Physics*, 50(32), 2017.

[13] Hitoshi Hojo and Atsushi Mase. Dispersion Relation of Electromagnetic Waves in One-Dimensional Plasma Photonic Crystals. *Journal of Plasma and Fusion Research*, 80(2):89–90, 2004.

[14] U. Shumlak and J. Loverich. Approximate riemann solver for the two-fluid plasma model. *Journal of Computational Physics*, 187(2):620–638, 2003.

[15] E. T. Meier and U. Shumlak. A general nonlinear fluid model for reacting plasma-neutral mixtures. *Physics of Plasmas*, 19(7), 2012.

[16] Stephen G. Parsons and Jeffrey Hopwood. Millimeter wave plasma formation within a 2d photonic crystal. *IEEE Electron Device Letters*, 38:1602–1605, 2017.

[17] GJM Hagelaar and LC Pitchford. Solving the boltzmann equation to obtain electron transport coefficients and rate coefficients for fluid models. *Plasma sources science and technology*, 14(4):722, 2005.

[18] Amnon Yariv and Pochi Yeh. *Optical Waves in Crystals: Propagation and Control of Laser Radiation.* Wiley, 1984.

[19] Eli Yablonovitch. Inhibited spontaneous emission in solid-state physics and electronics. *Physical Review Letters*, 58(20):2059–2062, 1987.

[20] Jean-michel Lourtioz, Henri Benisty, Vincent Berger, Jean-michel Gerard, Daniel Maystre, and Alexei Tchelnokov. *Photonic Crystals: Towards Nanoscale Photonic Devices*. Springer-Verlag Berlin Heidelberg, second edition edition, 2008.

[21] John D Joannopoulos, Steven Johnson, Joshua N Winn, and Robert D Meade. *Photonic crystals: molding the flow of light*. Princeton University Press, second edition edition, 2008.

[22] M. Ramezani Masir, P. Vasilopoulos, and F. M. Peeters. Kronig-Penney model of scalar and vector potentials in graphene. *Journal of Physics Condensed Matter*, 22(46), 2010.

[23] Kamil Boratay Alici and Ekmel Özbay. Radiation properties of a split ring resonator and monopole composite. *Physica status solidi (b)*, 244(4):1192–1196, 2007.

[24] N. Fang and Xiang Zhang. Imaging properties of a metamaterial superlens. In *Proceedings of the 2nd IEEE Conference on Nanotechnology*, pages 225–228, 2002.

[25] Koray Aydin, Irfan Bulu, and Ekmel Ozbay. Subwavelength resolution with a negative-index metamaterial superlens. *Applied physics letters*, 90(25):254102, 2007.

[26] Andrea Alu and Nader Engheta. Plasmonic and metamaterial cloaking: Physical mechanisms and potentials. *Journal of Optics A: Pure and Applied Optics*, 10(9), 2008.

[27] Christine T Chevalier, Analex Corporation, Brook Park, and Jeffrey D Wilson. Frequency Bandwidth Optimization of Left-Handed Metamaterial. Technical Report NASA/TM-2004-213403, NASA, 2004.

[28] J. B. Pendry, D. Schurig, and D. R. Smith. Controlling Electromagnetic Fields. *Science (American Association for the Advancement of Science)*, 312:1780–1782, 2006.

[29] Xiaohua Huang and Mostafa A. El-Sayed. Gold nanoparticles: Optical properties and implementations in cancer diagnosis and photothermal therapy. *Journal of Advanced Research*, 1(1):13–28, 2010.

[30] Jan Krajczewski, Karol Kołątaj, and Andrzej Kudelski. Plasmonic nanoparticles in chemical analysis. *RSC Advances*, 7(28):17559–17576, 2017.

[31] Guanying Chen, Jangwon Seo, Chunhui Yang, and Paras N. Prasad. Nanochemistry and nanomaterials for photovoltaics. *Chemical Society Reviews*, 42(21):8304, 2013.

[32] Kazuaki Sakoda. *Optical properties of photonic crystals*. Springer series in optical sciences. Springer, 2001.

[33] Osamu Sakai, Takui Sakaguchi, and Kunihide Tachibana. Photonic bands in two-dimensional microplasma arrays. I. Theoretical derivation of band structures of electromagnetic waves. *Journal of Applied Physics*, 101(7), 2007.

[34] F. Righetti, B. Wang, and M. A. Cappelli. Enhanced attenuation due to lattice resonances in a two-dimensional plasma photonic crystal. *Physics of Plasmas*, 25(12):124502, 2018.

[35] B. Wang and M. A. Cappelli. A tunable microwave plasma photonic crystal filter. *Applied Physics Letters*, 107(17), 2015.

[36] O. Sakai, T. Sakaguchi, Y. Ito, and K. Tachibana. Interaction and control of millimetre-waves with microplasma arrays. *Plasma Physics and Controlled Fusion*, 47(12 B):B617–B627, dec 2005.

[37] B. Wang and M. A. Cappelli. A plasma photonic crystal bandgap device. *Applied Physics Letters*, 108(16), 2016.

[38] J. Loverich and U. Shumlak. Nonlinear full two-fluid study of m=0 sausage instabilities in an axisymmetric Z pinch. *Physics of Plasmas*, 13(8), 2006.

[39] Weili Fan, Xinchun Zhang, and Lifang Dong. Two-dimensional plasma photonic crystals in dielectric barrier discharge. *Physics of Plasmas*, 17(11), 2010.

[40] Osamu Sakai and Kunihide Tachibana. Plasmas as metamaterials: A review. *Plasma Sources Science and Technology*, 21(1):013001, feb 2012.

[41] G. Lehmann and K. H. Spatschek. Transient Plasma Photonic Crystals for High-Power Lasers. *Physical Review Letters*, 116(22):1–5, 2016.

[42] G. Lehmann and K. H. Spatschek. Laser-driven plasma photonic crystals for high-power lasers. *Physics of Plasmas*, 24(5), 2017.

[43] V. Kuzmiak and A. Maradudin. Photonic band structures of one- and two-dimensional periodic systems with metallic components in the presence of dissipation. *Physical Review B - Condensed Matter and Materials Physics*, 55(12):7427–7444, 1997.

[44] Li Mei Qi, Zi Qiang Yang, Feng Lan, Xi Gao, and Da Zhi Li. Dispersion characteristics of two-dimensional unmagnetized dielectric plasma photonic crystal. *Chinese Physics B*, 19(3):034210, mar 2010.

[45] Allen Taflove. *Computational electrodynamics : the finite-difference time-domain method*. Artech House, Boston, 1995.

[46] Malgorzata Celuch-Marcysiak and Wojciech K. Gwarek. Spatially Looped Algorithms for Time-Domain Analysis of Periodic Structures. *IEEE Transactions on Microwave Theory and Techniques*, 43(4):860–865, 1995.

[47] Ardavan F. Oskooi, David Roundy, Mihai Ibanescu, Peter Bermel, J. D. Joannopoulos, and Steven G. Johnson. Meep: A flexible free-software package for electromagnetic simulations by the FDTD method. *Computer Physics Communications*, 181(3):687–702, 2010.

[48] Min Qiu and Sailing He. FDTD algorithm for computing the off-plane band structure in a two-dimensional photonic crystal with dielectric or metallic inclusions. *Physics Letters, Section A: General, Atomic and Solid State Physics*, 278(6):348–354, 2001.

[49] Osamu Sakai and Kunihide Tachibana. Dynamic control of propagating electromagnetic waves using tailored millimeter plasmas on microstrip structures. *IEEE Transactions on Plasma Science*, 34(1):80–87, 2006.

[50] Jan Trieschmann and Thomas Mussenbrock. Kinetic bandgap analysis of plasma photonic crystals. *Journal of Applied Physics*, 124(17):173302, 2018.

[51] JP Albert, C Jouanin, D Cassagne, and D Bertho. Generalized wannier function method for photonic crystals. *Physical Review B*, 61(7):4381, 2000.

[52] Maurizio Lontano and Nicolai Lunin. Propagation of electromagnetic waves in a density-modulated plasma. *Journal of Plasma Physics*, 45:173–190, 1991.

[53] Maurizio Lontano and Nicolai Lunin. Density-modulation effects on the propagation of an electromagnetic wave in a plasma. *Journal of Plasma Physics*, 48:209–214, 1992.

[54] L. Qi, L. Shang, and S. Zhang. One-dimensional plasma photonic crystals with sinusoidal densities. *Physics of Plasmas*, 21(1):013501, 2014.

[55] Wei Chen, Lixia Yang, Zhaowen Zheng, and Pingping Yu. Investigation on bandgaps of 1D space-varying plasma photonic crystal. *2012 International Conference on Microwave and Millimeter Wave Technology, ICMMT 2012 - Proceedings*, 3:843–846, 2012.

[56] S. Prasad, V. Singh, and A. K. Singh. Effect of inhomogeneous plasma density on the reflectivity in one dimensional plasma photonic crystal. *Progress In Electromagnetics Research M*, 21(November):211–222, 2011.

[57] Bin Guo and Xiao-Ming Qiu. Differential transfer matrix method for photonic band structure of one dimensional non-uniform distribution plasma photonic crystal. *Optik*, 123(15):1390–1392, aug 2012.

[58] P. Drude. Zur elektronentheorie der metalle. *Annalen der Physik*, 306:566–613, 1 1900.

[59] P. Drude. Zur elektronentheorie der metalle; ii. teil. galvanomagnetische und thermomagnetische effecte. *Annalen der Physik*, 308:369–402, 1 1900.

[60] Felix Bloch. *Über die Quantenmechanik der Elektronen in Kristallgittern*. PhD thesis, Universität Leipzig, 1928.

[61] A. Hakim and U. Shumlak. Two-fluid physics and field-reversed configurations. *Physics of Plasmas*, 14(5):055911, 2007.

[62] Bernardo Cockburn and Chi-Wang Shu. Tvb runge-kutta local projection discontinuous galerkin finite element method for conservation laws ii : General framework. *Mathematics of Computation*, 52:411–435, 1989.

[63] U. Shumlak, R. Lilly, N. Reddell, E. Sousa, and B. Srinivasan. Advanced physics calculations using a multi-fluid plasma model. *Computer Physics Communications*, 182(9):1767–1770, 2011.

[64] Deane T. Prescott and N. V. Shuley. Extensions to the fdtd method for the analysis of infinitely periodic arrays. *IEEE Microwave and Guided Wave Letters*, 4:352–354, 1994.

[65] V. A. Tolmachev, T. S. Perova, J. Ruttle, and E. V. Khokhlova. Design of one-dimensional photonic crystals using combination of band diagram and photonic gap map approaches. *Journal of Applied Physics*, 104(3):033536, 2008.

[66] Jean Michel Lourtioz, Henri Benisty, Vincent Berger, Jean Michel Gérard, Daniel Maystre, Alexei Tchelnokov, and Dominique Pagnoux. *Photonic crystals: Towards nanoscale photonic devices*. Springer, 2005.

[67] I. A. Sukhoivanov, I. V. Guryev, J. A. Andrade Lucio, E. Alvarado Mendez, M. Trejo-Duran, and M. Torres-Cisneros. Photonic density of states maps for design of photonic crystal devices. *Microelectronics Journal*, 39(3-4):685–689, 2008.

[68] Limei Qi, Chao Li, Guangyou Fang, and Xiang Gao. The absorbing properties of two-dimensional plasma photonic crystals. *Plasma Science and Technology*, 17(1):4–9, jan 2015.

[69] S. I. Braginskii. Transport processes in plasmas, 1986.

[70] J. Loverich and U. Shumlak. A discontinuous galerkin method for the full two-fluid plasma model. *Computer Physics Communications*, 169(1):251–255, 2005. Proceedings of the Europhysics Conference on Computational Physics 2004.

[71] A. Hakim, J. Loverich, and U. Shumlak. A high resolution wave propagation scheme for ideal two-fluid plasma equations. *Journal of Computational Physics*, 219(1):418–442, 2006.

[72] Bhuvana Srinivasan, Ammar Hakim, and Uri Shumlak. Numerical methods for two-fluid dispersive fast mhd phenomena. *Communications in Computational Physics*, 10(1):183–215, 2011.

[73] Sean T Miller and Uri Shumlak. A multi-species 13-moment model for moderately collisional plasmas. *Physics of Plasmas*, 23(8):082303, 2016.

[74] E.M. Sousa and U. Shumlak. A blended continuous–discontinuous finite element method for solving the multi-fluid plasma model. *Journal of Computational Physics*, 326:56–75, 2016.

[75] IAM Datta, DW Crews, and U Shumlak. Electromagnetic extension of the dory–guest–harris instability as a benchmark for vlasov–maxwell continuum kinetic simulations of magnetized plasmas. *Physics of Plasmas*, 28(7):072112, 2021.

[76] B. Wang and M. A. Cappelli. Waveguiding and bending modes in a plasma photonic crystal bandgap device. *AIP Advances*, 6(6), 2016.

[77] Fabio Righetti. *Gaseous Plasmonic Structures for Gigahertz and Low Terahertz Wave Manipulation*. PhD thesis, Stanford University, 2020.

[78] Fabio Righetti and Mark A Cappelli. Electromagnetic response of a limited-size two dimensional plasma grating formed by cw laser pumping. In *APS Annual Gaseous Electronics Meeting Abstracts*, pages FT1–081, 2019.

[79] José Gregório, Stephen Parsons, and Jeffrey Hopwood. Reconfigurable photonic crystal using self-initiated gas breakdown. *Plasma Sources Science and Technology*, 26(2):0–5, 2017.

[80] J. Gregório, P. Leprince, C. Boisse-Laporte, and L. L. Alves. Self-consistent modelling of atmospheric micro-plasmas produced by a microwave source. *Plasma Sources Science and Technology*, 21(1), 2012.

[81] Emanuele Arcese, François Rogier, and Jean Pierre Boeuf. Plasma fluid modeling of microwave streamers: Approximations and accuracy. *Physics of Plasmas*, 24, 2017.

[82] SS Dhillon, MS Vitiello, EH Linfield, AG Davies, Matthias C Hoffmann, John Booske, Claudio Paoloni, M Gensch, Peter Weightman, GP Williams, et al. The 2017 terahertz science and technology roadmap. *Journal of Physics D: Applied Physics*, 50(4):043001, 2017.

[83] Hans R Griem. Validity of local thermal equilibrium in plasma spectroscopy*. *Physical Review*, 131:1170–1176, 1963.

[84] L. L. Alves, A. Bogaerts, V. Guerra, and M. M. Turner. Foundations of modelling of nonequilibrium low-temperature plasmas. *Plasma Sources Science and Technology*, 27, 2018.

[85] Kailash Kumar and RE Robson. Mobility and diffusion. i. boltzmann equation treatment for charged particles in a neutral gas. *Australian Journal of Physics*, 26(2):157–186, 1973.

[86] Pierre Segur, Marie Claude Bordage, Jean Pierre Balaguer, and Mohamed Yousfi. The application of a modified form of thesn method to the calculation of swarm parameters of electrons in a weakly ionised equilibrium medium. *Journal of Computational Physics*, 50:116–137, 1983.

[87] Jacob Coty Stephens. A multi-term, multi-harmonic boltzmann equation model for kinetic behavior in intense microwave and terahertz excited low temperature plasmas. *Physics of Plasmas*, 25, 2018.

[88] G J M Hagelaar and G M W Kroesen. Speeding up fluid models for gas discharges by implicit treatment of the electron energy source term. *Journal of Computational Physics*, 159:1–12, 2000.

[89] Emile Carbone, Wouter Graef, Gerjan Hagelaar, Daan Boer, Matthew M Hopkins, Jacob C Stephens, Benjamin T Yee, Sergey Pancheshnyi, Jan van Dijk, and Leanne Pitchford. Data needs for modeling low-temperature non-equilibrium plasmas: the lxcat project, history, perspectives and a tutorial. *Atoms*, 9(1):16, 2021.

[90] Leanne C Pitchford, Luis L Alves, Klaus Bartschat, Stephen F Biagi, Marie-Claude Bordage, Igor Bray, Chris E Brion, Michael J Brunger, Laurence Campbell, Alise Chachereau, et al. Lxcat: An open-access, web-based platform for data needed for modeling low temperature plasmas. *Plasma Processes and Polymers*, 14(1-2):1600098, 2017.

[91] G. J. M Hagelaar. Coulomb collisions in the boltzmann equation for electrons in low-temperature gas discharge plasmas. *Plasma Sources Sci. Technol*, 25:15015, 2016.

[92] R. P. McEachran and A. D. Stauffer. Momentum transfer cross sections for the heavy noble gases. *European Physical Journal D*, 68, 2014.

[93] Lyman Spitzer and Richard Härm. Transport phenomena in a completely ionized gas. *Physical Review*, 89:977–981, 1953.

[94] Fred L. Hinton. Collisional transport in plasmas, 1983.

[95] Julien Annaloro, Vincent Morel, Arnaud Bultel, and Pierre Omaly. Global rate coefficients for ionization and recombination of carbon, nitrogen, oxygen, and argon. *Physics of Plasmas*, 19, 2012.

[96] G. S. Voronov. A practical fit formula for ionization rate coefficients of atoms and ions by electron impact: Z = 1-28. *Atomic Data and Nuclear Data Tables*, 65(1):1–35, 1997.

[97] C. Hombourger. An empirical expression for K-shell ionization cross section by electron impact. *Journal of Physics B: Atomic, Molecular and Optical Physics*, 31(16):3693–3702, 1998.

[98] Michał Gryziński. Two-particle collisions. ii. coulomb collisions in the laboratory system of coordinates. *Physical review*, 138(2A):A322, 1965.

[99] Michał Gryziński. Classical theory of atomic collisions. i. theory of inelastic collisions. *Physical Review*, 138(2A):A336, 1965.

[100] E. T. Meier, A. H. Glasser, V. S. Lukin, and U. Shumlak. Modeling open boundaries in dissipative MHD simulation. *Journal of Computational Physics*, 231(7):2963–2976, 2012.

[101] Eder M. Sousa. *A Blended Finite Element Method for Multi-fluid Plasma Modeling*. PhD thesis, University of Washington, 2014.

[102] V. M. Zhdanov and A. A. Stepanenko. Kinetic theory of transport processes in partially ionized reactive plasma, i: General transport equations. *Physica A: Statistical Mechanics and its Applications*, 446:35–53, 2016.

[103] E Nagnibeda and E Kustova. Chapter 6: Reaction rate coefficients, 2009.

Appendix A

FLOQUET-BLOCH PERIODIC BOUNDARY CONDITIONS

A.1 Motivation

In periodic problems, there are many cases where the periodicity of waves propagating through the domain need not be the same as the spatial periodicity of the medium. For example, while a rectangular crystal lattice can be represented accurately by a unit cell with periodic boundaries, the electromagnetic waves propagating through that crystal will be confined to only those that are integer multiples of the crystal period. To allow for other wavelengths the entire crystal would need to be simulated, and any advantage gained by the symmetry of the periodic problem would be lost.

Floquet-Bloch periodic boundary conditions allow for medium and EM wave periodicity to be different, while still only simulating the unit cell. Phase shifts corresponding to the wave vector of interest are applied to complex electromagnetic fields at the unit cell boundaries. A separate simulation must be run for each wave vector.

A.2 Theory

A phase shift ψ can be applied to a wave as it passes a boundary,

$$\mathbf{F}^1(\mathbf{x}) = \mathbf{F}^2(\mathbf{x})e^{j\psi}, \tag{A.1}$$

$$\mathbf{F}^2(\mathbf{x}) = \mathbf{F}^1(\mathbf{x})e^{-j\psi}, \tag{A.2}$$

where

$$\psi = \mathbf{k} \cdot \mathbf{a}, \tag{A.3}$$

and $\mathbf{F}$ is the field variable, superscript 1 and 2 denote the left and right boundaries, $k = 1/\lambda$ is the wave vector of the phase shift, and a is vector of periodic lengths in each direction.

As these boundary conditions are in effect replicating the same symmetry as Bloch theorem, they are commonly referred to as Bloch periodic boundary conditions. Similarly, the numerical model can also be used to find the eigenvalues and eigenstates of the photonic crystal. For further reading, please see the article by Celuch-Marcysiak, et al [46].

A.3 Implementation in WARPXM

See the Doxygen for `src/apps/general_apps/bloch`.

A.4 Using Floquet-Bloch periodic boundaries

A.4.1 Mesh requirements

Enough subdomains so that no subdomain will touch itself across periodic boundaries. This can generally be accomplished with two.

A.4.2 Special variables and boundary conditions

Separate sets of real and imaginary variables are assigned to *each* subdomain, including the fluid variables. The real and imaginary variables will be evolved separately, only coupled at the Bloch boundary conditions.

Separate field variables in the upper and lower domain are necessary to allow for discontinuous solutions at periodic boundaries where the phase shift occurs. Considering this requirement, one of the vacuum domain variables can be assigned to the plasma domain, so as to reduce the required number of sets of variables (see Figure A.2).

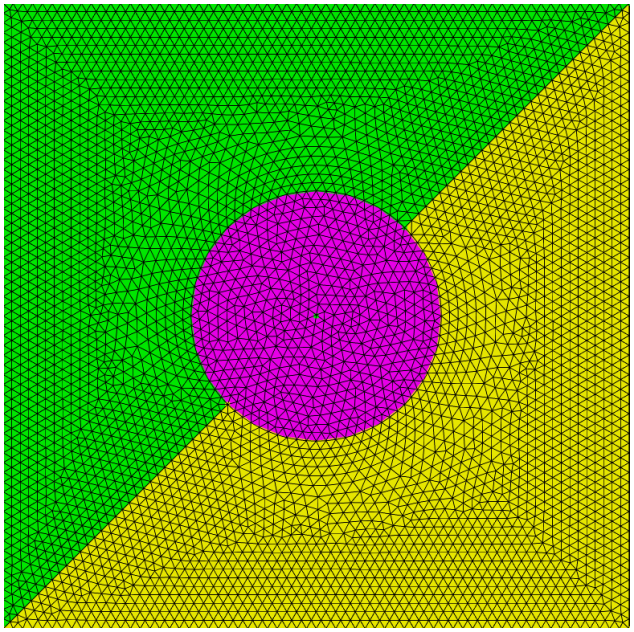

Figure A.1: Example of a mesh subdomain division necessary for two sets of Bloch periodic boundary conditions on a 2D domain.

A.4.3 The "bloch_var" WARPy helper class, and simplified input files

The `bloch_var` helper class can be used to set up all the variables, boundary conditions, and flux and source apps across two subdomains. Details on the implementation can be found in the Doxygen for the `warpy.helpers.bloch_var` class.

Initializing a bloch_var object for each variable

```
1    field = warpy.helpers.bloch_var(
2        variable_name='field',
3        components=['Ex', 'Ey', 'Ez', 'Bx', 'By', 'Bz'],
4        sorder=sorder,
5        region1=left_subdomains,
```

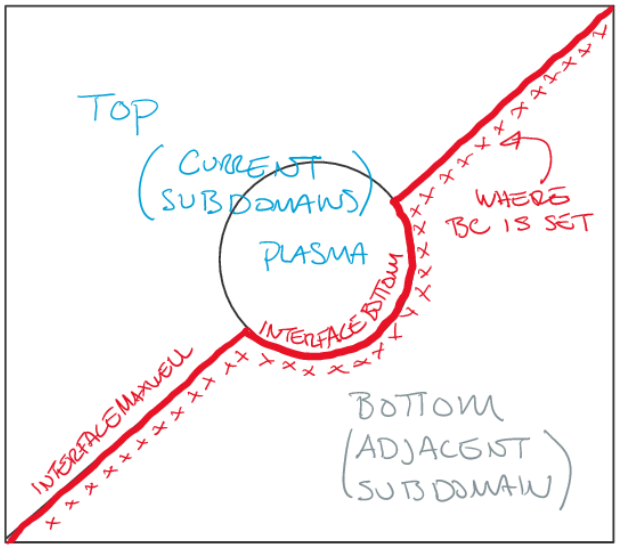

Figure A.2: Unit cell domain showing subdomain division. "Top" and "Plasma" contain one set of field variables, and "Bottom" has another set. Virtual boundary conditions are then required to pass the solution across the interior (red) and exterior boundary conditions

```
6         region2=right_subdomains,
7         region1_periodic=left_periodic_boundaries,
8         region2_periodic=right_periodic_boundaries,
9         region12_interface=interface_boundaries)
```

Setting initial conditions

Wrapper functions for several initial conditions have been created to facilitate applying initial conditions across the complex and real parts of each sub-region variable. The methods return a list of initial condition functions. The `va_runner` is used to apply the initial condition functions once they are set up, as usual.

```
va_ics = []
va_ics += field.ic_sine1d(
    background_value=0.,
    pert_amplitude=B_norm,
    wavelength=1.,
    components=['Bz'])
va_ics += field.ic_sine1d(
    background_value=0.,
    pert_amplitude=E_norm,
    wavelength=1.,
    components=['Ey']
ha_ic = warpy.host_actions.va_runner(
    name='ha_ic', variable_adjusters=va_ics)
```

Initial conditions that have wrappers in `bloch_var` are:

- `ic_maxwell_sinc`: A 2D sinc function for Maxwell variables.

- `ic_fivemoment_pulse`: Creates a 2D rectangular array of identical plasma density columns with the option for parabolic density profile.

- `ic_sine1d`: A minimalist wrapper on the `fourier` initial condition.

- `ic_fourier_square_1d`: Uses the `fourier` initial condition to make a Fourier approximation of square wave, with specified number of terms.

- `ic_sine2d`: Minimalist wrapper on the `sine2d` initial condition function.

- `ic_setto`: Minimalist wrapper on the `setto` initial condition function.

Applying flux and source applications, spatial solvers

Flux and source wrappers have been created for a few common Maxwell and 5-moment model applications. The wrapper methods return two lists of applications, one for each sub-region. Currently, they have to be separated and passed to separate spatial solvers. This may be simplified in the future.

```
apps_left = []
apps_right = []

# Apps for the fluid
apps_fluids = electron_fluid.apps_euler_field_source(
    field=field,
    mass=A_e,
    charge=charge_e_norm,
    skin_depth_norm=skin_depth_norm)
apps_left += apps_fluids[0]
apps_right += apps_fluids[1]

# Apps for the for fields
apps_fields = field.apps_maxwell_flux(
    skin_depth_norm=skin_depth_norm,
    omega_p_norm=omega_p_tau,
    rel_permittivity=epsilon_r)
apps_left += apps_fields[0]
apps_right += apps_fields[1]

# Spatial solvers
spatial_solver_left = warpy.spatial_solvers.dg(
    name="dg_left",
    spatial_order=sorder,
```

```
    applications=apps_left,
    on_subdomains=left_subdomains)

spatial_solver_right = warpy.spatial_solvers.dg(
    name="dg_right",
    spatial_order=sorder,
    applications=apps_right,
    on_subdomains=right_subdomains)
```

Boundary conditions

Everything associated with the Floquet-Bloch specific boundary conditions happen in a single function call for each variable. The function returns a list of boundary condition variable adjusters that can be passed to a temporal solver as usual.

```
va_bc_bloch = []
va_bc_bloch += field.va_bc_bloch(
    k_vector=bloch_k,
    a_vector=bloch_a)
va_bc_bloch += electron_fluid.va_bc_bloch(
    k_vector=[0.0, 0.0, 0.0],
    a_vector=bloch_a)
```

Physical boundary conditions are not currently being handled.

Writing out variables

Until now, the four sub variable created for each variable have not been hidden from the user. To access these variable for write out purposes, a `get_vars` method has been created.

```
variables_left = field.get_vars(region='region1')
```

```
variables_right = field.get_vars(region='region2')
variables_left += electron_fluid.get_vars(region='region1')
variables_right += electron_fluid.get_vars(region='region2')

writer = warpy.host_actions.writer(
    name='writer',
    WriteInterval=1000,
    ReadVars=variables_left + variables_right)
```

A.5 Example

In the example `user_runs\whitney_thomas\ppc\5_moment\bloch_periodic.py` a series of simulations is run with different wave vectors k. Fourier transforms are performed on probe field data to extract dominant frequencies for each simulations. These frequencies are then plotted versus wave number to create a dispersion relation, or band diagram, for the crystal (see Figure A.3).

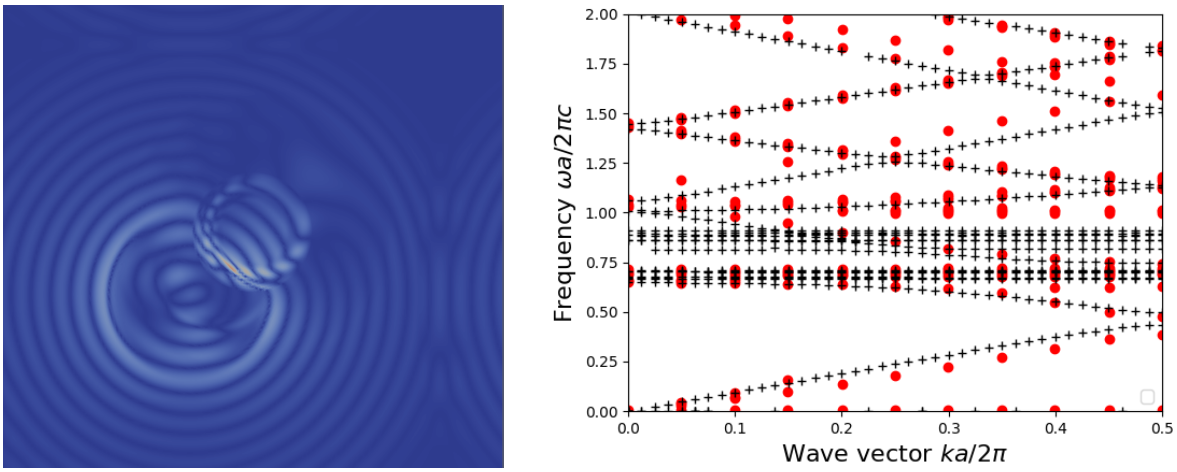

Figure A.3: (Right) initial condition with circular sinc pulse, and (left) a band diagram generated using the WARPXM implemented Bloch boundary conditions (red dots) compared to bands generated by another program, Meep (+).

Appendix B

LACUNA BASED OPEN BOUNDARY CONDITION IMPLEMENTATION IN WARPXM

B.1 Motivation for open boundary conditions

There are many situations in plasma physics (and in fluid dynamics in general) where the region of interest is small compared to the distances information can propagate over the simulation time. Say, when a plasma is being irradiated by microwaves that aren't entirely absorbed, or plasma waves produced near a wall from sheath formation propagate into the bulk plasma, or a hurricane moving in a jet stream. If an artificial wall is simulated at the edges of the regions of interest, wave energy will be reflected back into the domain, skewing results. If the domain was made large enough that information could not reach the boundaries during the simulation, then large amounts of computation time would have to be spent advancing an effectively useless solution.

To solve this problem, boundary conditions that allow information to pass freely out of a simulation domain are necessary. While a number of simple open boundary conditions are adequate over short periods or with linear hyperbolic equations (zero normal derivative (ZND), or perfectly matched layers (PML)) they will accumulate error over long simulations, or mixed parabolic-hyperbolic systems.

A lacuna-based open boundary condition (LOBC) is proposed by E.T. Meier, et al, in [100]. The LOBC works by passing the interior solution to an exterior auxiliary variable via a source term. The auxiliary solution is then effectively damped out before reaching the exterior boundary, ensuring that information about the boundary cannot re-enter the interior domain.

B.2 Lacuna-based open boundary condition theory

The lacuna-based boundary condition (LOBC) is based on the fact that after a wave has passed, a fluid will return to its previous state. This quiescent region immediately following a wave is called a lacuna. The LOBC takes advantage of this idea by assuming that the lacuna of a wave is in the same state than if that wave had never passed by. In this case, if an earlier wave were suddenly "deleted" from the history of an auxiliary variable, the later solution will not be effected, leaving the boundary of the interior domain unchanged.

To see this in practice, we take an arbitrary PDE, written in flux-source form,

$$\frac{\partial \mathbf{q}}{\partial t} + \nabla \cdot \mathbb{F}(\mathbf{q}) = \mathbf{S}(\mathbf{q}), \tag{B.1}$$

where q is the interior variable, $\mathbb{F}$ is the flux, and $\mathbf{S}$ is the source. An exterior variable w is advanced with a similar system, except that it includes an extra source term $\mathbf{\Omega}(\mathbf{q})$,

$$\frac{\partial \mathbf{w}}{\partial t} + \nabla \cdot \mathbb{F}(\mathbf{w}) = S(\mathbf{w}) + \Omega(\mathbf{q}). \tag{B.2}$$

The variables w and q are related through a transition variable μ, which varies smoothly from 0 in the interior to 1 in the exterior region (see Figure B.2). The source term functions to transfer the interior solution to the auxiliary solution so that $w = q$ at the open boundary (the boundary between the transition and exterior regions). The value of w just outside this boundary is used as the boundary condition on q.

This set up alone will not prevent information from reflecting off of the exterior boundary and re-entering the interior domain through the boundary condition on q. To prevent this, the solution on w is periodically reintegrated with source $\Omega(q) = 0$ for some period of time. This effectively erases the leading edge of the wave front. When the reintegration and quiescent times are chosen appropriately, the wave front will always be erased before reaching the exterior boundary.

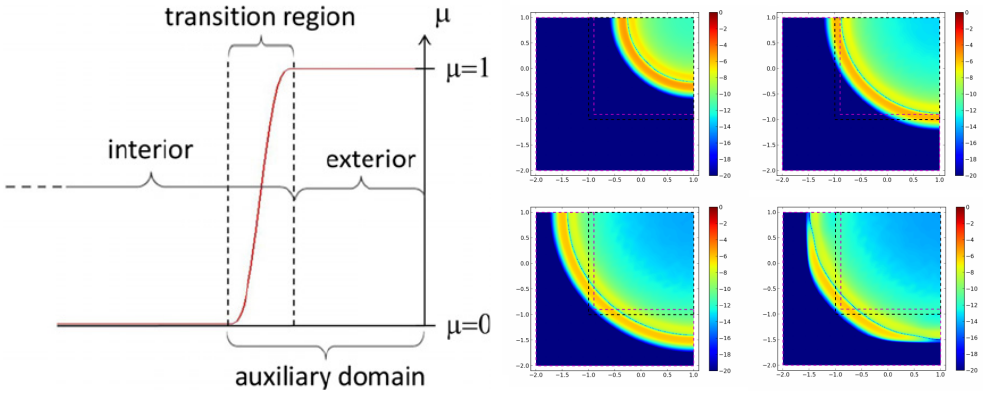

Figure B.1: LOBC domain schematic [100] (left), and a 2D EM wave pulse propagating into an LOBC exterior domain and subsequent reintegration [101](right).

B.3 WARPXM implementation details

WARPXM is well suited for efficient implementation of the LOBC. The code is modular: new boundary conditions, source terms, and equation sets can easily be added without touching much of the code. Variables and equation sets can be assigned to single or multiple subdomains, allowing auxiliary variables to only exist and be evolved in auxiliary domains.

Differing slightly from the method described in [100], the auxiliary solution was not reintegrated periodically. Instead, a second auxiliary variable w_{lacuna} was evolved simultaneously with the source term set to zero for some amount of time following a "reintegration." At what would have been a reintegration time, the solution contained in w_{lacuna} is swapped with that in w. After the swap, the w_{lacuna} is zeroed. The cycle is repeated over the duration of the simulation.

Evolving a second auxiliary variable prevents having to store source values and perform the periodic reintegration, which would require significant modifications to the WARPXM framework. This also spreads out the load of the reintegration over all time steps. Swapping

pointers for w and w_{lacuna}, instead of copying further reduces memory usage and time.

The structure of the problem setup is as follows:

- A mesh is created the has, at a minimum, an interior and exterior subdomain with a transition subdomain separating the two.

- Interior variables and equation sets are initialized as usual on the interior and transition subdomains.

- Auxiliary variables w and w_{lacuna} and their equation sets are initiated on the transition and exterior subdomains.

- On the transition subdomain alone, the transition variable is initialized and its gradient calculated.

- The gradient, along with the flux application for the interior variable q is passed to auxiliary variable source term Ω for w and w_{lacuna}. The source term for w_{lacuna} also includes a reintegration and lacuna time period to determine when to set the source to zero.

- A boundary condition on the transition-exterior boundary assigns values of w to the ghost values of q.

- As the simulation advances a reintegration time period, set by the user, triggers w and w_{lacuna} to be swapped, and then zeros w_{lacuna} .

To implement the LOBC in WARPXM, the following new capabilities were added:

- LOBC source term for $\Omega(q)$.

- A timed variable swap host action, which takes the place of the auxiliary variable reintegration.

- Generic virtual boundary condition that copies one variable to the ghost cell of another. This is used for the open boundary condition on q.

- Helper functions to simplify simulation setups that use LOBCs.

B.3.1 The LOBC source application

To find an appropriate expression for the source term $\Omega(q)$, we can replace all the ws in Eq. B.2 with the equivalent μq,

$$\frac{\partial \mu \mathbf{q}}{\partial t} + \nabla \cdot \mathbb{F}(\mu \mathbf{q}) = S(\mu \mathbf{q}) + \Omega(\mathbf{q}). \tag{B.3}$$

μ is not a function of time, and assuming that $\mathbb{F}$ and S are linear functions of q, then we can extract μ to get,

$$\mu \frac{\partial \mathbf{q}}{\partial t} + \nabla \cdot \mu \mathbb{F}(\mathbf{q}) = \mu S(\mathbf{q}) + \Omega(\mathbf{q}). \tag{B.4}$$

Performing a vector-scalar product rule, and collecting terms we get

$$\Omega(\mathbf{q}) = \mu \left(\frac{\partial \mathbf{q}}{\partial t} + \nabla \cdot \mathbb{F}(\mathbf{q}) - S(\mathbf{q}) \right) + \mathbb{F}(\mathbf{q}) \cdot \nabla \mu. \tag{B.5}$$

The expression in parentheses is the evolution equation for q, and is equal to zero. What remains is a simple equation for $\Omega(q)$ that depends only on the flux $F(q)$ and the gradient of the transition variable:

$$\Omega(\mathbf{q}) = \mathbb{F}(\mathbf{q}) \cdot \nabla \mu. \tag{B.6}$$

In the implementation for WARPXM, an application is created that takes as inputs the flux application for q, as well as the gradient of μ ($[\partial\mu/\partial x, \partial\mu/\partial y, \partial\mu/\partial z]$) calculated previously. The application is also made time dependent, so that it may be turned off during the quiescent period in the reintegration variable such that,

$$\Omega(\mathbf{q}, t) = \ell(t) F(\mathbf{q}) \cdot \nabla\mu, \tag{B.7}$$

where $\ell(t) = 0$ for $nt_{reint} < t < nt_{reint} + t_{lacuna},\ n = 1, 2, 3, ..,$ and one at all other times.

The flux $F(q)$ is the same analytic flux as calculated in the evolution equations for q. To make the source app general use (regardless of problem being solved), the app is passed a flux app in the input file.

```
<w_lobc_source>
  Type = application
  Kind = LOBC_SOURCE
  ReintegrationTime = 2.0
  LacunaTime = 0.0
  ExteriorVariable = [6, 7, 8, 9, 10, 11]
  GradientMu = [18, 19, 20]
  InteriorVariable = [0, 1, 2, 3, 4, 5]
  <q_flux_app>
    Type = application
    Kind = maxwell
    skin_depth_norm = 1.0
    omega_p_norm = 1.0
    Field = [0, 1, 2, 3, 4, 5]
  </q_flux_app>
</w_lobc_source>
```

When the `setup()` of the LOBC source (`wmapplication_lobc_source.cc`) is called during simulation initialization, the crypt set is searched for an application

```
std::vector<std::string> names = wxc.getNamesOfType("application");
```

If one is found the cryptset for the flux application block is extracted, and used to create the `WmApplication` object `_flux_app`.

```
if (names.size()==1)
{
  const WxCryptSet& subwxc = wxc.getSet(names[0]);
  _flux_app.reset(WxCreatorMap<WmApplication>::getNew(subwxc.get<std::string>("Kind")));
  _flux_app->setup(subwxc);
}
```

and finally the setup function for that application is called.

During the simulation the `internal_flux()` function of the `_flux_app` is called and used to calculate the source term at that node

```
// Calculate the internal flux
std::vector<std::vector<real>> internalFlux(pEG->num_dims,std::vector<real> (num_components,0.));
_flux_app->internal_flux(q, aux, pEG, internalFlux);

if (std::fmod(t, _reint_time) >= _lacuna_time)
{
  for (size_t i=0; i < num_components;++i)
  {
    for (size_t j = 0; j < pEG->num_dims; ++j)
    {
      source[i] += aux[j] * internalFlux[j][i];
    }
  }
}
```

B.3.2 Reintegration: the fill_value and timed_swap host actions

Performed with the `fill_value` and `timed\_swap` host actions.

B.3.3 Boundary condition at the open boundary

WARPXM treats normal boundary conditions by assigning values to the nodes on ghost elements (additional elements that WARPXM appends to the element list from the imported mesh). VBCs differ from normal boundary conditions in WARPXM in that there are no ghost elements created on these interior subdomain boundaries.

B.4 Using LOBCs in WARPXM

Applying these open boundary conditions are more involved than typical boundary conditions in WARPXM.

1. Predetermine the boundary condition reintegration and quiescent times based on physics of the problem B.4.1. Use these times and known wave speeds to determine necessary size of transition and exterior regions.

2. Create a mesh with two extra subdomains on the open boundary for a transition and exterior region (Section B.4.2) using sizes calculated in the previous step.

3. Set up the interior problem. This process does not changed.

4. For the open boundary condition extra variables need to be initialized for two sets of exterior variables, a transition parameter, and the gradient of the transition parameter.

5. Initial conditions applied to exterior physical variables, and an appropriate profile assigned to the transition variable.

6. Create apps for exterior variable physical fluxes and sources, as well as a transition region source for passing the interior to the exterior variables.

7. Apply boundary conditions on the interior and exterior physical variables.

8. Create Variable Adjusters for the transition variable gradient calculation, boundary conditions, and exterior variable swapping and zeroing.

9. Set up Spatial Solvers and a Time Integrator.

Steps 3-9 have been automated through a WARPy helper class. Its use is described in Section B.4.3 and further detail on implementation in Section B.5

B.4.1 Choosing reintegration and quiescent time periods

Reintegration and quiescent time periods should be chosen so that the fastest wave speed in the system will not travel the width of the exterior region (or twice that width if reflection is allowed) during a reintegration period.

If a is the fastest wave speed, L_e and L_t are the exterior and transition domain widths, some advisable bounds on times are

$$t_{integration} \leq L_e/a + t_{quiescent} \quad : \quad t_{quiescent} \approx L_t/a. \tag{B.8}$$

B.4.2 Mesh

To run a simulation with an LOBC a mesh file must be created with at least three subdomains (names of domains listed bellow are suggestions only):

- "interior" - The interior subdomain can either be all of the normal simulation domain (excepting the transition region) or just the region in the domain adjacent to the transition region.

- "transition" - The transition subdomain is part of the normal simulation domain and completely separates the interior from the exterior subdomains. The transition region should be at minimum 10 elements across.

- "exterior" - This is the only region that is outside the normal simulation domain. The only subdomain it shares a boundary with is the transition subdomain. The larger the exterior domain, the larger the added computational cost, but the less frequent reintegrations need to occur. As reintegrations add very little to computation time in this implementation, it is better to have a smaller exterior subdomain. 3 to 4 times the width of the transition region is sufficient.

And two node sets:

- "transBoundary" - Separates the interior and transition subdomains.
- "openBoundary" - Separates the transition and exterior subdomains. Also constitutes the normal simulation domain boundary.
- And any physical boundaries on the transition and exterior subdomains.

The WARPy input file is created in the normal way. Variables, initial conditions, apps, variable adjusters, and spatial solvers can be created for the **interior** subdomains as usual.

B.4.3 Creating the open boundary condition: the WARPy LOBC helper object

To facilitate initializing LOBCs in WARPy input files, a helper object was created to automate the setup of all variables, apps, sources, and boundary conditions on the transition and exterior domains.

Once the interior problem has been set up, a `warpy.helper.lobc` object is created for each interior variable (see below).

```
lobc_q = warpy.helpers.lobc(
    interior_variable = q,
    sorder = sorder,
    lacuna_time = lacuna_time,
```

```
    reintegration_time = reintegration_time,
    interior_subdomains = interior_subdomains,
    tran_subdomains = tran_subdomains,
    exterior_subdomains = exterior_subdomains,
    interior_to_transition_boundary = interior_to_transition_boundary,
    open_boundary = open_boundary,
    exterior_boundary = exterior_boundary,
    other_tran_subdomain_boundaries = None
)
```

The `lobc` object contains a list of attributes describing the lacuna time, reintegration time, spatial order, and the names of subdomains and boundaries specific to that LOBC, as well as a number of functions for creating the host actions associated with the LOBC: auxiliary variable initial conditions, transition variable gradient calculation, LOBC auxiliary variable temporal solver, and the reintegrated solution swapping and zeroing.

After the object is created, the following object function calls will execute the setup:

1. Create an initial condition applicator or LOBC specific variables:

```
ic_applicators_lobc = q_lobc_right.vars_setup(
    direction = [1, 0, 0],
    center = transition_center,
    transitionwidth = transition_width
)
```

2. Create host action for calculating the transition variable gradient before the first time step:

```
host_action_lobc_mu = q_lobc_right.calc_dmu()
```

3. Create the temporal solver for the transition and exterior domains. This first requires the user to setup physics fluxes, sources, and boundary conditions for auxiliary vari-

ables, as these will depend on your particular problem. Several functions have been created to facilitate the process:

```
# Setup physics fluxes and sources
app_flux_w, app_flux_wlacuna = q_lobc_right.apps_flux_maxwell(
    skin_depth_norm = skin_depth_norm,
    omega_p_norm = omega_p_norm
)

# Setup physics boundary condition apps. TODO: make easier.
# if not set, warpxm will assume copyout
```

Once setup, the physics apps can be passed to the temporal solver creator:

```
temporal_solver_lobc = q_lobc_right.create_temporal_solver(
    torder = torder,
    apps_flux_interior_var = [app_flux_q],
    apps_source_interior_var = None,
    apps_flux_aux_vars = [app_flux_w, app_flux_wlacuna],
    apps_source_aux_vars = None,
    apps_bc_physics = None
)
```

4. A separate host action is created that performs the reintegration variable swapping and zeroing, which must happen before each time step (and therefore requires its own host action):

```
host_actions_lobc_pre_ti = q_lobc_right.create_pre_ti_hostactions()
```

5. Finally, the auxiliary variables can be accessed to include them in any variable write out host action:

```
writer = warpy.host_actions.writer(
```

```
    name = 'writer',
    ReadVars = [q, lobc_q.w, lobc_q.wlacuna, lobc_q.mu, lobc_q.dmu]
)
```

The host actions created can then be passed to the `warpy.dg_sim` object as follows:

```
sim = warpy.dg_sim(
    name                      = 'lobc_maxwell_2D',
    meshes                    = [mesh],
    initial_conditions        = ic_applicators + ic_applicators_lobc,
    extra_start_host_actions = [host_action_lobc_mu],
    temporal_solvers          = [temporal_solver, temporal_solver_lobc],
    pre_ti_host_actions       = host_actions_lobc_pre_ti,
    writers                   = [writer],
    time                      = [0, dt_final],
    dt_controller             = dt_controller,
    flexible_writeout         = False,
    write_steps               = write_steps,
    verbosity                 = 'info'
)
```

B.5 The LOBC WARPy helper object

The following are the steps preformed internally by the `lobc` helper object.

Variables to be initialized:

- **Interior variables:** These are the simulation variables, and are initialized everywhere in the normal simulation domain
  - Subdomains: “interior”, “transition”
  - Virtual subdomains: “exterior”
  - Initial condition: what ever is necessary for the problem

- **Exterior variables w and w_{lacuna}:** This are the auxiliary variables that the interior solution is passed to through the source term in the transition region.

  - Subdomains: "transition", "exterior"
  - Virtual subdomains: None
  - Initial condition: must be consistent with the interior variable such that $w = \mu q$, where q is the interior variable.

- **Transition variables μ and $\nabla\mu$:** The transition variables only exist in the transition region

  - Subdomains: "transition"
  - Virtual subdomains: None
  - Explodable: False (This prevents WARPXM from creating copies of the variable for Runge-Kutta intermediate values.)
  - Initial condition: μ must be a C^1 continuous function with the boundary conditions $\mu|_{int} = 0$, $\mu|_{ext} = 1$, and $\nabla\mu \cdot \hat{n}|_{int,ext} = 0$, where $\hat{n}$ is the normal at the interior or exterior boundary.
  - Caution!: When $\nabla\mu$ is calculated from a specified μ with a gradient variable adjuster, boundary values of μ must be specified. Setting zero Neumann (zero first derivative) boundary conditions on all physical boundaries is sufficient.

    As only $\nabla\mu$ is required, and if it is known can be specified without having to initialize μ and calculate its gradient.

B.5.1 Assigning flux and source applications

Physics apps for fluxes and sources are assigned to the interior and exterior variables alike.

In addition to the physics apps, an LOBC source ($\Omega(q)$) is applied only to the exterior variables, and only in the transition subdomain.

B.5.2 Setting virtual and traditional boundary conditions

- Non-LOBC boundaries are set as usual.

- Physical boundary conditions on the exterior subdomain should not cause backward propagation of information through the open boundary in the time between reintegration. Zero Neumann or a continuation of the physical boundary conditions from the interior domain are good options.

- Boundary condition on μ should be zero Neumann (zero gradient) on all transition subdomain boundaries.

- Boundary condition on "transitionBoundary" for auxiliary variables should be a zero Dirichlet.

- Boundary condition on "openBoundary" for interior variables will use the virtual boundary condition.

B.6 Example: 2D Maxwell equations

The example in Figure B.2 was run using the `2D_maxwell_lobc.py` input file. The boundary conditions in y are conducting wall. A wave train emanates from the right boundary and passes through transition region to the auxiliary variable. In the last frame, the auxiliary solution has been reintegrated and wave front has receded from the left wall. The domain is 0.5×7 nu, the normalized speed of light is 1, and the quiescent and reintegration times are 4 and 6, respectively

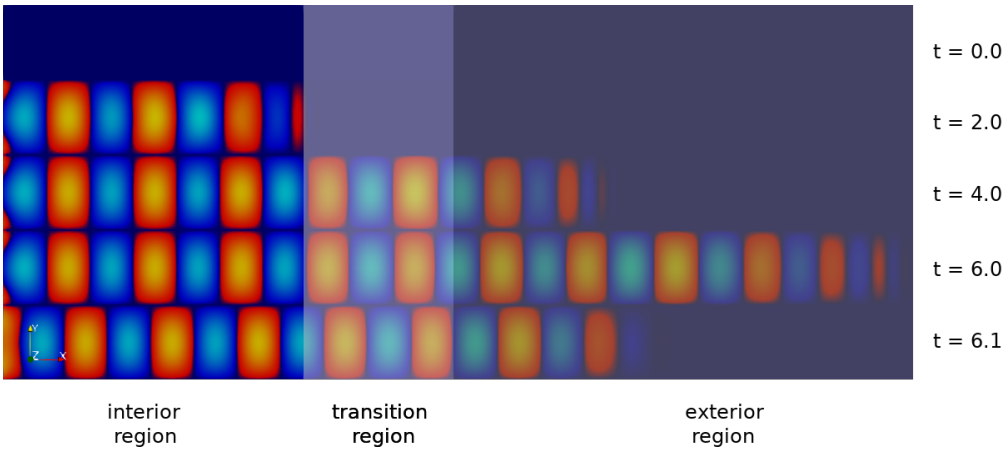

Figure B.2: A 2D EM wave propagating into an LOBC exterior domain and subsequent reintegration.

Appendix C

COLLISIONAL OPERATORS FOR VARIOUS PLASMA MODELS

In this appendix collision operators for elastic and inelastic collisions are reviewed. Starting with the Boltzmann-type collision operators, and then summarizations of corresponding simplified models used in the Bolsig+ and the Meier reacting 5-moment model.

C.1 Boltzmann-type collision operators

The classic Boltzmann collision operator for elastic 2-body collisions

$$\left.\frac{df}{dt}\right|_{coll} = \int\int [f'(v_\alpha)f'(v_\beta) - f(v_\alpha)f(v_\beta)]g\sigma_{\alpha\beta}(g,\chi)d\Omega d^2\boldsymbol{v}_\beta \tag{C.1}$$

where primes denote distribution functions after the collisions, $g = |\boldsymbol{v}_\alpha - \boldsymbol{V}_\beta|$ is the relative speed between species, $\sigma_{\alpha\beta}(g,\chi)$ is the differential cross section at relative speed g and scattering angle χ, and Ω is the differential solid angle. Zhdanov [102] expands this to arbitrary excited, molecular, and atomic species

$$\frac{df_{\alpha i}}{dt} + \boldsymbol{v}\cdot\nabla f_{\alpha i} + \frac{q_\alpha}{m_\alpha}(\boldsymbol{E} + \boldsymbol{v}\times\boldsymbol{B})\cdot\nabla_v f_{\alpha_i} = \left.\frac{df}{dt}\right|_{coll} + \left.\frac{df}{dt}\right|_{react} \tag{C.2}$$

where

$$f_{\alpha i} = f_\alpha(\boldsymbol{r},\boldsymbol{v},t,i) \tag{C.3}$$

and i denotes the excited state. The collision integrals, as described by Wang-Chang and Uhlenbeck[], for binary elastic and inelastic collisions (momentum transfer, excitation, and de-excitation)

$$\left.\frac{df}{dt}\right|_{coll} = \sum_\beta\sum_{jkl} J_{ij}^{kl}(f_{\alpha i}f_{\beta j}) \tag{C.4}$$

where i and j are the excited states for species α and β before the collision, and k and l are the excited states after. The collision integral is defined as

$$J_{ij}^{kl}(f_{\alpha i}f_{\beta j}) = \int\int \left(\frac{S_{\alpha i}S_{\beta j}}{S_{\alpha k}S_{1\beta l}}f'_{\alpha k}f'_{\beta k} - f_{\alpha i}f_{\beta j}\right) g\sigma_{\alpha\beta}(ij|kl,g,\chi)d\Omega d\boldsymbol{v}_{1\beta}. \tag{C.5}$$

Binary reactions of the form [103]

$$A_\alpha + A_\beta \leftrightarrow A_\gamma + A_\delta \tag{C.6}$$

have the following collision integral

$$\left.\frac{df}{dt}\right|_{react} = \frac{1}{2}\sum_{\beta\gamma\delta}\sum_{jkl}\int\int \left(f'_{\gamma k}f'_{deltal}\frac{S_{\alpha i}S_{\beta j}}{S_{\gamma k}S_{deltal}}\left(\frac{m_\alpha m_\beta}{m_\gamma m_\delta}\right)^3 - f_{\alpha i}f_{\beta j}\right) g\sigma^r_{\alpha\beta\gamma\delta}(ij|kl,g,\chi)d\Omega d\boldsymbol{v}_{1\beta}. \tag{C.7}$$

Coulomb collisions theoretically have an infinite interaction potential that falls of like $1/r$, which would require each charge particle interact with every other. Due to Debye shielding, the interactions of particles through electromagnetic fields is separated into long range, or collective fields, and short range interactions within the Debye sphere.

C.2 Bolsig+ collision operators

The collision operators in Bolsig+ are separated into two-types: isotropic and anisotropic. Isotropic collision operators are indicated by a subscript 0. Anisotropic collision operators are indicated by a subscript 1, and often neglected for simplicity, as their total contribution is often small. See references [17] and [17] for more details.

Elastic collisions

$$\tilde{C}_{0,k=\text{elastic}} = \gamma x_k \frac{2m}{M_k}\frac{\partial}{\partial\varepsilon}\left[\varepsilon^2\sigma_k\left(F_0 + \frac{k_B T_k}{e}\frac{\partial F_0}{\partial\varepsilon}\right)\right] \tag{C.8}$$

where x_k, M_k and T_k are the mole fraction, mass, and temperature of target species k, respectively. This assumes Maxwellian velocity distributions for all target particles.

Ionization for equal sharing of energy between incoming and emitted electrons

$$\tilde{C}_{0,k=\text{ionization}} = -\gamma x_k[\varepsilon\sigma_k(\varepsilon)F_0(\varepsilon) - 2(2\varepsilon + u_k)\sigma_k(2\varepsilon + u_k)F_0(2\varepsilon + u_k)]. \tag{C.9}$$

Here u_k is the threshold energy for the reaction. For primary electron taking all energy

$$\tilde{C}_{0,k=\text{ionization}} = -\gamma x_k[\varepsilon\sigma_k(\varepsilon)F_0(\varepsilon) - (\varepsilon+u_k)\sigma_k(\varepsilon+u_k)F_0(\varepsilon+u_k)] + \delta(\varepsilon)\gamma x_k \int_0^\infty u\sigma_k(u)F_0(u)du. \tag{C.10}$$

The last term deposits secondary electrons at zero energy.

Recombination/Attachment

$$\tilde{C}_{0,k=\text{attachment}} = -\gamma x_k \varepsilon\sigma_k(\varepsilon)F_0(\varepsilon) \tag{C.11}$$

Electron-electron collisions and **electron-ion collisions** are more complex and are not repeated here for brevity. Details can be found in [91].

C.3 Collision operators for Meier reacting 5-moment model

In the Meier reacting 5-moment fluid model[15], reacting collision operators for ionization, recombination and charge exchange are defined as

$$C_n^{ion} = -f_n \int f_e v_{rel}\sigma_{ion}(v_{rel})d\boldsymbol{v}, \tag{C.12}$$

$$C_e^{ion} = -C_i^{ion} = f_n \int f_e v_{rel}\sigma_{ion}(v_{rel})d\boldsymbol{v}, \tag{C.13}$$

$$C_e^{rec} = -f_i \int f_e g\sigma_{rec}(v_{rel})d\boldsymbol{v}, \tag{C.14}$$

$$C_i^{rec} = -f_i \int f_e g\sigma_{rec}(v_{rel})d\boldsymbol{v}, \tag{C.15}$$

$$C_n^{rec} = \frac{m_e}{m_n} f_e \int f_i \sigma_{rec} v_{rel} d\boldsymbol{v} + \frac{m_i}{m_n} f_i \int f_e \sigma_{rec} v_{rel} d\boldsymbol{v}, \tag{C.16}$$

$$C_i^{cx} = f_n \int f_i \sigma_{cx} v_{rel} d\boldsymbol{v} - f_i \int f_n \sigma_{cx} v_{rel} d\boldsymbol{v}, \tag{C.17}$$

$$C_n^{cx} = \frac{m_i}{m_n} f_i \int f_n \sigma_{cx} v_{rel} d\boldsymbol{v} + \frac{m_i}{m_n} f_n \int f_i \sigma_{cx} v_{rel} d\boldsymbol{v}, \tag{C.18}$$

C.3.1 Moments of the ionization integral

The Meier model makes the assumption that the electron thermal speed is large compared to the drift speed $v_{Te} \gg v_{rel}$, and $T_e \geq T_i$, therefore $v_{rel} \approx w$, so the inner integral becomes

$$\int f_e v_{rel} \sigma_{rec}(v_{rel}) d\boldsymbol{v} \approx \int f_e(\boldsymbol{w}) \sigma_{rec}(w) d\boldsymbol{w} = n_e \left\langle \sigma_{ion} u_e \right\rangle \tag{C.19}$$

0th Moment

$$\int C_n^{ion} d\boldsymbol{v} \approx \Gamma_n^{ion} \equiv -n_e n_i \left\langle \sigma_{ion} u_e \right\rangle = -\Gamma_i^{ion} = -\Gamma_e^{ion}. \tag{C.20}$$

Here Γ_α^{react} is the reaction source rate for species α.

1st Moment

$$\int m_i \boldsymbol{v} C_i^{ion} d\boldsymbol{v} \approx m_i \boldsymbol{v_n} \Gamma_i^{ion} \tag{C.21}$$

2nd Moment

Ions:

$$\int \frac{1}{2} m_i v^2 C_i^{ion} d\boldsymbol{v} \approx \frac{m_i}{m_n} \left(\Gamma_i^{ion} \frac{1}{2} m_n v_n^2 + Q_n^{ion} \right) \tag{C.22}$$

Electrons:

$$\int \frac{1}{2} m_e v^2 C_e^{ion} d\boldsymbol{v} \approx \frac{m_e}{m_n} \left(\Gamma_i^{ion} \frac{1}{2} m_n v_n^2 + Q_n^{ion} \right) - \Gamma_i^{ion} \psi_{ion} \tag{C.23}$$

Neutrals:

$$\int \frac{1}{2} m_n v^2 C_n^{ion} d\boldsymbol{v} \approx -\left(\Gamma_i^{ion} \frac{1}{2} m_n v_n^2 + Q_n^{ion} \right) \tag{C.24}$$

where $Q_n^{ion} \equiv \Gamma_i^{ion} \frac{3}{2} k T_n$ is the transfer of internal energy. See Meier paper for derivation of recombination and charge-exchange.